Microvascular Damage as Initial Event of Scar Formation after Carbon Ion Irradiation of Cardiac Substructures

Vom Fachbereich Biologie der Technischen Universität Darmstadt
Zur Erlangung des akademischen Grades eines Doctor rerum naturalium
genehmigte Dissertation von Master of Science Nadine Erbeldinger aus Lindenfels

1. Referent: Prof. Dr. Gerhard Thiel
2. Referent: Prof. Dr. Marco Durante

Tag der Einreichung: 18.04.2017
Tag der mündlichen Prüfung: 06.06.2017

Darmstadt 2017
D 17

TECHNISCHE
UNIVERSITÄT
DARMSTADT

Microvascular Damage as Initial Event of Scar Formation After Carbon Ion Irradiation of Cardiac Substructures

Vom Fachbereich Biologie der Technischen Universität Darmstadt
zur Erlangung des akademischen Grades eines Doctor rerum naturalium
genehmigte Dissertation von Master of Science Nadine Erbeldinger aus Lindenfels

1. Referent: Prof. Dr. Gerhard Thiel
2. Referent: Prof. Dr. Marco Durante

Tag der Einreichung: 18.04.2017
Tag der mündlichen Prüfung: 06.06.2017

Darmstadt 2017
D 17

Ehrenwörtliche Erklärung

Ich erkläre hiermit ehrenwörtlich, dass ich die vorliegende Arbeit entsprechend den Regeln guter wissenschaftlicher Praxis selbstständig und ohne unzulässige Hilfe Dritter angefertigt habe. Sämtliche aus fremden Quellen direkt oder indirekt übernommenen Gedanken sowie sämtliche von Anderen direkt oder indirekt übernommenen Daten, Techniken und Materialien sind als solche kenntlich gemacht.

Die Arbeit wurde bisher bei keiner anderen Hochschule zu Prüfungszwecken eingereicht.

Darmstadt, den 18.04.2017

Danksagung

Mein allerster Dank gilt Prof. Dr. Marco Durante für die Aufnahme in die Abteilung Biophysik, die es mir ermöglichte, meine Masterthesis und diese Arbeit durchführen zu können. Gleichermaßen möchte ich Prof. Dr. Gerhard Thiel dafür danken, dass er mein Erstgutachten übernahm. Beiden möchte ich für ihre Unterstützung, Interesse und hilfreichen Ratschläge während unserer Gespräche danken.

Ein besonderer Dank gilt auch Prof. Dr. Claudia Fournier, die mich mit offenen Armen in ihre Gruppe aufgenommen und seit meiner Masterthesis betreut hat. Danke dafür, dass du mir die Mitarbeit im „Schweineprojekt“ ermöglich hast. Und danke auch für die Zeit, die du für meine Betreuung aufgewendet hast.

Nicht weniger danke ich Dr. Felicitas Merz für ihre direkte Betreuung und Zusammenarbeit im Labor. Danke für deine Unterstützung bei der Etablierung histologischer Färbungen und deren Auswertung. Und danke auch dafür, dass ich mich in nahezu allen Lebenslagen auf dich verlassen konnte.

In diesem Zuge möchte ich auch allen einen Dank aussprechen, die am „Schweineprojekt“ mitgearbeitet haben. Besonders hervorzuheben ist hierbei Dr. Immo Lehmann, der dieses Projekt ins Leben rief und nie müde wurde, sein Wissen zu teilen. Auch möchte ich Dr. Patrick Lugenbiel für seine tatkräftige Unterstützung bei der Durchführung diverser „follow ups“ und Entnahme von Proben danken. Weiterhin gilt ein herzlicher Dank den Mitgliedern des Motion Teams, besonders dem Gruppenleiter Dr. Christian Graeff, dessen Hilfsbereitschaft beispielslos war. Außerdem möchte ich Dr. Anna Constantinescu, Dr. Daniel Richter, Dr. Anna Eichhorn, und Dr. Matthias Prall für die Zusammenarbeit und die angenehme Arbeitsatmosphäre auch während stressiger Phasen danken. Danke auch dafür, dass ihr mich in dieses Projekt aufgenommen habt und mir immer wieder gerne bei Fragen zu den Hintergründen des Projekts und der dazugehörigen Physik zur Seite standet. I also want to thank Dr. Palma Simoniello for working with me in this project. Thank you for the time and your support.

Ein besonders herzliches Dankeschön geht auch alle Bachelor-, Master- und Werkstudenten, die mir bei der Anfertigung dieser Arbeit geholfen haben. Vielen Dank für eure tatkräftige Unterstützung. Besonders hervorzuheben sind Marie Liebig, Jasmin Hunsrucker, Florian Braun, Cosima Caliendo und Eva Thönnes, welche mich auch während ihrer Tätigkeit als TA in unserer Gruppe entlastete.

Außerdem möchte ich auch bei allen Mitgliedern der *Entzündungsgruppe* für unsere gemeinsame Zeit und eine sehr angenehme Arbeitsatmosphäre bedanken. Es war mir eine Freude mit euch zusammenzuarbeiten.

Weiterhin war es mir eine Ehre, ein Mitglied der Abteilung Biophysik zu sein. Danke dafür, dass ich immer offene Türen vorgefunden habe und besonders der Austausch zwischen Biologen und Physikern derart rege war. Hierbei möchte ich vor allem Dr. Thomas Friedrich danken, der mit anscheinend unendlicher Geduld immer wieder gerne alle Statistik-bezogenen Fragen diverser Biologen, darunter auch meine, klärte.

Wem ich auch auf jeden Fall danken möchte ist die Mittagsessensgruppe, die immer dafür sorgte, dass die Mittagszeit ein Highlight des Tages war. Danke dafür, dass ich mich immer darauf freuen konnte, mittags zu lachen, etwas zu lernen oder Probleme zu besprechen. Hierbei möchte ich vor allen Paul Günther, Christoph Sauter, Tamara Buch, Alexander Bothe, Jona Renner und Sylvie Lerchl für die kurzweiligen und abwechslungsreichen Mittagspausen danken.

Auch möchte ich auch allen Mitgliedern des Graduiertenkollegs (GrK) 1657 danken. Danke dafür, dass alle Veranstaltungen des GrK nicht nur unserer Fortbildung dienten, sondern auch Spaß gemacht haben. Dazu haben vor allem Tanya Syzonenko, Laura Babel, Johannes Pilakowski, Kateryna Shreder, aber auch viele mehr beigetragen.

Neben allen, die mich während meiner gesamten Zeit bei GSI unterstützt haben, möchte ich aber auch jenen danken, die in den letzten Monaten meine Arbeit Korrektur gelesen haben. Scarlett Nitsch, Dr. Till Dettmering, Janna Zimmermann und Jan Kahlenberg, ich danke euch für eure wertvollen Hinweise, ohne euch wäre diese Arbeit bestimmt weniger gelungen.

Danken möchte ich auch meiner Familie für ihre immerwährende Unterstützung. Danke auch für eure aufmunternden Worte und wertvollen Ratschläge. In erster Linie möchte ich meiner Mutter dafür danken, dass sie mich immer dazu ermutigt hat, meine Ziele zu verfolgen, und dafür, dass sie immer an mich geglaubt hat.

Mein mit Abstand größter Dank gilt Tobi, der mich auch in stressigen Zeiten immer ertragen und unterstützt hat. Danke dafür, dass du einfach immer für mich da bist. Danke für deine Geduld, deine Liebe und deine Partnerschaft.

Zusammenfassung

Aus der Strahlentherapie ist bekannt, dass die Bestrahlung von Herzgewebe, welche im Zuge der Krebsbehandlung im Thorax stattfindet, zu elektrophysiologischen Veränderungen führen kann. Diese Erkenntnisse wurden für eine erste *in vivo*-Machbarkeitsstudie genutzt, um mit Kohlenstoffionen-Bestrahlung eine alternative, nicht-invasive Behandlungsmethode von Herzrhythmusstörungen zu etablieren. Es ist davon auszugehen, dass durch die Bestrahlung u.a. Schäden der kleinen Blutgefäße (Mikrovaskulatur) im Herzgewebe erzeugt werden. Diese stellen vermutlich Ausgangsereignisse für Langzeiteffekte wie Fibrose und schließlich Störungen der Elektrophysiologie dar. Dennoch sind die zugrundeliegenden Wirkungsweisen dieser Effekte nach hoch dosierter Bestrahlung eines geringen Volumens mit Kohlenstoffionen bisher noch nicht vollständig bekannt. Daher wurden in dieser Arbeit strahleninduzierte mikrovaskuläre Schäden nach Ablation potentiell arrhythmogener Substrukturen in Schweineherzen charakterisiert.

Im Zuge dieses Projekts wurde die Bestrahlung des linken Ventrikels (LV) und Atrioventrikularknotens (AVN) mit hohen Dosen durchgeführt. Während der LV mit 40 Gy bestrahlt wurde, wurde eine Dosiseskalationsstudie mit 25; 40 oder 55 Gy bei Bestrahlung des AVN durchgeführt. Die Bestrahlung der Eingangskanäle führte zu einer dortigen Deposition mittlerer Dosen (7 – 17 Gy). In allen Gruppen wurden elektrophysiologische Veränderungen im Zielgewebe detektiert. Diese Veränderungen waren vermutlich durch eine fibrotische Narbenbildung bedingt. Dennoch war die Entwicklung des Narbengewebes auch für gleiche Dosisgruppen heterogen ausgeprägt.

Dementsprechend wurden mikrovaskuläre Schäden (Hämorrhagie und Verlust der Mikrovaskulatur) und Folgeprozesse (Entzündungsprozesse und Zelltod) in der vorgelegten Arbeit untersucht. Das wiederholte Auftreten dieser Prozesse bedeutete, dass die Narbenbildung noch nicht abgeschlossen war. Neben den Analysen im Zielgewebe wurden auch andere Bereiche des Herzens untersucht, um mögliche Nebeneffekte festzustellen. In den Eingangskanälen wurden Hinweise auf ein verzögertes Fortschreiten von Gewebsveränderungen gefunden. Indes wurde in unbestrahlten Herzbereichen keine Schadensausbreitung während der untersuchten sechs Monate festgestellt. Zusätzlich wurden keine systemischen Entzündungsprozesse nach der applizierten Bestrahlung mit Kohlenstoffionen detektiert.

Abstract

The irradiation of the heart during thoracic cancer radiotherapy can lead to changes in the cardiac electrophysiology. These findings were applied in a first *in vivo* feasibility study using scanned carbon ion irradiation to establish an alternative, non-invasive treatment method for cardiac arrhythmias. Damage to the small blood vessels (microvasculature) after cardiac irradiation is putatively an initial event for longterm effects like fibrosis and finally electrophysiological changes. However, the exact underlying mechanisms of those effects after high dosed carbon ion irradiation of small volumes are not fully understood. Therefore, irradiation–induced vascular damage was characterized in a porcine model for the ablation of potentially arrhythmogenic cardiac substructures in the presented thesis.

The irradiation of target areas, the left ventricle (LV) and atrio–ventricular node (AVN), was performed with high doses. The LV target was exposed to 40 Gy. For the AVN target, a dose–escalation study was performed. Consequently, the AVN was irradiated with 25, 40 or 55 Gy. The irradiation of entrance channel regions resulted in the deposition of medium doses (7 – 17 Gy). All target groups exhibited electrophysiological changes in target areas. These changes were presumably caused by the formation of a fibrous scar. However, heterogeneous results for the scar formation were obtained among animals of the same dose group.

Correspondingly, the vascular damage (haemorrhage and loss of microvessels) and subsequent tissue responses (inflammatory processes and cell death) were investigated in this thesis. Their repeated occurrence pointed to an uncompleted scar formation. Aside from target areas, non-targeted regions were also investigated to detect potential side effects. In entrance channel regions, hints for a delayed progression of tissue remodelling were found. However, the damage in irradiated tissue was not spreading to unirradiated cardiac regions during the investigated time frame (until six months after irradiation). Furthermore, no systemic inflammation was detected after the applied carbon ion irradiation.

Contents

List of Figures

List of Tables

List of Abbreviations

AVN	atrioventricular node
BZ	borderzone
CA	cardiac arrhythmia
CRP	C-reactive protein
Cx	connexin
EC	endothelial cells
ECM	extracellular matrix
h	hours
HF	heart failure
HMGB1	high-mobility group box-1
IL	Interleukin
IFN	Interferon
IR	ionizing radiation
irr.[#]	dose was not determined
LAA	left atrial appendage
LET	linear energy transfer
LD-RT	low dose radiotherapy
LV	left ventricle
MI	myocardial infarct
N.D.	not dermined
pH	*potentia hydrogenii*
rpm	rounds per minute
RAA	right atrial appendage
RBE	relative biological effectiveness

RIHD	radiation-induced heart disease
RT	room temperature
RV	right ventricle
SMC	smooth muscle cells
TGF-β	transforming growth factor β
TNF-α	tumour necrosis factor-α
TU Darmstadt	Technische Universität Darmstadt
vWF	von Willebrand-factor

1. Introduction

Cardiac arrhythmias (CA) were identified as a large global burden, particularly in older individuals (Chugh et al., 2014; Verdino, 2015). As the average age of the population is increasing, the treatment of cardiac arrhythmias will move even more into focus over time. Therefore, this thesis was performed within the frame of a project aiming for the inactivation of cardiac tissue (ablation): The irradiation of small volumes with high dosed carbon ions was performed in pigs for the first time. It is assumed that this treatment induces an electrically isolating lesion. The consequent interruption of cardiac impulse propagation was presumably caused by a fibrous scar (Lehmann, Graeff, Durante, & Packer, 2016). Results from animal studies suggest vascular damage as initial event for cardiac fibrosis (Fajardo & Stewart, 1971; Seemann et al., 2012; Virag & Murry, 2003). Consequently, vascular damage and its implications after cardiac irradiation were investigated in the presented thesis. The link between vascular damage and fibrotic processes is a major topic in radiotherapy. Hence, the findings of this thesis contribute to the knowledge of tissue remodelling after irradiation.

1.1. Physics of Ionizing Irradiation

In the following sections, the basic physics of radiotherapy are presented. Based on their interaction with matter, the applied radiation qualities are characterized as ionizing radiation (IR). The term IR designates any radiation type causing ionization of atoms. However, a sufficiently high kinetic energy is needed to release electrons from the shell during interaction of target atom and radiation. If the target atom is part of a molecule, like DNA, IR can cause broken bonds, which eventually leads to the disintegration of molecules. The absorbed energy ΔE_{abs} per mass unit Δm is called dose D in measured in the SI unit Gy (Equation 1).

$$Gy = \frac{J}{kg} \left(\mathrm{D} = \frac{\Delta E_{\mathrm{abs}}}{\Delta \mathrm{m}}\right)$$

Equation 1: Definition of dose and SI unit Gy.

IR can be subdivided into photons, massless quanta of electromagnetic radiation, and accelerated particles, ions and neutrons. Based on their properties, photons act as sparsely ionizing and accelerated particles mostly comprise densely IR. The physics of both types of IR will be explained in more detail in the following sections. In radiobiology, the most relevant reference material is water, which represents the main component of cells (Atkins, 2010; Hall & Giaccia, 2006).

1.1.1. Photons

In classic physics, electromagnetic radiation is interpreted as electromagnetic field, consisting of two components: the electrical field, which interacts with charged particles, and the magnetic field, which only acts on moving charge. In radiotherapy, the most relevant photons comprise x- and γ-rays, because both radiation types have highly energetic single photons. In contrast to particle irradiation, photons have a small cross section. The interaction with matter mostly causes scattering or absorption. As photons exhibit a low probability to interact, they are defined as sparsely ionizing (Atkins, 2010).

1.1.2. Particles

In contrast to photons, accelerated particles are mainly considered as densely IR. Particle irradiation comprises neutrons and charged particles. Charged particles can be further differentiated into protons, α-particles (He^{2+}) or heavy ions (Hall & Giaccia, 2006). As neutrons are not relevant within the scope of this thesis, the physics of neutrons interacting with matter will not be described herein.

The interaction of charged particles with matter is based on the process of electronic stopping through inelastic Coulomb interactions: traversing particles predominantly interact with electrons of the target material through ionization and excitation. The specific track structures of an incident charged particle depends on the mass, charge and initial velocity. The interaction with matter and subsequent energy loss causes the formation of δ-electrons due to ionization of target atoms along the trajectory of an incident charged particle (Figure 1). Released δ-electrons have only low energy and consequently only a low mean free path length (in the order of nm for the core and cm for the penumbra of the track structure). As a result, a track of very dense ionizations around the trajectory of the particle emerges (Demtröder, 1997; Hall & Giaccia, 2006).

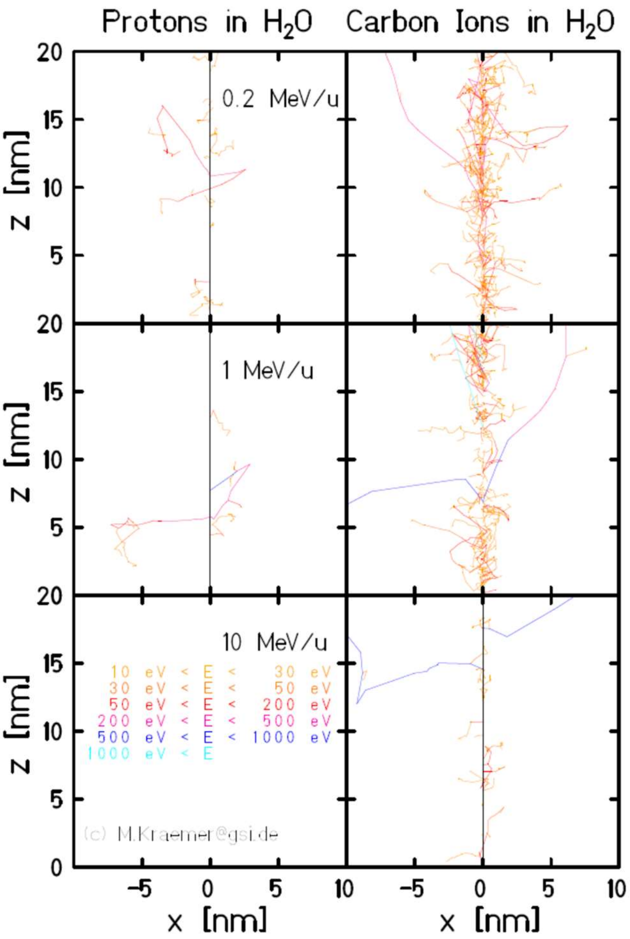

Figure 1: Simulation of δ-electrons produced by different energies of protons and carbon ions. Image courtesy of M. Krämer.

The energy, which is deposited by ionizations caused by the ion and δ-electrons, along the trajectory of the ion is defined as linear energy transfer (LET): the deposited energy E along path length s is proportional to the effective charge Z_{eff}^2 and its relativistic velocity $\beta = v/c$ (Equation 2). In the Bethe Bloch formula, the LET is described quantitatively (Demtröder, 1997; Hall & Giaccia, 2006).

$$\mathrm{LET} = \frac{\Delta \mathrm{E}}{\Delta s}\left[\frac{keV}{\mu m}\right] \propto \frac{Z_{eff}^2}{\beta^2}$$

Equation 2: Definition of the LET.

As mentioned above, the energy deposition of charged particles differs from photons. The depth dose deposition of different radiation qualities is shown in Figure 2. For photons, a built up effect at the beginning and an exponential energy loss can be observed. Due to the scattering of δ-electrons the initial part of the maximum dose deposition cannot be measured by a detector.

For charged particle irradiation, an incident accelerated charged particle only slowly decelerates as it traverses matter causing little energy loss at first. This steady plateau of deposited dose is termed as the entrance channel. In the next step, the amount of deposited energy per path length increases due to the slower velocity causing further deceleration. The following Bragg peak indicates the location of most energy loss, which is the dominant feature of depth dose deposition of charged particles. In case of heavy ions, nuclear fragmentation and inelastic scattering leads to a minor dose deposition behind the Bragg peak. These different physical properties are used for radiotherapy, mainly for the sparing of critical structures as discussed in more detail later.

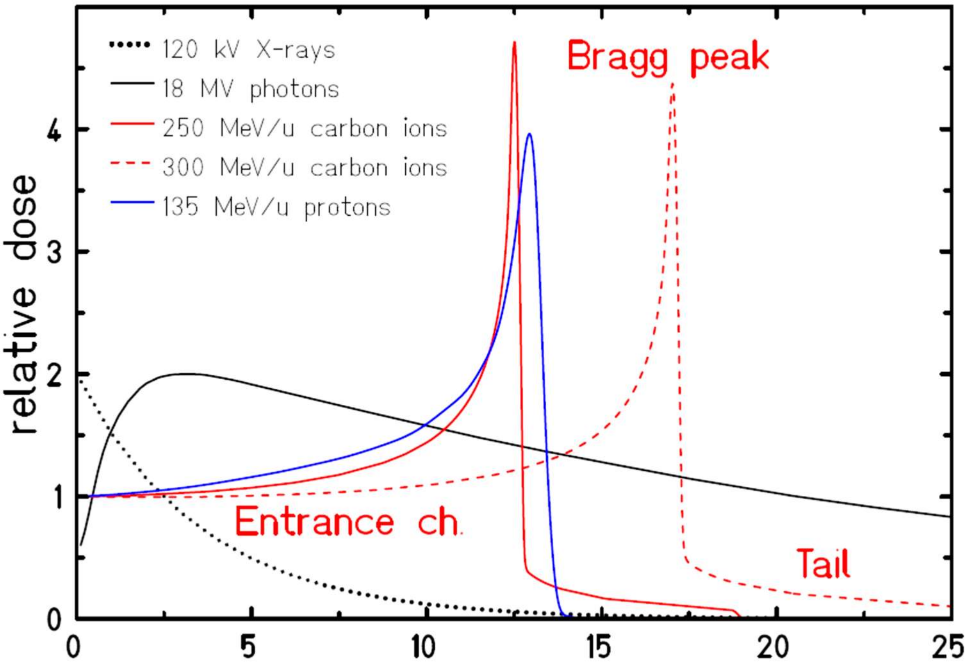

Figure 2: Depth dose distribution of different radiation qualities in water. The depicted radiation types are photons (black), carbon ions at different energies (red) and protons (blue). Characteristics of particle irradiation are indicated: first the entrance channel, which is followed by the Bragg peak and at last a dose tail. Reprinted from (Dettmering, 2013).

For understanding the action of different radiation qualities, not only their depth dose profile needs to be considered, but also their microscopic dose deposition differs. As visualized in Figure 3, X-rays are homogenously deposited across the surface, whereas irradiation with carbon ions causes local dose maxima, which are several orders of magnitude higher than the mean dose. As the LET decreases with increasing energies, the local dose maxima are less pronounced than at lower energies.

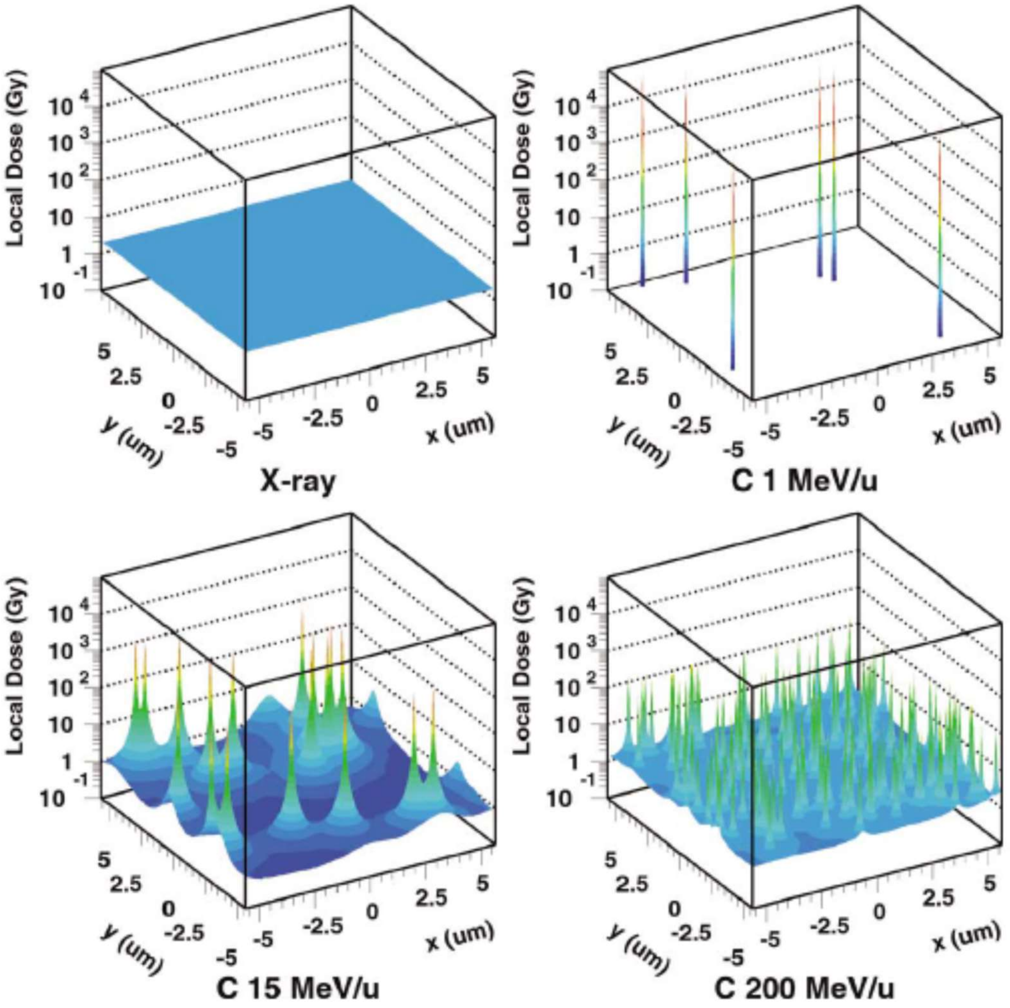

Figure 3: Microscopic dose distribution of X-rays and carbon ions. The average dose is 2 Gy in each case with different energies. The size of the area is 10 x 10 μm^2 and corresponds to the typical size of mammalian cell nuclei. Reprinted from (Krämer, Weyrather, & Scholz, 2003).

1.2. Biological Effects of Ionizing Irradiation

The interaction between IR and matter is based on underlying physical properties (photons or charged particles), LET, cell type and other factors. Therefore, a brief overview on the different levels of responses to IR will be introduced in this section. Radiation damage can cause a variety of responses, ranging from physiochemical to tissue damage, leading to acute and chronic effects. DNA is considered as the most sensitive target of irradiation as it represents all genetic data in only little redundancy. IR can cause DNA damage in direct or indirect manner (Hall & Giaccia, 2006; Reece & Urry, 2011). As depicted in Figure 4, interaction of irradiation with DNA is termed direct action. The indirect action is described in the same figure and is based on interaction of ionizing irradiation with water. Because water is the most abundant molecule in cells (80 % volume in mammalian cells), it is stochastically the most probable interaction partner for IR. The ionization of water molecules leads to formation of highly reactive water radicals, a process termed as radiolysis. Subsequent diffusion and interaction of water radicals lasts only a few µs or less and can also lead to DNA damage. Because of this intermediate step for DNA damage, this effect is termed as indirect action (Hall & Giaccia, 2006).

DNA damage can manifest as breaks of the sugar phosphate backbone, which can develop into more severe damage, or as chemical modification of bases. Breaks of the sugar phosphate backbone can result in single strand breakage (SSB) or, if both strands are affected, in double strand breakage (DSB). So far, all interactions were of physical and chemical nature (Hall & Giaccia, 2006). One of the first cellular responses to DNA damage is DNA repair. Due to errors during DNA repair, changes of genetic information might be introduced eventually causing mutations. As modifications and SSBs are usually easier to repair, the most crucial damage for cells is the DSB as it is more likely to cause mitotic failure and consequent cell death. Depending on the DNA repair pathway for DSB, incorrect rejoining of DNA strands can introduce chromosomal aberrations and later chromosomal instability, which is considered as risk factor for cancer development (Hall & Giaccia, 2006; Iliakis, 1991).

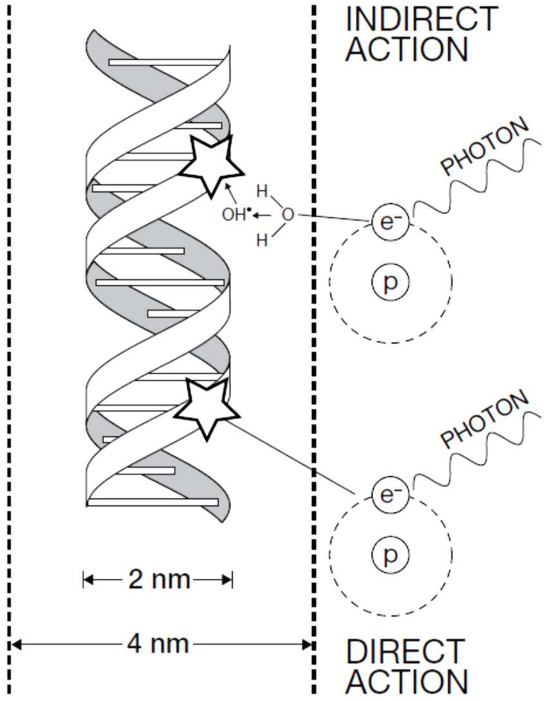

Figure 4: Direct and indirect interaction of ionizing irradiation with DNA as the sensitive target. Reprinted from (Hall & Giaccia, 2006).

In addition to the repair of DNA damage like SSB and DSB, DNA repair factors also interfere with other aspects of the cellular responses, such as cell cycle, cell death, metabolism, inflammation etc. (Hall & Giaccia, 2006). On a tissue level, the most acute radiation induced effect is the inactivation of targeted cells, finally leading to functional defects or even tissue failure. Tissues with high proliferating activity such as the gastrointestinal tract, skin and bone marrow are often termed radiosensitive because first detrimental effects can already be observed after very low doses (<1 Gy x-ray) (Hall & Giaccia, 2006). In contrast, radioresistant tissue is characterized by slow proliferation activity and can tolerate doses up to 50 Gy. Historically, examples for radioresistant tissue in radiobiology are spinal cord, brain, lung, heart and other mainly postmitotic tissues. Besides the proliferation rate, tissue architecture and irradiated volume are contributing factors for the induction of radiation damage (Hall & Giaccia, 2006; Karger, Peschke, Sanchez-Brandelik, Scholz, & Debus, 2006; Schultz-Hector & Trott, 2007).

One of the most common longterm irradiation damage is fibrosis, which can develop until years and decades after irradiation exposure (Adams, Hardenbergh, Constine, & Lipshultz, 2003; Heidenreich & Kapoor, 2009; Schultz-Hector & Trott, 2007; Taunk, Haffty, Kostis, & Goyal, 2015): As discussed above, first responses often involve cell death in different forms, ranging from apoptosis, necrosis to autophagy (Hall & Giaccia, 2006; Tam, Wu, & Law, 2017). Most of these cell death types are linked to inflammation, which manifests e.g. as infiltration of immune cells and cytokine release (Libby, P.; Ridker, P. M.; Hansson, 2011; Libby, 2002; Taunk et al., 2015). Inflammation is one step in wound healing, which needs to be strictly regulated. If it is not, chronic inflammation may persist and lead to the manifestation of fibrosis or other defects (Wynn, 2004).

For the comparison of biological effects upon interaction of different radiation qualities, the term of relative biological effectiveness (RBE) was introduced. The RBE serves as a quantitative parameter for realizing the same biological outcome for exposure of different radiation qualities (Hall & Giaccia, 2006). As depicted in Equation 3, it is defined as the dose of a reference radiation quality, classically x-ray, $D_{\text{x-rays}}$ divided by the dose of the untested radiation quality D_{test} for the same effect (Hall & Giaccia, 2006; Krämer et al., 2003). The specific RBE of carbon ion irradiation is usually higher than photon irradiation, but depends on the biological endpoint.

$$\mathrm{RBE} = \frac{D_{X-ray}}{D_{test}}\Big|_{iso-effect}$$

Equation 3: Calculation of the RBE (Krämer et al., 2003).

1.3. Application of Radiotherapy

Radiotherapy with photons and carbon ions is one of the current therapy options to inactivate target tissue, which was also applied for cardiac ablation. The main limitation of radiotherapy is damage in non-targeted tissue. Such damage can appear in tissue surrounding the target or exposed in entrance channel regions and lead to side effects. Therefore, different approaches for highly conformal therapy and sparing of normal tissue during charged particle irradiation are evinced in the following sections.

Anyway, the foremost advantage of radiotherapy with charged particles is their unique depth profile. As depicted in Figure 2, this profile allows for optimal sparing of normal tissue during treatment. As the Bragg peak comprises the location of the maximum RBE, most effective dose deposition can be applied to target volume (Schardt, Elsässer, & Schulz-Ertner, 2010).

The application of charged particle beams are realized with two main shaping techniques of pencil beams: Passive and active beam delivery. Both provide delivery of conformal and homogeneous treatment. In addition, the shaping of a lateral and longitudinal beam is necessary to accomplish homogenous dose application to the whole target volume as spread-out Bragg peak (SOBP): Target irradiation comprises virtual subdivision of its volume into several layers. Every layer is exposed with different energies of a charged particle beam. This energy stacking results in an extended uniform dose region in depth, which is known as SOBP (Hall & Giaccia, 2006). Nowadays, active scanning systems are preferred as they provide superior dose conformity. Further optimizations of radiotherapy are realized with 4D treatment planning for the irradiation of moving targets.

1.3.1. Active Beam Delivery

During radiotherapy with charged particles, highly conformal depth dose delivery is realized by the deflection of the beam via dipole magnets in an active beam delivery system. This method offers several advantages, because there is no need for patient-specific hardware in front of the beam line, which leads to a reduction of additional neutron dose (T Elsässer, Gemmel, Scholz, Schardt, & Krämer, 2009; Krämer et al., 2003).

The application of this method is based on the virtual separation of the target into several layers. Every layer corresponds to the same depth dose of beam energy as it is extracted from the synchroton accelerator. Furthermore, every layer is subdivided into a grid. Magnetic reflection of the beam allows for horizontal and vertical adjustment of the beam. At every raster point within the grid a predetermined number of particles is deposited (Figure 5). This method allows integrating a variable RBE in the planning process. Fully active 3D scanning system with spill-by-spill energy variation and scanning in vertical and horizontal direction are offered by raster scanning approach as it was developed at GSI (Grözinger et al., 2006; Kaderka et al., 2012; Krämer, 2009).

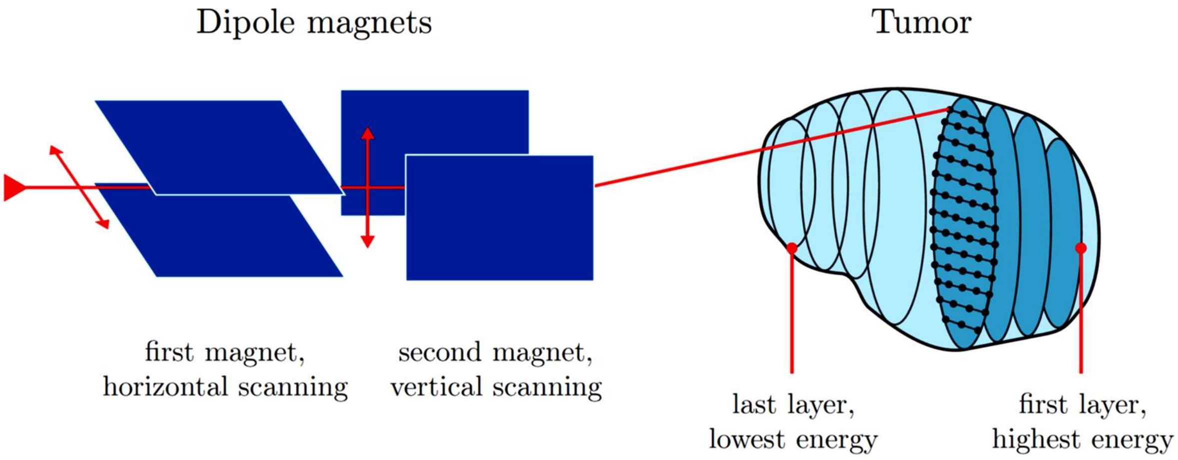

Figure 5: Active beam delivery and raster scanning for carbon ions as developed at GSI. Reprinted from (Krämer, 2009).

1.3.2. Treatment of Moving Targets Using 4D Treatment Planning

Radiotherapy of static target has improved within the last decades and is well established for several applications. However, irradiation of a moving target is still challenging and remains a major research field for photon and particle therapy. The irradiation of moving types can cause dose blurring or deformed dose distribution, because the target is partly moving out of the field. Interference effects, so-called interplay effects, between motion of the target and the scanned pencil beam, can produce local over- and under-dosage in the target volume and additional exposure of normal tissue (Bert, Grozinger, & Rietzel, 2008; Grözinger et al., 2006). The motion of moving targets can be compensated with different mitigation strategies (Bert & Durante, 2011). They are based on reducing patient movement during treatment and enlargement of target volume in the course of treatment planning. These methods comprise rescanning, gating and tracking of target volume:

- Rescanning refers to the irradiation of each raster point repeatedly with corresponding lower doses than exposure of raster points with the total dose at once as described above. This way, inhomogeneous dose application due to interplay effects is statistically averaged.
- Gating describes target irradiation during a part of the motion circle with small amplitude. Irradiation is only applied, if target volume is within this small window. Because beam extraction needs to be repeatedly started and stopped, prolonged treatment time is caused.
- Tracking is based on implantation of electromagnetic transponder signals, which can be imaged easily. Consequently, the irradiation field is applied to the location of marker signals and does not rely on further image-guidance.

Before the application of mitigation strategies, the target and organs at risk (OAR) are outlined on a CT image by a physician. For a more precise contouring, positron emission tomography (PET) and magnetic resonance imaging (MRI) give additional information of the target. The sparing of normal tissue, in particular OAR, during radiotherapy requires an exact definition of the beam entry angles and beam parameters. For particle therapy, the complexity of treatment planning is added due to the consideration of several factors such as RBE and fragmentation of projectile and target. Based on TRiP98, a dedicated treatment planning system for particle therapy (Thilo Elsässer et al., 2010; Krämer, 2009), an upgraded TRiP4D comprising a 4D version was performed by the Group of C. Graeff (Eichhorn, 2016).

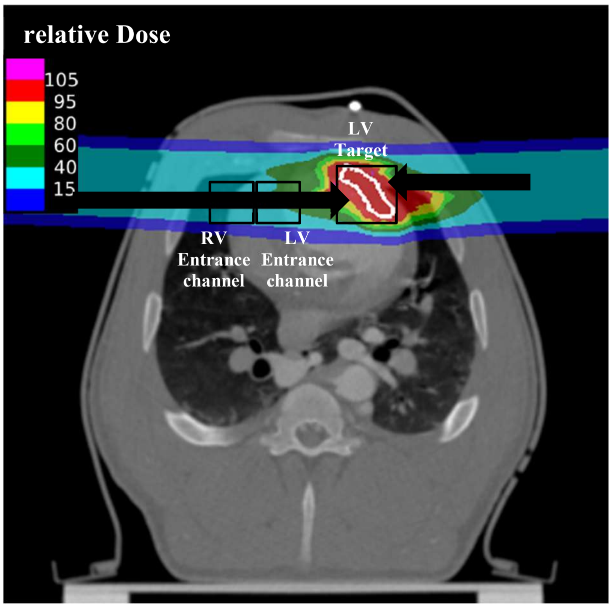

Figure 6: CT scans of the heart with exemplary dosecuts from the axial (left) view of a left ventricular target irradiated with a dose of 40 Gy. Modified from (Erbeldinger et al., 2015).

This improvement of accelerated ion therapy, in particular if it is actively delivered, can increase the dose conformity as it is very sensitive to target motion. This is achieved by using time-resolved computed tomography (4DCT), which allows for the comprehension of a single motion cycle. Before the treatment planning, 4DCT are divided into ten motion phases, either based on amplitude or phase. From these, one reference phase is selected and the others are registered to it. This process comprises image registration either between different motion phases or between different image modalities, for example contrasts CT to native CT or CT to MRI, can be deduced. The results are so-called deformation maps, which specify the transformation of every voxel between each motion phase and the reference phase (Gemmel, Rietzel, Kraft, Durante, & Bert, 2011; Richter, 2012). Accordingly, the irradiation of cardiac substructures was based on these plans, of which effects were investigated in the presented thesis.

1.4. General Structure of the Cardiovascular System

The effects of irradiating heart tissue with carbon ions might lead to an impairment of cardiac functions, which are the driving force of the cardiovascular system. In order to comprehend possible effects, the structure of the heart and its significance for the cardiovascular system will be described in the following sections. The cardiovascular system itself can also be divided into two constituents, the systemic and pulmonary circulatory system. In the systemic circulatory system, nutrient and oxygen rich blood is pumped by the heart from its left side into arteries, that branch into arterioles and finally capillaries, which interchange metabolites in tissue. After their passage through the body, capillaries merge into venules and veins, transporting the deoxygenated blood into the right heart side. From there, blood is pumped into the lungs, where it is oxygenated again and transported into the left heart side, restarting the cycle (Schmidt & Lang, 2007).

1.4.1. Heart Structure and Physiology

As one integral part of the cardiovascular system, the heart is a hollow muscle that pumps blood into organs. Its structure is based on four chambers, two on each side, which are termed atria and ventricles (Figure 7). The blood flow between the chambers of each side of the heart and the following arteries are controlled by heart valves. The heart valves are embedded in valve rings. This structure consists of connective tissue, hence it is impermeable for electrical propagation except for components of the conduction system (Schmidt & Lang, 2007).

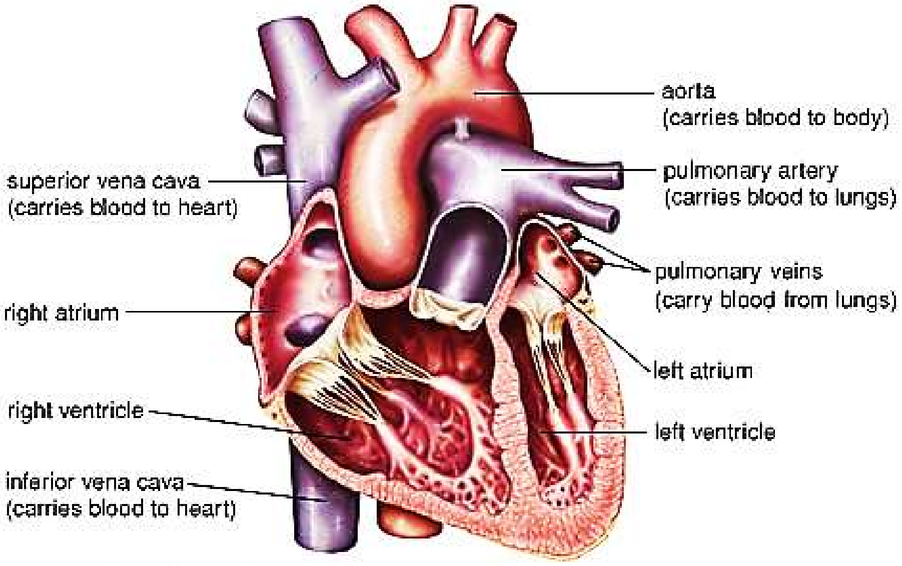

Figure 7: Structure of the heart. Reprinted from (Britannica, 2006).

In cardiac cross-sections, its subdivision into three layers are observable, which are the endocardium, myocardium and epicardium (Figure 8A). The endocardium describes the inner lining of the heart, which is in contact with blood flow. It consists of endothelial cells (EC) and contributes actively against coagulation (Schmidt & Lang, 2007).

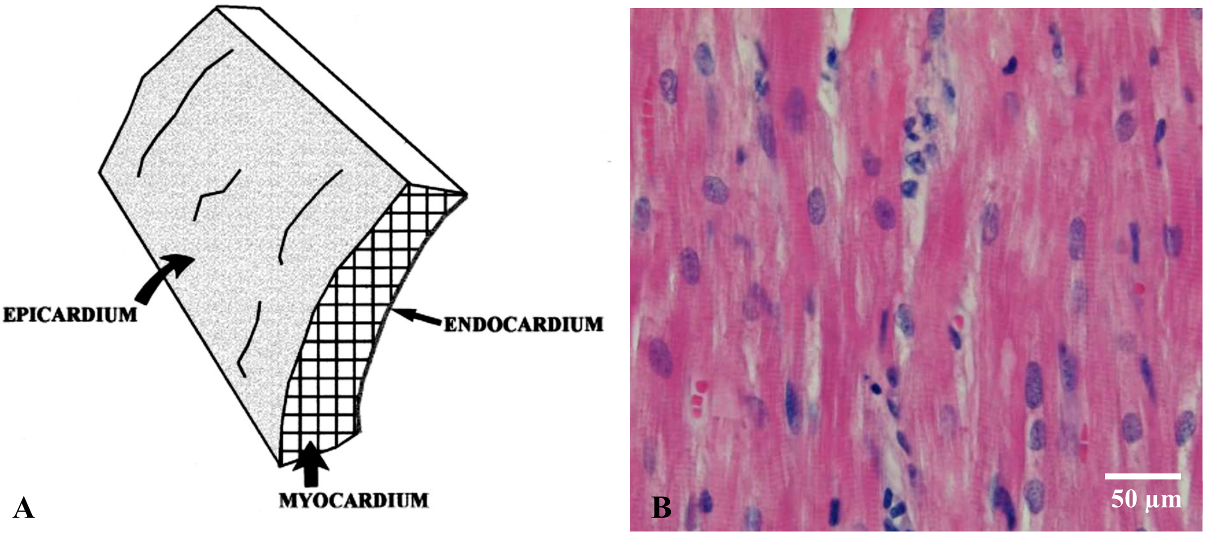

Figure 8: A cross-section through the heart shows that it consists of three layers (A). Reprinted from (Crick, Sheppard, Ho, & Anderson, 1999). The contraction of the middle layer, myocardium, is generated by cross–striated cardiomyocytes, here shown in a longitudinal section (stained with H&E, B).

The myocardium represents the main cardiac muscle and consists of cross-striated, mainly mononuclear cardiomyocytes (Figure 8B). Mature cardiomyocytes are also referred to as cardiac muscle fibres (Schmidt & Lang, 2007). The structure of muscle fibres is ensured by cardiac connective tissue. These connective tissue fibres also facilitate an appropriate chemical environment, such as calcium, sodium, and potassium, for subsequent contraction. They consist of mainly elastic fibres of collagen type I and III and are subdivided into endo-, peri- and epimysium. The endomysium envelops individual muscle fibres and contains capillaries and nerves. Several muscle fibres are encapsulated by the perimysium representing a fascicle. Fascicles are finally enclosed by the epimysium, which protects muscle from friction (Schmidt & Lang, 2007). Although cardiomyocytes represent the largest part of the volume of the myocardium, only 30 % of all cells are cardiomyocytes. Apart from cardiomyocytes, the most abundant cells in the myocardium are EC (45 %) and fibroblasts (11 %), which are crucial for blood supply, electrical isolation and myocardial structure. The rest are other mesenchymal cells and resident immune cells (Talman & Ruskoaho, 2016).

The epicardium constitutes the outer lining and consists of connective and adipose tissue. The epicardium and subepicardium contain cardiomyocyte progenitor cells in hypoxic niches (Kocabas et al., 2012). Blood vessels and nerves supplementing the cardiac muscle enter from there. Between epi- and pericardium, pericardial fluid lubricates the heart, enabling contraction of the myocardium between these two layers. The pericardium protects the heart from friction with other organs (Schmidt & Lang, 2007).

1.4.2. Structure of Blood Vessels

The alimentation of cardiac tissue relies on a network of capillaries. Consequently, cardiac remodelling like fibrosis is associated with vascular damage. This circumstance is also observed in radiobiology, where vascular damage is associated with longterm effects after cardiac irradiation (Talman & Ruskoaho, 2016). In this section, the general structure of blood vessels and the functions of their components are introduced. The structure of a blood vessel (Figure 9) comprises three layers, the tunica intima, media and adventitia. The tunica intima represents the inner lining of a blood vessel, which is in direct contact with blood flow. Similar to the endocardium, the tunica intima consists of EC and actively contributes to blood pressure and prevents coagulation. According to its name, the tunica media is the middle layer of a blood vessel. It is separated from the intima by a basal layer and contains circumferentially arranged smooth muscle cells (SMC). Their main task is the regulation of vasodilation (Schmidt & Lang, 2007).

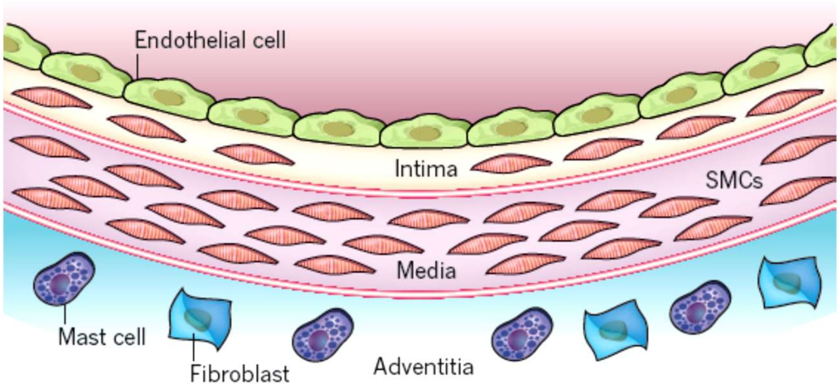

Figure 9: Structure of a blood vessel. Reprinted from (Libby, P.; Ridker, P. M.; Hansson, 2011).

The outer layer is tunica adventitia and functions as integration of a blood vessel into the respective organ tissue. It consists of connective tissue, e.g. fibroblasts and collagen fibres (Schmidt & Lang, 2007). Based on the vascular type, the thickness of the tunica media and adventitia can vary. In capillaries, which are in direct contact with the tissue and therefore directly provide gas and metabolite exchange, only EC are present on a basal layer. The EC in capillaries are supported by pericytes, contractile cells of the connective tissue. (Schmidt & Lang, 2007). Capillaries are the most radiosensitive target of the cardiovascular system. Accordingly, their damage has direct consequences for the supplied tissue (Fajardo & Stewart, 1971; Hopewell et al., 1986).

1.5. The Cardiac Conduction System

The function of the heart is based on its contraction providing continuous blood flow throughout the whole body. The content of this section exemplifies the structure and the main components of the cardiac conduction system as well as their functions. Furthermore, the comprehension of this system is crucial for the treatment of cardiac arrhythmias.

The contraction of the heart is based on the propagation of electrical impulses through different cell types, mainly cardiomyocytes and nerve cells. Modulating influences are sympathetical and parasympathetical innervation and hormones. However, the heart muscle contains two types of cardiac muscle fibres: pacemaker and contractile (non-pacemaker) cells. As pacemaker cells are more specialized, they generate spontaneous electrical impulses. In turn, non-pacemaker cells are activated by the impulses of pacemaker cells (Schmidt & Lang, 2007). Signal transduction between cells is mediated by so-called gap junctions, protein channels between cells for ion and metabolite exchange. The most prominent gap junction proteins in cardiac tissue are connexin (Cx)40, Cx43 and Cx45. They mediate signal transduction between cardiomyocytes and other cell types of the myocardium like fibroblasts (Schmidt & Lang, 2007; Talman & Ruskoaho, 2016).

The comparison of pacemaker and non-pacemaker cells shows that pacemaker cells are more voluminous and present less contractile elements and mitochondria. They also contain more glycogen and enzymes for anaerobic energy metabolism. Consequently, pacemaker cells are mainly located in the sino-atrial node (SAN) and atrio-ventricular node (AVN). Non-pacemaker cells instead represent the most abundant type of cardiomyocytes in the heart (Schmidt & Lang, 2007).

The course of cardiac impulse propagation, which starts at the SAN, is illustrated in Figure 10. The SAN is positioned in the inside of the posterior right atrial (RA) wall. Electrical impulses from SAN stimulate contraction of both atria and subsequently enter into the AVN, which is either activated through impulses from the SAN or spontaneously by itself. The valve rings prevent any impulse propagation, which is not induced by AVN. From there, a small bundle of specialized cardiomyocytes, the bundle of His, branches into Purkinje fibres, thereby transmitting electrical signals through ventricles.

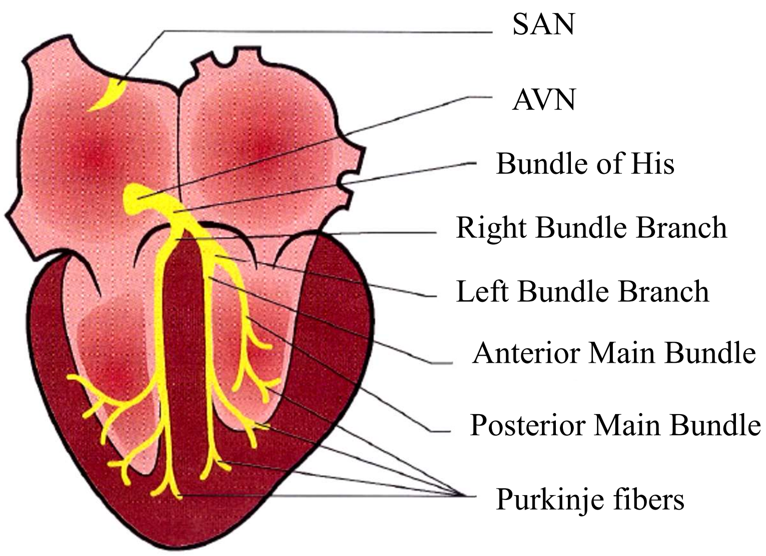

Figure 10: Scheme of the cardiac electrical conduction system (in yellow), which maintains the rhythmical contraction of the heart. The frontal view is shown. Modified after (Schmidt & Lang, 2007).

The SAN represents the fastest spontaneous depolarisation (60 – 80 times/minute). Therefore, it is referred to as primary pacemaker for electrical automatism in the heart. The AVN has a spontaneous depolarisation rate of 40 – 50 times/minute and the bundle of His 30 – 40 times/minute. Accordingly, they are stated as secondary and tertiary pacemakers of the heart (Schmidt & Lang, 2007).

1.6. Arrhythmias and Treatment

This section introduces the definition, assorted characteristics and standard treatment of CA. In addition, the risks of the standard treatment are presented, which motivated the investigations of cardiac ablation with carbon ion irradiation. CA are characterized by an irregular heart rate or disturbed spreading of electrical signals. The detection of CA can be performed with ECG measurements. Frequencies greater than 100 times/minute are referred to as tachycardia, which is most commonly caused by the activation of the sympathetic system. In contrast, bradycardia denotes frequencies below 50 times/minute (Schmidt & Lang, 2007). Persistent CA cause anatomical and electrical remodelling and are associated with increased risk for thromboembolism, heart failure (HF) and increased mortality. Based on their location, they are distinguished as supraventricular or ventricular. Most common supraventricular CA is atrial fibrillation (AF), which is characterized as chaotic contraction of the atria. They are mainly caused by the extension of the myocardial muscle sleeves of the left atrium into the PV (Calkins et al., 2012). However, AF usually does not transfer into ventricles and subsequently does not interfere with the cardiac pump capacity. In contrast, the tachycardiac fibrillation of ventricles (VT) is in conflict with normal heart rhythm as they cause ventricular filling and contraction in too short durations. The AV block is another prominent CA and defined as prolonged duration of the propagation of electrical signals from the atria to the ventricles. A disturbed impulse propagation in the ventricles can be caused by the blockage of bundle of His or dysfunction of myocardium due to ischemia (Calkins et al., 2012; Schmidt & Lang, 2007).

The occurrence of CA can lead to fatigue, shortness of breath, or chest pain. Their persistence is associated with higher stroke risk and heart failure causing increased mortality. Treatment options of CA require anti-coagulative and anti-arrhythmic drugs. Ventricular arrhythmias, such as AV block, can be handled by the implantation of a pacemaker. The standard treatment for long persisting CA is catheter ablation. This minimally invasive procedure requires the insertion of a catheter from femoral vein or artery into the heart. Arrhythmogenic structures are then ablated by the induction of transmural lesions. For this purpose, radiofrequency or cryothermal energy is applied. The lesion is caused by coagulative necrosis evolving into a non-conducting lesion. Optimal outcomes require transmural lesion formation. However, the application of radiofrequency or cryothermal energy carries risks for a number of complications. Although such complications are infrequent, they can be fatal and range from cardiac tamponade, PV stenosis, thromboembolism, etc. Limiting the power of the radiofrequency will prevent such collateral damage, but insufficient energy application might not cause a transmural lesion. Another drawback of this treatment is the recurrence of CA. Therefore, repeated cardiac ablation is required for 20 – 40 % of all patients (Calkins et al., 2012).

1.7. Radiation-Induced Heart Diseases

Longterm effects of cardiac irradiation were discovered after radiotherapy of thoracic tumours. Typical examples of such tumours are Hodgkin lymphoma and breast cancer. In the course of treatment, cardiac tissue is exposed to total doses of 35 – 40 Gy (given with a maximum of 2 Gy per fraction) (Adams et al., 2003; Schultz-Hector & Trott, 2007; Taunk et al., 2015). However, a significant and dose-dependent increase of cardiac mortality can be observed after the application of doses below 10 Gy (Schultz-Hector & Trott, 2007).

Animal models for RIHD displayed microvascular damage, such as loss of small vessels, haemorrhage and obstruction of lumen by microthrombi was an early effect. In addition, microvascular damage occurred before further structural changes and was claimed as initial event of cardiac fibrosis (Adams et al., 2003; Fajardo & Stewart, 1971; Hopewell et al., 1986; Schultz-Hector & Trott, 2007). According to Talman et al., Biernacka et al., as well as Fajardo and Stewart, the development of cardiac fibrosis can be divided into three stages, namely inflammation of damaged tissue, proliferation of myofibroblasts, and maturation of the scar. The first stage ("inflammation of damaged tissue") comprises inflammation due to vascular damage. Inflammatory reactions are triggered by cell death due to the malnourishment of the tissue. They involve the release of cytokines (TNFα, IL-1, IL-6, CRP, etc.) as well as the recruitment and infiltration of immune cells (Adams et al., 2003; Biernacka & Frangogiannis, 2011; Talman & Ruskoaho, 2016; Taunk et al., 2015).

The second stage ("proliferation of myofibroblasts") is marked by the suppression of pro-inflammatory signals, which recruited immune cells in the first stage. This is achieved by the release of anti-inflammatory (IL-10) and pro-fibrotic (TGFβ, IL-4 and IL-13) cytokines (Biernacka & Frangogiannis, 2011; Talman & Ruskoaho, 2016; Taunk et al., 2015; Wynn, 2004). Consequently, pro–fibrotic signalling leads to the dedifferentiation of several cell types, such as fibroblasts, SMC and mesenchymal stem cell like cells, into myofibroblasts. The infiltration and proliferation of activated myofibroblasts appears in parallel to the apoptosis of the previously infiltrated immune cells due to multiple molecular signals. Myofibroblasts produce excessive extracellular matrix (ECM) proteins like collagen, proteoglycans and fibronectin. This leads to an increased tensile strength of the heart wall. In addition, a microvascular network is established after the release of angiogenic signals from the surrounding tissue, which stimulates the proliferation and infiltration of EC (Biernacka & Frangogiannis, 2011; Talman & Ruskoaho, 2016; Wynn, 2004).

In the last stage ("maturation of the scar"), most of the myofibroblasts and vascular cells undergo cell death. This process causes the disintegration of previously formed microvasculature in the immature scar tissue. This last step in the development of cardiac fibrosis leaves a mature fibrous scar with only few myofibroblasts. Such a scar can be identified macroscopically (Biernacka & Frangogiannis, 2011; Fajardo & Stewart, 1971; Talman & Ruskoaho, 2016). This order of events is also termed as replacement fibrosis. It prevents the rupturing of cardiac tissue due to an altered composition (Biernacka & Frangogiannis, 2011; Talman & Ruskoaho, 2016).

Unlike wound healing, some myofibroblasts stay permanently activated even after repair of the affected cardiac tissue. They presumably cause the progression of damage to borderzones and remote areas. In addition, replacement fibrosis leads to increased mechanical stress and subsequent release of pro-fibrotic signals. The resulting spreading of cardiac fibrosis is known as reactive fibrosis (Biernacka & Frangogiannis, 2011; Talman & Ruskoaho, 2016; Taunk et al., 2015). Accordingly, fibrosis is one of the hallmarks of RIHD.

Most common RIHD are pericarditis, accelerated atherosclerosis of coronary arteries and cardiomyopathy: The development of pericarditis is only observed after irradiation of big volumes and characterized as oedematous swelling, fibrotic thickening and adhesions of epi– and pericardium. This condition can lead to cardiac tamponade and finally congestive heart failure (Adams et al., 2003; Heidenreich & Kapoor, 2009; Schultz-Hector & Trott, 2007; Taunk et al., 2015). Accelerated atherosclerosis comprises plaque formation and subendothelial fibrosis, which both cause the narrowing of diseased vessels and impaired vasodilation. As large plaques are unstable, they can rupture and therefore lead to MI or stroke (Adams et al., 2003; Heidenreich & Kapoor, 2009; Schultz-Hector & Trott, 2007; Taunk et al., 2015). Cardiomyopathy is clearly associated with spreading of fibrosis in heart tissue. Due to the progression of fibrosis, it is related to systolic and diastolic dysfunction, in particular if the left ventricle is affected (Adams et al., 2003; Heidenreich & Kapoor, 2009; Schultz-Hector & Trott, 2007; Taunk et al., 2015). Another side effect of heart irradiation is conduction abnormalities. In contrast to aforementioned RIHD, they are not well characterized, yet.

Risk factors for the incidence and severity of RIHD are irradiation of large volumes, younger age during treatment, concomitant application of chemotherapy, obesity and hypertension (Schultz-Hector & Trott, 2007). However, the irradiation of any relevant cardiac structure could not be linked to the development of specific RIHD (Wondergem, Boerma, Kodama, Stewart, & Trott, 2013).

1.8. Carbon Ion Irradiation of Small Volumes in a Porcine Heart

This thesis was carried out in frame of a project aiming for an alternative treatment method of cardiac ablation. In order to understand the aim of this thesis, the motivation, performance, and macroscopic results of this project are presented in the following section.

The current standard treatment for CA is catheter ablation of the anatomic substrates, which causes the CA. However, this minimally invasive method comprises a lacking efficacy and several risks, which can be fatal (Calkins et al., 2012). In contrast, high dosed external irradiation is non-invasive and limits the risk of complications. Additionally, the favourable properties of carbon ion irradiation are well established in cancer therapy. Its application with high volume conformity and thus low dose exposure to critical structures offers optimal conditions for novel treatment options (Kraft, 2000; Schardt et al., 2010).

Therefore, the application of high dosed carbon ion irradiation (25 – 55 Gy) was accomplished in a feasibility study. As the dimensions and architecture are similar to a human heart, the project was performed in a porcine model. Analogous to conventional catheter ablation, only small volumes (1 – 1.5 cm^3) were aimed to ablate. The feasibility of this approach was established before in isolated porcine hearts under Langendorff-perfusion (Lehmann et al., 2015).

For this innovative treatment method, two clinically relevant structures for cardiac ablation were irradiated. The first target is the LV. It represents the thickest part of the heart muscle and is usually ablated in case of VT. Due to its thickness, conventional catheter ablation often fails to penetrate the whole tissue. Therefore, transmural scar formation can often not be accomplished. The second target was the AVN. Ablation of the AVN is clinically performed in severe cases of AF. The electrophysiological endpoint for this target is an AV block. The irradiation of targets was realized with an exemplary 4D-treatment plan for dose deposition including rescanning of contoured targets. Online- positron emission tomography (PET) scans confirmed precise target irradiation (Lehmann et al., 2016).

Electrophysiological changes were detected in target areas three and six months after irradiation. Anyhow, lesion formation was not transmural for either target group. In addition, the scar formation was heterogeneously distributed and inter-individually differing radiation responses were detected. Gross macroscopic investigations indicated signs of haemorrhage and inflammation side by side with fibrosis. First results indicated cell death, haemorrhage and inflammation. The macroscopic inspection of entrance channel and outfield regions did not point to the occurrence of damage in these areas, which would be a limiting factor of these investigations (Lehmann et al., 2016).

To summarize, cardiac ablation with high dosed carbon ions causes several tissue responses. However, it did not lead to mature or transmural scar tissue in the target areas. In addition, the effects to entrance channel and outfield regions were not characterized yet. These findings motivated the investigations of microvascular damage in target, entrance channel and outfield regions as they might give hints on ongoing tissue remodelling.

1.9. Objective of this Thesis

Cardiac irradiation can lead to longterm effects like the development of fibrosis and electrophysiological changes. Such implications were identified in cancer patients after radiotherapy and A bomb survivors as RIHD. Investigations in animal models indicated vascular damage as initial event for these diseases. In these settings, large volumes or even the whole hearts were exposed to IR. The applied doses range from low (A bomb survivors), to medium (animal experiments), to eventually high (cancer patients) (Adams et al., 2003; Fajardo & Stewart, 1970; Schultz-Hector & Trott, 2007; Seemann et al., 2012; Washington, Jeffords, Rodrigues, Ma, & Das, 2013). Comparably, the link between the development of cardiac fibrosis and vascular damage were also identified in MI patients and corresponding animal models (Dusek, Rona, & Kahn, 1971; Meyer, Hodwin, Ramanujam, Engelhardt, & Sarikas, 2016; Virag & Murry, 2003).

This thesis was performed as a part of the aforementioned project (1.8) described by Lehmann and co-workers. Within this project, high dosed carbon ion irradiation of cardiac substructures led to incomplete scar formation in parallel to early events of tissue remodelling in target areas (Lehmann et al., 2016). These results indicate persistent tissue remodelling. The occurrence of microvascular damage confirms this indication.

Accordingly, this thesis aimed to characterize precedent and ongoing manifestations of microvascular damage. Furthermore, the implications of vascular damage on tissue remodelling were investigated. These studies were elaborated in scar and muscle tissue in parallel to identify different stages of tissue remodelling. In particular, the effects of carbon ion irradiation with high doses in target areas and medium doses in entrance channel regions were studied. These findings gave hints on the progression of cardiac fibrosis after different doses and on potential threshold doses for several effects. These results were complemented with examinations on cell death, hypoxia and inflammatory mediators to understand underlying molecular mechanisms.

Moreover, late effects of vascular damage might lead to the spreading of damage to precedent unaffected tissue (Baldi et al., 2002; Dusek et al., 1971; Talman & Ruskoaho, 2016; Virag & Murry, 2003). Therefore, the detection of reactive fibrosis in outfield regions of the heart was another crucial aspect of this thesis.

2. Material and Methods

2.1. Materials

2.1.1. Chemicals

Name	Manufacturer
Acetone	Roth, Karlsruhe, Germany
Acid fuchsin	Roth, Karlsruhe, Germany
Basic fuchsin	Roth, Karlsruhe, Germany
Citric acid	Roth, Karlsruhe, Germany
Ethanol ROTIPURAN® _99,8 %,	Roth, Karlsruhe, Germany
Eosin	Sigma, Steinheim, Germany
Eukitt®	Sigma, Steinheim, Germany
Ferric chloride	Merck, Darmstadt, Germany
Formaldehyde solution, 37 %	Sigma, Steinheim, Germany
Glacial acetic acid	Sigma, Steinheim, Germany
Glycerol	AppliChem,Darmstadt, Germany
Goat serum	Thermo Scientific, Frederick, Maryland
H_2O_2-Solution, 30 %	Sigma, Steinheim, Germany
Haematoxylin	Roth, Karlsruhe, Germany
Isopropanol	Roth, Karlsruhe, Germany
Mayer´s Hematoxylin solution	Roth, Karlsruhe, Germany
Hydrochloric acid (HCl) 37 % smoking, for analysis	Merck, Darmstadt, Germany
Iodine	Sigma, Steinheim, Germany
Nuclear fast red	Roth, Karlsruhe, Germany
Paraffin	Merck, Darmstadt, Germany
Picric acid	Sigma, Steinheim, Germany
Potassium alum	Sigma, Steinheim, Germany
Potassium chloride	Merck, Darmstadt, Germany
Potassium ferrocyanide ($K_4[Fe(CN)_6]$)	Roth, Karlsruhe, Germany
Potassium hydrogenphosphate (KH_2PO_4)	Merck, Darmstadt, Germany
Potassium iodide	Merck, Darmstadt, Germany
Sodium citrate	Merck, Darmstadt, Germany
Sodium chloride	AppliChem,Darmstadt, Germany
Sodium hydrogenphosphate (Na_2HPO_4)	Merck, Darmstadt, Germany
Sulphuric acid (H_2SO_4, 96 %)	L+S-Labor, Bad Bocklet, Germany
Tween 20	Sigma, Steinheim, Germany
Xylol	Roth, Karlsruhe, Germany

2.1.2. Buffer und Solutions

Buffer or Solution	Composition
0.1 % basic fuchsin	0.5 g basic fuchsin 500 ml aqua dest.
1 % aqueous acid fuchsin	1 g acid fuchsin 1 ml acetic acid 100 ml aqua dest.
2 % aqueous ferric chloride	36 ml 10 % aqueous ferric chloride 144 ml aqua dest.
5 % alcoholic haematoxylin	25 g haematoxylin 500 ml 100 % ethanol Dissolved with gentle heat, the filtered and kept 4 weeks for oxidation before usage for oxidation
5 % HCl	67.5 ml HCl 432.5 ml aqua dest.
5 % potassium ferrocyanide	25 g $K_4[Fe(CN)_6]$ 500 ml aqua dest.
10 % aqueous ferric chloride	40 g ferric chloride 400 ml aqua dest.
Blocking solution	135 µl goat serum 100 µl Tween 10 ml PBS
Citric buffer pH 6 10x	14,7 g sodium citrate 10,5 g citric acid 500 ml aqua dest.
Citric buffer pH 6 1x	100 ml citric buffer pH 6 10x 900 ml aqua dest.
Ehrlich´s haematoxylin solution	1 g haematoxylin 50 ml isopropanol 50 ml aqua dest. 50 ml glycerol 7,5 g potassium alum 5 ml acetic acid Kept for at least 4 weeks before usage for oxidation
ELISA – washing buffer	500 µl Tween-20 1000 ml PBS (1x)
ELISA stop solution (2N H_2SO_4)	5,6 ml sulphuric acid (96 %) 94,4 ml aqua dest.
Nuclear fast red	25 g aluminium sulphate 0.5 g nuclear fast red 500 ml aqua dest. Dissolved with gentle heat, then filtered

PBS (pH 7,4) 10x	160 g NaCl 4 g KCl 28,8 g Na_2HPO_4 4,8 g KH_2PO_4 2000 ml aqua dest.
PBS 1x	100 ml PBS 10x 900 ml aqua dest.
Van Gieson solution	28 ml 1 % aqueous acid fuchsin 154 ml saturated aqueous picric acid
Verhoeff´s working solution	100 ml 5 % alcoholic haematoxylin 40 ml 10 % aqueous ferric chloride 40 ml Weigert´s iodine solution
Weigert´s iodine solution	8 g potassium iodide 4 g iodine 400 ml aqua dest.

2.1.3. Antibodies

Name	**Manufacturer**	**Catalog number**
Active caspase 3	Cell Signaling, Denver, Colorado	#9661
Active caspase 3	R&D systems, Minneapolis, Minnesota	AF - 835
CD31	Abcam, Cambridge, UK	Ab28364
CD34	Abcam, Cambridge, UK	Ab81289
Complement factor 9	Leica Biosystems, Newcastle, UK	NCL-CCC9
HIF-1α	Abcam, Cambridge, UK	Ab16066
S100a	Abcam, Cambridge, UK	Ab11428
S100b	Abcam, Cambridge, UK	Ab41548
TUNEL	Millipore, Temecula, California	S7101
vWF	Millipore, Temecula, California	AB7356
Biotinylated affinity-purified goat anti-rabbit IgG	Thermo Scientific, Frederick, Maryland	#32054
Biotinylated affinity-purified horse anti-mouse IgG	Thermo Scientific, Frederick, Maryland	#31806

2.1.4. Kits

Name	Manufacturer	Catalog number
DuoSet Ancillary Reagent Kit 2	R&D systems, Minneapolis, Minnesota	DY008
Human IL-6 ELISA Ready-SETGo!®	eBioscience, Wien, Österreich	88-7066-86
Human IL-8 ELISA Ready-SETGo!®	eBioscience, Wien, Österreich	88-8086-86
Human MCP-1 ELISA Ready-SETGo!®	eBioscience, Wien, Österreich	88-7399-86
Porcine C-reactive protein DouSet ELISA Kit	R&D systems, Minneapolis, Minnesota	DY2648
Porcine HMGB1 ELISA Kit	IBL, Hamburg, Germany	ST51011
Porcine IFNγ ELISA Kit	Invitrogen, Camarillo, California	KSC4022
Porcine IL-1β ELISA Kit	Thermo Scientific, Frederick, Maryland	ESIL1B
Porcine IL-4 ELISA Kit	Invitrogen, Camarillo, California	KSC0042
Porcine IL-6 ELISA Kit	Thermo Scientific, Frederick, Maryland	ESIL6
Porcine IL-8 ELISA Kit	Invitrogen, Camarillo, California	KSC0082
Porcine IL-10 ELISA Kit	Invitrogen, Camarillo, California	KSC0102
Porcine TNFα ELISA Kit	Thermo Scientific, Frederick, Maryland	EP2TNFA2
Porcine TNFα ELISA Kit	Invitrogen, Camarillo, California	KSC3012
Porcine troponin t ELISA Kit	Cloud clone, Houston, Texas	SED232Po
Porcine vWF ELISA Kit	Cloud clone, Houston, Texas	CEA833Po
SIGMAFAST®3,3-diaminobenzidine tablets	Sigma, Steinheim	D4293-50
Ultra-Sensitive ABC Peroxidase Rabbit IgG Staining Kit	Thermo Scientific, Frederick, Maryland	32054
Ultra-Sensitive ABC Peroxidase Mouse IgG Staining Kit	Thermo Scientific, Frederick, Maryland	32054

2.1.5. Devices

Name	Manufacturer
Absorption reader for microplates EL 808	BioTek, Bad Friedrichshall, Germany
Analytical balance H51	Sartorius AG, Göttingen, Germany
Block heater HB-2	Wealtec Corp., Sparks, Nevada
Centrifuge	Heraeus, Hanau, Germany
Fridge	Liebherr, Hamburg, Germany
Leica TCS SPE microscope	Leica Microsystems, Mannheim, Germany
Light microscope BX61	Olympus, Hamburg, Germany
Paraffin oven UN 30 PLUS	Memmert GmbH, Schwabach, Germany
Photo camera E-330	Olympus, Hamburg, Germany
Pipettes	Eppendorf, Hamburg, Germany
Precision balance	KERN, Munich, Germany
Rotation microtome RM2235	Leica Microsystems, Wetzlar, Germany
Rotating shaker Unimax 1010	Heidolph Instruments, Schwabach, Germany
Slide Drying Bench MH6616	Electrothermal, Staffordshire, UK
Water bath M20 E100	Lauda, Lauda-Königshofen, Germany

2.1.6. Consumables

Name	Manufacturer
Centrifuge tubes 15ml	TPP, Edinburgh, GB
Centrifuge tubes 50ml	TPP, Edinburgh, GB
Cover slips 24 x 24 mm	Roth, Karlsruhe, Germany
Glass slides StarFrost	Knittel Gläser, Babenhausen, Germany
Gloves, Latex rotiprotect	Roth, Karlsruhe, Germany
Gloves, Nitril Format blue	Unigloves, Troisdorf, Germany
MaxiSorp® flat-bottom 96 well plate	Sigma, Steinheim, Germany
Pasteur pipettes, plastic	Roth, Karlsruhe, Germany
Pasteur pipettes, glas	Hirschmann, Fluorn-Winzeln, Germany
Pipette tips 10 – 100 μl	Brand, Wertheim, Germany
Reaction tubes 0.5 - 2 ml	Eppendorf, Hamburg, Germany
S-Monovette 7.5 ml K3E (EDTA)	Sarstedt, Nümbrecht, Germany
S-Monovette 7.5 ml Z-Gel (Serum)	Sarstedt, Nümbrecht, Germany
Wipes Kimwipes Lite 100	Kimberly Clark

2.1.7. Software

Name	Manufacturer
Microsoft Office 2007	Microsoft
Image J	National Institutes of Health
Prism7.02	Graph Pad

2.1.8. Animals

In total, 16 pigs (*sus scrofa domestica*) were included in this study, 14 of them were prepared for irradiation and 2 pigs were kept as a control group. Except for the irradiation procedure, the animals were kept at the 'Interfakultäre Biomedizinische Forschungseinrichtung' (IBF) of the University Clinic Heidelberg (UCHD). Due to vascular obliteration, one pig was not available for investigations (Pig L, AVN 40 Gy). Another one suffered from cardiac malformation and was therefore excluded from further analyses (Pig Q, LV 40 Gy). As the standard treatment of care is performed in patients, who already underwent implantation of a pacemaker, pigs underwent implantation of pacemakers before AVN targeted carbon ions irradiation, accordingly. Three pigs had to be euthanized before the end of the experiment due to the inflammation of the pacemakers (Pig K AVN 25 Gy, Pig J AVN 40 Gy, and Pig M AVN55 Gy). At the time of irradiation, all pigs were about 10 weeks old and weighed between 29 and 39 kg. The animals were randomly separated in two groups corresponding to two different target volumes, which were 1 cm^3 for the AVN target and 1.5 cm^3 for the LV target.

2.2. Methods

2.2.1. Carbon Ion Irradiation and Treatment Planning

The irradiation was applied in a single-fraction treatment. The dose groups were randomly assigned and were chosen based on findings of previous photon studies: permanent alteration of the electrical pathways, which is referred to as ablation, were at least 25 to 70 Gy X-rays (Bode et al., 2015; Sharma et al., 2010) and 25 to 100 Gy β-irradiation (Franceschi et al., 2012). These findings motivated the application of 25, 40 and 55 Gy for the AVN target group to carry out a dose escalation study. For the LV target group, only 40 Gy were applied to induce lesion formation. In parallel, this dose ensured, that the doses deposited in the organs at risk (OAR) surrounding the heart were as low as possible to avoid radiation-induced side effects.

The irradiation procedure was prepared with the treatment planning system TRiP4D, which was developed at GSI for ion therapy. This software is capable of calculating 4D dose distributions and can incorporate different motion mitigation techniques in the planning process for particle therapy (Richter, 2012). The raster point distance in horizontal and vertical direction was selected to be 2 mm with a distance of 3 mm between two iso-energy slices (IESs). Every raster point received a minimum number of 75,000 particles as a rescanning scheme with up to 15 rescans. In addition, this number of particles ensured position and intensity feedback from the treatment control system for successful irradiations at GSI. However, due to limited irradiation time, the number of particles per raster point was adapted up to 125,000 particles, if necessary. All irradiations were planned using two opposing horizontal fields with angles of 90° and 270°. This approach was selected, because it reduced the sensitivity to slight displacements and deformations of the heart due to the heartbeat or positioning uncertainties and therefore ensured the robustness of the treatment. Further details of the treatment planning were described elsewhere (Eichhorn, 2016).

In the course of the LV target irradiation procedure (Figure 11A), two horizontal pencil beams were applied. The beam from the right side penetrated the right ventricle (RV), then part of LV before it reached the LV target. Therefore, the irradiation setup generated RV and LV entrance channels from one irradiation field. In case of the AVN target irradiation (Figure 11B), the pencil beams traversed the left and right atrial appendage before they hit the target area. The doses deposited in the entrance channel regions were estimated other studies of this project. Accordingly, medium doses (7 - 17 Gy) were deposited in entrance channel regions (A. Eichhorn, C. Graeff, and J. Wiedemann, GSI, personal communication)

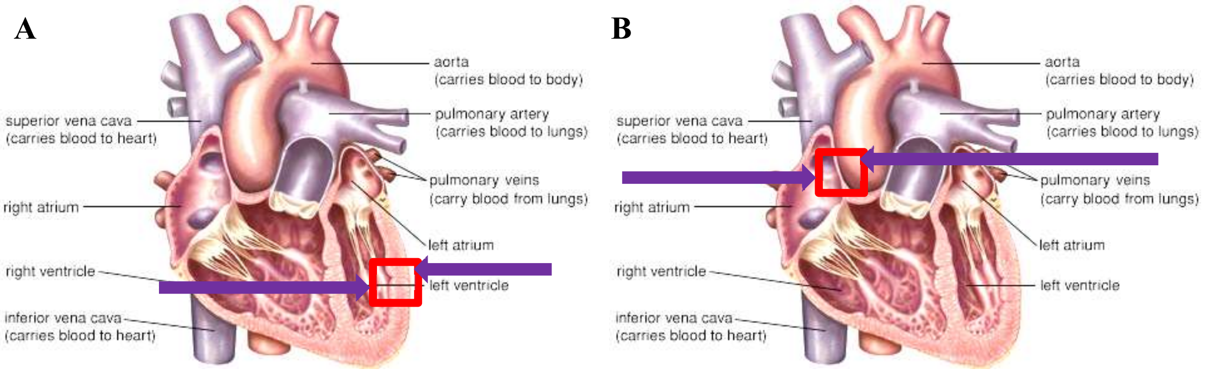

Figure 11: Scheme of target irradiation of the LV (A) and the AVN (B). The target is marked with red outline. The beam entrance channels through right and left heart side are shown as purple arrows. Modified from (Britannica, 2006).

2.2.2. Study Outline

Two to three weeks before the irradiation, baseline studies were performed, which comprised electrophysiological mapping of the heart, implantation of pacemakers and collection of blood samples. The implantation of a pacemaker ensured the survival of AVN targeted animals after a successful induction of a fibrotic scar. For the catheter-free irradiation procedure, the animals were transported to GSI with an adequately equipped truck. The animals were anaesthetized and blood samples were taken before the irradiation procedure. In addition, 12-channel electrocardiograms (ECGs) and blood samples were obtained at four follow-ups, which took place 4, 8, 12 and 24 weeks after irradiation. During the follow-ups after 4 and 8 weeks, regular ECGs were performed for the AVN pigs to check for AV blocks. In contrast, after 12 and 24 weeks final follow-ups were carried out.

2.2.3. Sample Collection and Processing

2.2.3.1. Histology

Three and six months after irradiation, animals were euthanized through intracardiac potassium injection. The heart, lungs, trachea, phrenic nerves and oesophagus were removed *en* block. Triphenyltetrazolium chloride (TTC) was administered to portray the ablation lesions by increasing the contrast between healthy myocardium and hypoxic regions as described in literature (Lie, Pairolero, Holley, & Titus, 1975). Discernible pathological findings were evaluated and noted. Afterwards, samples from different cardiac regions, like target, entrance channel and various outfield areas were obtained from all animals. The fixation of samples was accomplished with 4 % formalin solution at 4°C at least over night until 2 days. Afterwards, samples were rinsed with water and stored in 1x PBS for one or two weeks and then in 75 % ethanol at 4°C until further processing. Before the embedding of tissue samples in paraffin, a dehydration series was applied as depicted in Table 1.

Table 1: Dehydration and paraffinisation of tissue samples.

Solution	**Incubation Time**
95 % ethanol	over night
100 % ethanol I	90 minutes
100 % ethanol II	90 minutes
Xylol I	30 minutes
Xylol II	30 minutes
Paraffin I	120 minutes
Paraffin II	120 minutes
Paraffin III	120 minutes

After the paraffinisation, the tissue samples were aligned in block shaped moulds at room temperature until their hardened. The paraffin blocks were then attached to carriers to enable later cross sectioning and stored at room temperature. Sections of 4 or 7 µm were cut with a microtome. The tissue slides were placed on 30°C warm water to enable their extension and then absorbed to a glass slide. For optimal attachment, the slides were incubated at least one hour at 37°C on a heating plate. Afterwards, they could be stored at room temperature. For histological and antibody based staining methods, the tissue slides needed to be dewaxed and rehydrated. For this procedure, a series of descending alcohol concentrations was applied (Table 2).

Table 2: Rehydration of the paraffin sections for stainings.

Solution	**Incubation Time**
Xylol I	6 – 10 minutes
Xylol II	6 – 10 minutes
100 % ethanol I	3 – 5 minutes
100 % ethanol II	3 – 5 minutes
95 % ethanol	3 – 5 minutes
70 % ethanol	3 – 5 minutes
H_2O	3 – 5 minutes

After histological stainings, the tissue slides were dehydrated again in order to embed them with non-aqueous mounting medium and store them at room temperature. Unlike the rehydration process described in Table 2, a series of ascending alcohol concentrations was administered (Table 3).

Table 3: Dehydration of the paraffin sections after histological stainings.

Solution	**Incubation Time**
H_2O	5 minutes
95 % ethanol	5 minutes
100 % ethanol I	5 minutes
100 % ethanol II	5 minutes
Xylol I	3 minutes
Xylol II	3 minutes

2.2.3.2. Blood and Pericardial Fluid Samples

For the later analyses of soluble factors, blood samples were drawn at the day of irradiation and at every follow-up. For the retrieval of serum and plasma samples, blood samples were collected in specialized vacutainers and further processed according to the manufacturer´s instruction:

The plasma samples were centrifuged (300x g at 4°C) to partition the fluid from cellular components of the blood. For serum separation, samples were incubated for 30 minutes at room temperature and then also centrifuged. In addition, pericardial fluid (PF) was collected after euthanasia of the animals, which was only possible, if the pericardium was still intact. The complete separation of cellular contamination from the PF was ensured by centrifugation for 20 minutes (300x g at 4°C). After the sampling process, plasma, serum and PF were aliquoted and stored at -80°C for later ELISA measurements.

2.2.4. Histochemical Stainings

2.2.4.1. Haematoxylin and Eosin Staining

For first results on irradiation-induced effects in tissue samples, haematoxylin and eosin (H&E) staining was prepared. This staining technique is classically used for histopathology of tissue samples and was applied in this project to investigate the morphology of the tissue. Haematoxylin is an acidic staining agent, which is positively charged at a low pH value. Therefore, it stains negatively charged molecules in cells blue, for instance the DNA in the cell nucleus. Eosin though serves as counterstaining, because it is visible as a pink staining in the cytoplasm of cells and connective tissue fibres.

After the deparaffinisation and rehydration, which is shown in Table 2, the tissue sections were incubated for 8 to 10 minutes in Mayer´s haematoxylin solution. Afterwards, the slides were washed for 10 minutes with running tap water. This leads to a change from acidic to neutral pH milieu and therefore changes the colour of haematoxylin from blue to violet. After a washing step with deionized water, slides were incubated for 30 seconds in eosin solution. The slides were then rinsed with 70 % ethanol and then dehydrated with an ascending alcohol series as depicted in Table 3. The sections were mounted with non-aqueous mounting medium (EuKitt), dried flat and stored at room temperature.

2.2.4.2. Perls´ Prussian Blue Staining

The detection of siderophages was based on a classic detection method for iron, which is Prussian Blue. It was established by the German pathologist Max Perls and is widely used to identify the presence of iron in biopsy specimens, for instance in bone marrow or liver samples. The staining is sensitive enough to detect 2 ng of trivalent iron compounds in tissue sections, in particular in hemosiderin (Ponka, 1999; Welsch & Mulisch, 2010). The chemical reaction is based on the oxidation of ferrous ferrocyanide salts in an acidic milieu. The trivalent iron reacts with potassium ferrocyanide ($K_4[Fe(CN)_6]$) leading to the formation of a blue dye. The counterstaining for this study was performed with nuclear fast red, which leads to a red colouring of the cell nuclei.

For the staining procedure, tissue slides were dewaxed and rehydrated as depicted in Table 2. The working solution for the Prussian Blue staining consisted of equal volumes of 5 % w/v potassium ferrocyanide and 5 % v/v hydrochloric acid. The slides were incubated in the working solution at 60°C in a chemical fume hood. The working solution was changed twice after 1.5 – 2 minutes. Afterwards, the slides were washed three times in deionized water for 5 minutes each. For the counterstaining, tissue sections were incubated with nuclear fast red for 3 minutes and then washed with running tap water for 5 minutes. The slides were then dehydrated with an ascending alcohol series as shown in Table 3, mounted with non-aqueous mounting medium, dried flat and stored at room temperature.

2.2.4.3. Verhoeff-van Gieson Staining

The visualization of the different layers of blood vessels was realized with the Verhoeff-van Gieson staining method, which was adapted from the laboratory of Rob Coppes. The working solution consists of 5 % w/v alcoholic haematoxylin, which is oxidised by ferric chloride and iodine to haematin and acts as a black mordant staining of tissue. A diluted ferric chloride solution is used for the differentiation of this staining, because it dissolves the mordant. The elastic fibres are more affine to the haematin and are therefore stained more intense than the rest of the tissue. The only exception is cell nuclei, which are also stained darker. The counterstaining is achieved with van Gieson solution, which results in a red staining of collagen fibres, while the rest of the tissue has a brown-yellowish colour. Taken together, the tunica adventitia is stained in red-violet. In contrast, the tunica media has a greyish appearance due to the dark cell nuclei of the smooth muscle cells and is surrounded by an inner and outer elastic membrane in black. Consequently, this staining can be used to depict vessels and their remodelling.

The tissue sections were deparaffinised and rehydrated as presented in Table 2. The counterstaining of particularly cell nuclei with Ehrlich´s haematoxylin solution was applied for 3 minutes, which was followed by washing with running tap water for 8 minutes and then 2 minutes with deionized water. The elastic membranes were stained with the Verhoeff˝s working solution for 20 minutes and then rinsed with deionized water with 3 changes. The staining was differentiated with 2 % w/v ferric chloride for 30 seconds. If the working solution was used multiple times a day, the incubation time was adapted to 30 to 35 minutes for the second and 45 to 60 minutes for the third execution. The differentiation time was then limited to 5 seconds. The differentiation was stopped with several changes of tap water and verified microscopically. The slides were then washed with deionized water and counter-stained with van Gieson´s solution for 5 minutes. After rinsing in deionized water, the tissue slides were dehydrated (Table 3), mounted with non-aqueous mounting medium, dried flat and stored at room temperature. As collagen and elastic fibres are also abundant in scar and connective tissue, this staining only allowed for identification of microvasculature in the myocardium.

2.2.4.4. Haematoxylin Basic Fuchsin Picric Acid Staining

A non-enzymatic histochemical technique for the detection of early stages of myocardial and skeletal muscular ischemia was first described by Lie et al. This method can be used to identify ischemia before morphological alterations appeared (Bi et al., 2013; Lie, Holley, Kampa, & Titus, 1971; Scherer & Masi, 1975). The authors hypothesized that the affinity for the haematoxylin basic fuchsin picric acid (HBFP) staining was caused by an unstable protein or protein-phospholipid complex, because deamination prevented positive staining (Lie et al., 1971). Therefore Scherer and Masi demonstrated that the tissue sections needed to be cut within 2 days before staining to prevent false-positive signals (Scherer & Masi, 1975).

Based on the findings of Scherer and Masi, tissue sections were freshly cut before the staining and then deparaffinised and rehydrated as visualized in Table 2. The counterstaining was done with Ehrlich´s haematoxylin solution and only optional, because it caused a reddish background, which could be mistaken as positive signal. If applied, tissue slides were stained for 3 minutes and washed for 8 minutes with running tap water and another 2 minutes with deionized water. The tissue slides were then incubated with 0.1 % w/v basic fuchsin for 3 minutes and rinsed with deionized water and absolute acetone, each for 10 seconds. The staining was differentiated with 0.1 % picric acid in absolute acetone for 3 to 15 seconds. Afterwards, the sections were rinsed in absolute acetone again for 10 seconds, which was cleared directly afterwards twice in xylol for 3 minutes and mounted with non-aqueous mounting medium. Slides were stored at room temperature.

2.2.5. Antibody Staining

The expression and localisation of certain marker proteins in tissue was studied with specific antibodies. Before the staining procedure, the tissue slides were dewaxed and rehydrated as illustrated in Table 2. They were then equilibrated in citric buffer for 15 minutes and heated four times in a microwave at 800 Watt for 5 minutes. This procedure was applied to unmask the antigens, which may have become inaccessible due to the paraffinisation procedure. After the slides had cooled, they were washed three times with PBS for 5 minutes. The slides were outlined with a bold pen and covered with 0.3 % hydrogen peroxide for 30 minutes, which results in inactivation of endogenous peroxidases and therefore prevents false-positive signals later. After washing the slides for 5 minutes with PBS three times, a blocking solution (1.35 % goat serum and 0.1 % tween in PBS) was applied for 30 minutes to disguise non-specific antibody binding sites. The primary antibody was also diluted in the blocking solution as shown in Table 4 and its incubation was performed over night at 4°C.

Table 4: Primary antibodies for immunohistochemical stainings in tissue sections.

Antibody	Host	Specificity	Dilution
Active caspase 3	Rabbit	Human, mouse	1:50
Active caspase 3	Rabbit	Human, mouse	1:100
CD31	Rabbit	Mouse, human, pig	1:100
CD34	Rabbit	Mouse, rat, human	1:2500
Complement factor 9	Rabbit	Human	1:200
HIF-1α	Mouse	Mouse, human, pig	1:200
S100a	Rabbit	Mouse, rat, pig	1:100
S100b	Rabbit	Mouse, rat, pig	1:5000
vWF	Rabbit	Human, mouse, rat	1:200

After the incubation with the primary antibody the slides were washed three times with PBS for 5 minutes. The respective biotinylated secondary antibody was also diluted in blocking solution as shown in Table 5. The slides were then covered with the solution of the secondary antibody and incubated for 2 hours at room temperature

Table 5: Secondary antibodies for immunohistochemical stainings in tissue sections.

Antibody	Host	Dilution
biotinylated anti-rabbit IgG	Goat	1:100
biotinylated anti-mouse IgG	Horse	1:100

Afterwards, the slides were washed again three times for 10 minutes with PBS. In the meantime, the ABC-reagent was prepared according to the manufacturer´s instructions: To allow the avidin to complex with the biotinylated horseradish peroxidase (HRP), it was incubated at room temperature for 30 minutes. After the washing step, the ABC-reagent was incubated for 30 minutes with the slides. After three additional washing steps, the detection was performed with diaminobenzidine (DAB) in accordance with the manufacturer´s instructions. After stopping of the detection with deionized water, a counterstaining with Mayer´s hematoxylin solution for 8 minutes was achieved. The slides were then washed for 10 minutes with running tap water to induce a change of the pH-value. The slides were rinsed in deionized water, dehydrated (Table 3) and mounted with non-aqueous mounting medium.

2.2.6. Quantitative Analyses of Histological Changes

The detection of histological changes was carried out on paraffin sections of 4 or 7 µm. They were cut and stained with histological stainings and examined by light microscopy. Inhomogeneous distribution of several effects, like scar formation, were already detected macroscopically. Therefore, one to two sections of sample were analysed in at least two different locations to grasp occurrence of these effects in different zones of the areas of interest. For distinction of myocardium and scar tissue and scoring of inflammation, haemorrhage and siderophages, the total section was scanned. For the measurement of diameter of microvessels, ten to fifteen pictures per section were analysed depending on the inhomogeneous distribution of microvessels.

2.2.6.1. Scoring of Myocardium and Scar Tissue

Remodelling of the myocardium to scar tissue comprises several changes of the histological alterations. These alterations included enlargement or shrinkage of cardiomyocytes after irradiation as it is depicted in Figure 12. These two phenotypic changes were observed particularly in target areas. As the shrinkage of cardiomyocytes appeared in parallel to increased deposition of ECM proteins, which are associated with fibrosis, only this change was used as an indicator of fibrosis in this study.

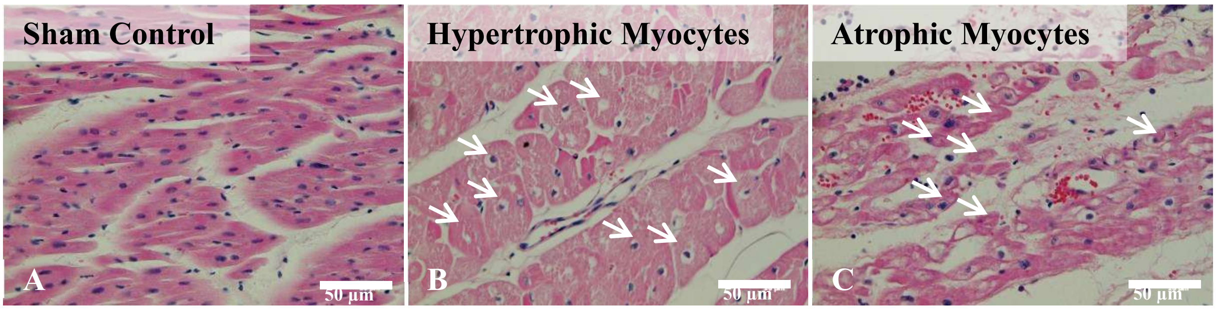

Figure 12: Irradiation-induced changes of cardiomyocytes in target areas, which are exemplarily shown after 40 Gy irradiation of the LV target in comparison to the sham control. Healthy cardiomyocytes (A) are shown in comparison to their hypertrophy (B) and atrophy (C). Sections were stained with H&E.

Cardiac remodelling after carbon ion irradiation also exhibited other changes, which are linked to fibrosis (Figure 13). In addition to the aforementioned shrinkage of cardiomyocytes in Figure 12, coagulative necrosis, which can be detected as lighter stained tissue without nuclei and cross-striation, and myocytolysis, the vacuolization of cardiomyocytes (Figure 13B and C) were detected particularly in target areas. The occurrences of these three phenotypic changes are linked to early fibrosis. In parallel to these early changes, increased deposition of ECM components (Figure 13E and F) were also observed in target areas. They are associated with later stages of fibrosis and cannot be distinguished from cardiac connective tissue, i.e. peri- and epimysium. To summarize, the appearance of coagulative necrosis, myocytolysis and shrinkage of cardiomyocytes as well as connective tissue were referred to as scar tissue.

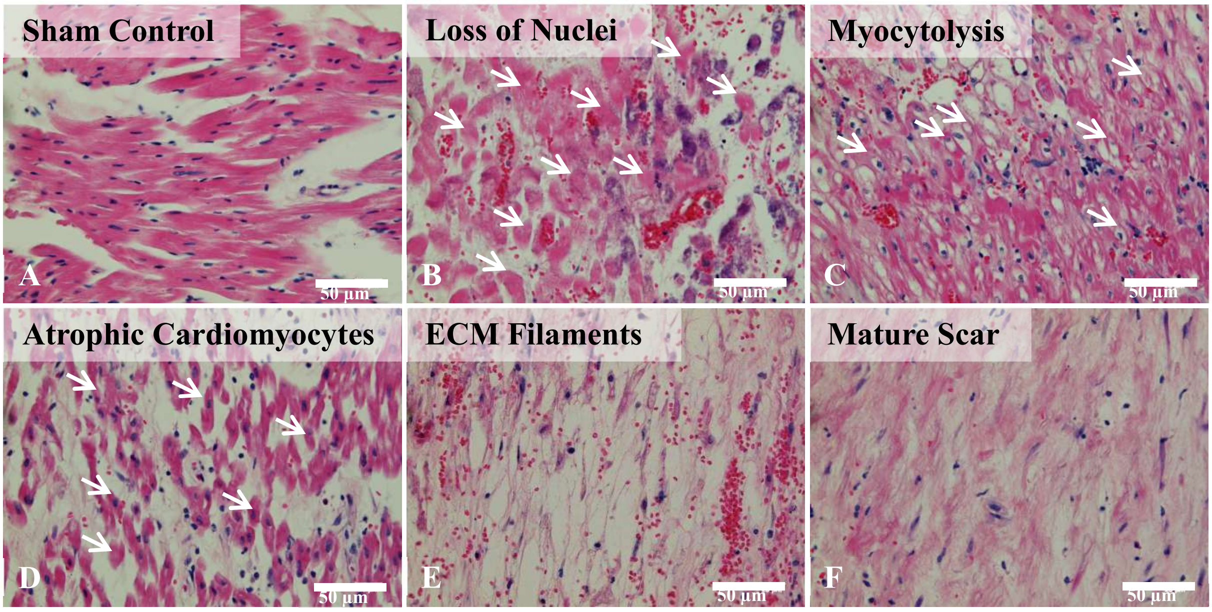

Figure 13: Fibrotic changes of the myocardium after carbon ion irradiation, which are exemplarily depicted after 40 Gy irradiation of the LV in comparison to the sham control. After high dosed carbon ion irradiation of the targets, healthy myocardium (A) underwent several alterations. The loss of nuclei, which were indicative of coagulative necrosis, (B) and myocytolysis (vacuoles in myocyte cytoplasm), which are linked to apoptosis or autophagy, (C) of cardiomyocytes represented early changes. They were followed by shrinkage of cardiomyocytes (D) and their replacement with connective tissue, here shown as matrix of ECM filaments (E) and its repopulation with cells (F). Sections were stained with H&E.

2.2.6.2. Scoring of Inflammation

Macroscopic investigations of particularly target areas indicated ongoing inflammatory processes. After the application of Perls´ Prussian Blue Stain for enhanced contrast, microscopic analyses revealed infiltration of immune cells. These were assessed with a scoring system per visual field, which was established in the presented thesis. The absence of immune cells was recorded as score 0, which means that only the pale pink nuclei of the resident tissue cells were present. The higher scores represent an increasing amount of infiltrated immune cells with intensive pink up to the highest amount, which was score 3, as shown in Figure 14.

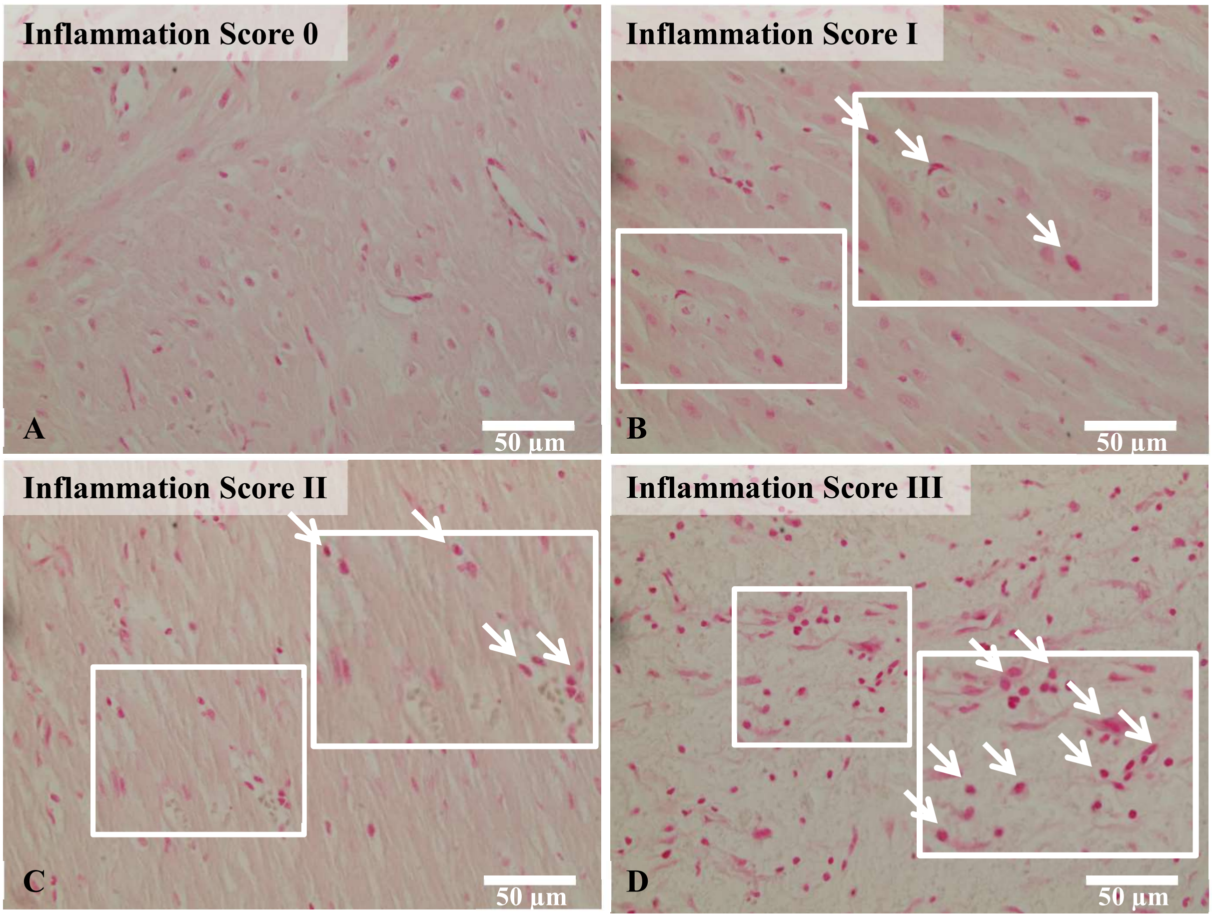

Figure 14: Scoring of inflammation after carbon ion irradiation. The arrows, inserts, and white frames serve the exemplification of infiltrating immune cells. The increasing number of infiltrating immune cells was connected to a scoring of inflammation per visual field. The analysis was performed after Perls´ Prussian Blue Staining.

2.2.6.3. Scoring of Haemorrhage

Similarly to inflammation, haemorrhage was observed during macroscopic investigations of target areas. Perls´ Prussian Blue Staining was used to enhance the contrast of tissue for microscopic analyses. Haemorrhage was evaluated with a scoring system per visual field. In accordance to the assessment of infiltration of immune cells, the absence of erythrocytes out of blood vessels per visual field was documented as score 0. The consequent scores increased with enhanced occurrence of haemorrhage. The highest score (3) was adapted to the most elevated level of haemorrhage observed in the tissue. The scoring of haemorrhage is depicted in Figure 15.

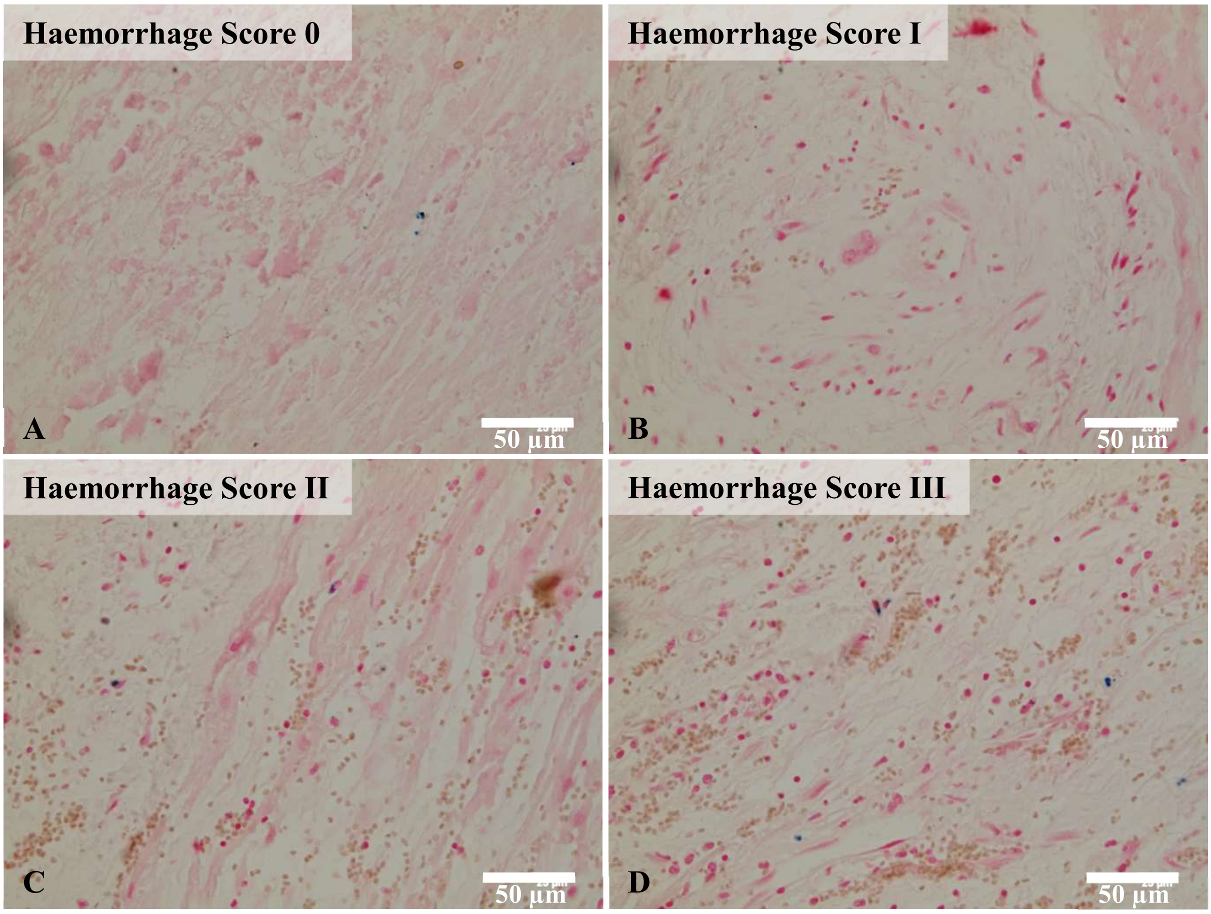

Figure 15: Scoring of haemorrhage after carbon ion irradiation. The increasing amount of erythrocytes outside of blood vessels was connected to a scoring of haemorrhage per visual field. The analysis was performed after Perls´ Prussian Blue Staining.

In addition to the scoring of haemorrhage, the area per visual field, where haemorrhage occurred, was also measured as shown in Figure 16. This further information was added, because haemorrhage was often limited to a discrete area of the visual field in contrast to inflammation. The amount of haemorrhage was assessed as the quotient of the scoring and the percentage area covered by erythrocytes.

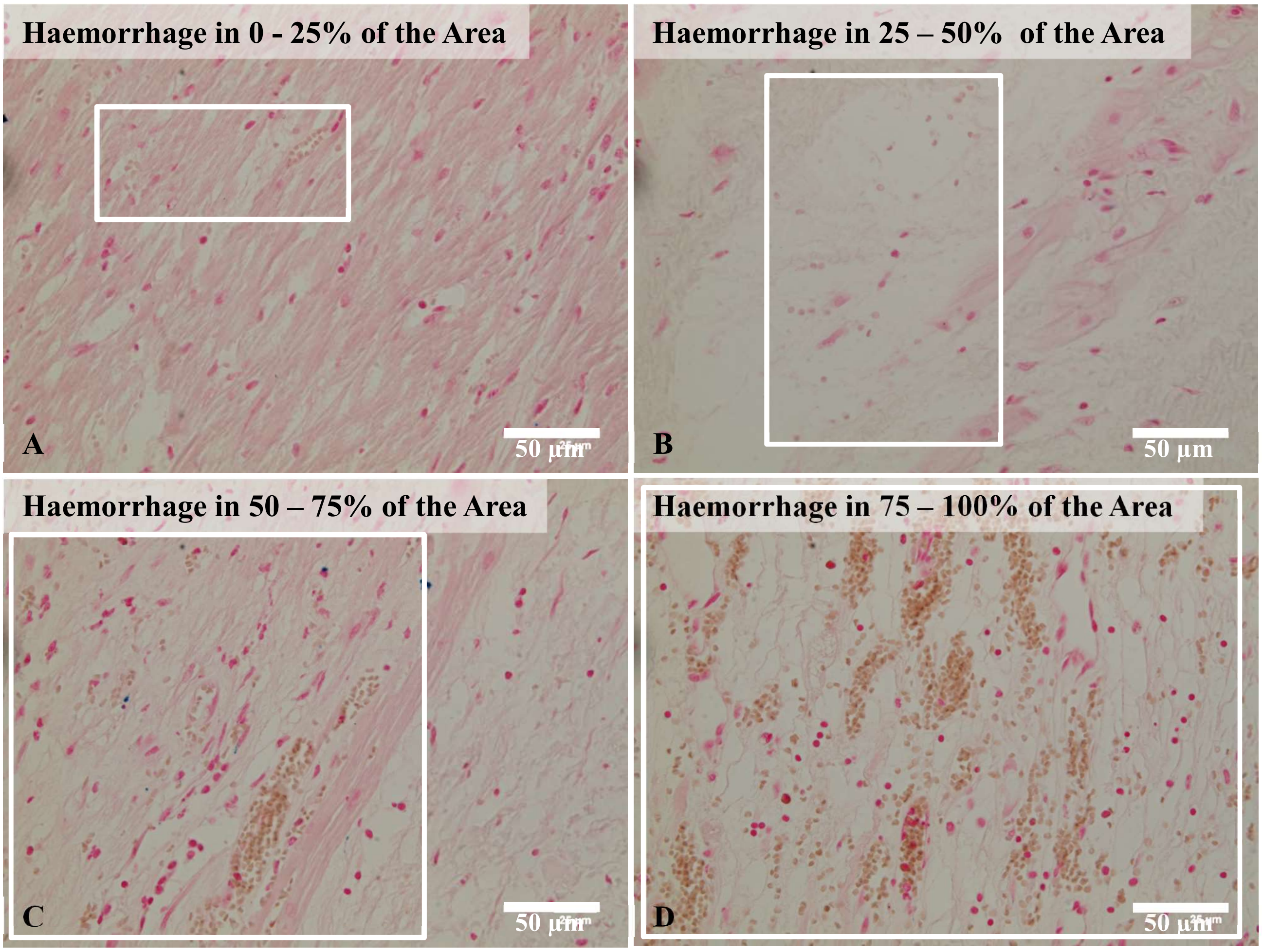

Figure 16: Area covered with haemorrhage after carbon ion irradiation. The area per visual field, which was covered with erythrocytes outside of blood vessels, was described as quarters of the visual field, which increased accordingly. The white frames indicate the area covered with haemorrhage in the particular visual field. The analysis was performed after Perls´ Prussian Blue Staining.

2.2.6.4. Scoring of Siderophages

After the incidence of haemorrhage, immune cells, in particular macrophages, clear the tissue from blood components by phagocytosis. In the course of this process, the phagocytosing cells accumulate iron from the haemoglobin of erythrocytes. Under normal physiological conditions, the iron is stored with ferritin and can be recycled again. If the amount of phagocytised iron however exceeds the capacity of iron storage in a cell, autophagy is induced. During this process, a complex, which is insoluble in water, is formed out of ferritin and other proteins to store the iron. This complex is contained in specialized vesicles and called hemosiderin (Ponka, 1999). Cells containing hemosiderin are called siderophages. They are most prominently known as “heart failure cells” in lung tissue. In this case, high pulmonary blood pressure pushes erythrocytes through the vascular wall in alveoli, which can then also be detected in the sputum of patients (Lederer et al., 2014). However, siderophages are not specific for heart failure. For instance, they were also used for the detection of hematoma in the uterus and microbleeds in the brain (Fisher, French, Ji, & Kim, 2010; Shirota et al., 2013). Although they can be detected by H&E staining, Perls´ Prussian Blue Stain is more sensitive and allows for more defined distinction of the amount of iron in siderophages.

According to the amount of iron in siderophages, their intensity of blue staining increases after application of Perls´ Prussian Blue Stain. Similar to the quantification of haemorrhage and inflammation, the amount of siderophages per visual field was determined with a scoring system. No detection of staining corresponded to a score of 0. The more area of siderophages was covered by blue colouring, the scoring increasing from 1 to 4. The highest score resembled the biggest area covered with hemosiderin as shown in Figure 17.

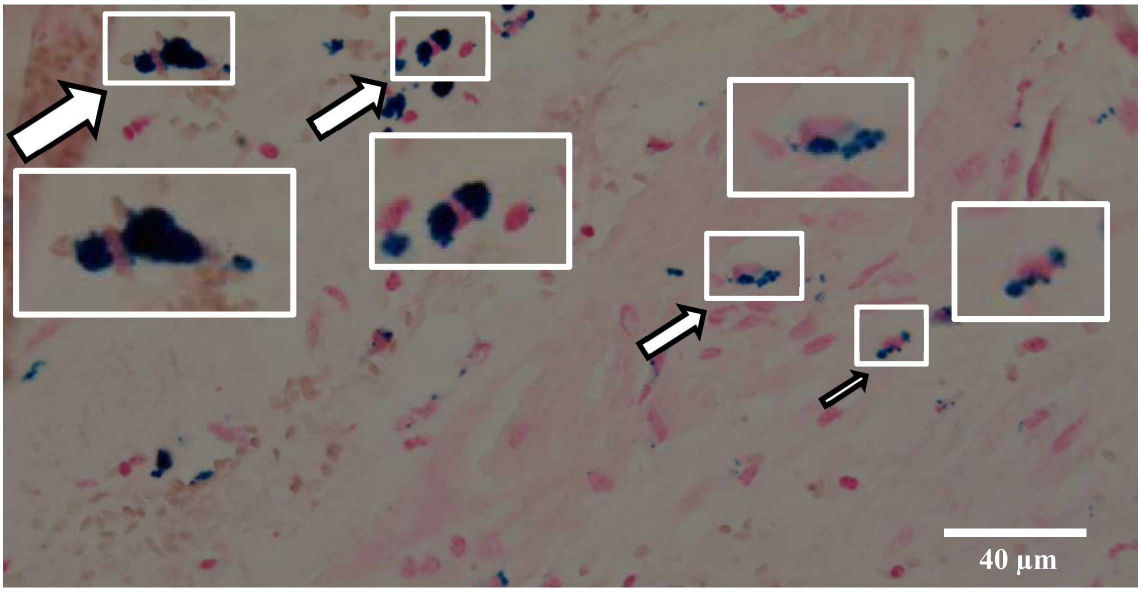

Figure 17: Scoring of siderophages after carbon ion irradiation. The inserts and white frames serve the exemplification of siderophages. The increasing blue stained area in the cytoplasm of siderophages was linked to a scoring of haemorrhage per visual field, which is here indicated with increased thickness of arrows. The analysis was performed after Perls´ Prussian Blue Staining.

In adaption of Lederer et al., the scoring of siderophages was assessed as Golde score (Lederer et al., 2014). This Golde score was applied, because it takes the scoring of siderophages as increased amount of hemosiderin and their number per visual field into account. This additional calculation is depicted in Table 6.

Table 6: Depiction of the Golde score calculation.

Iron content of siderophages	**Number of cells**	**Coefficient x number of cells**
Score 0	N_0	$0 \times N_0$
Score I	N_I	$1 \times N_I$
Score II	N_{II}	$2 \times N_{II}$
Score III	N_{III}	$3 \times N_{III}$
Score IV	N_{IV}	$4 \times N_{IV}$
Total score (for all detected cells, N_{total})		Sum_{total}

2.2.6.5. Measurement of the Diameter of Microvessels

Vascular damage is hypothesized to be the initial event of fibrotic processes (Adams et al., 2003; Schultz-Hector & Trott, 2007; Seemann et al., 2012). In particular microvessels were identified as the radiosensitive target (Fajardo & Stewart, 1971; Hopewell et al., 1986), which is especially crucial, because they mediate nutrient and oxygen exchange within the tissue. Therefore, the diameter of microvessels, which also comprise capillaries, was measured. For this approach, tissue sections were stained with Verhoeff-van Gieson staining, which highlights the basement membrane, i.e. the one of the endothelium. The staining was only reliable in the myocardium; therefore, the analyses of the diameter of microvessels could not be applied to connective or scar tissue. An exemplary staining of myocardium is shown in Figure 18.

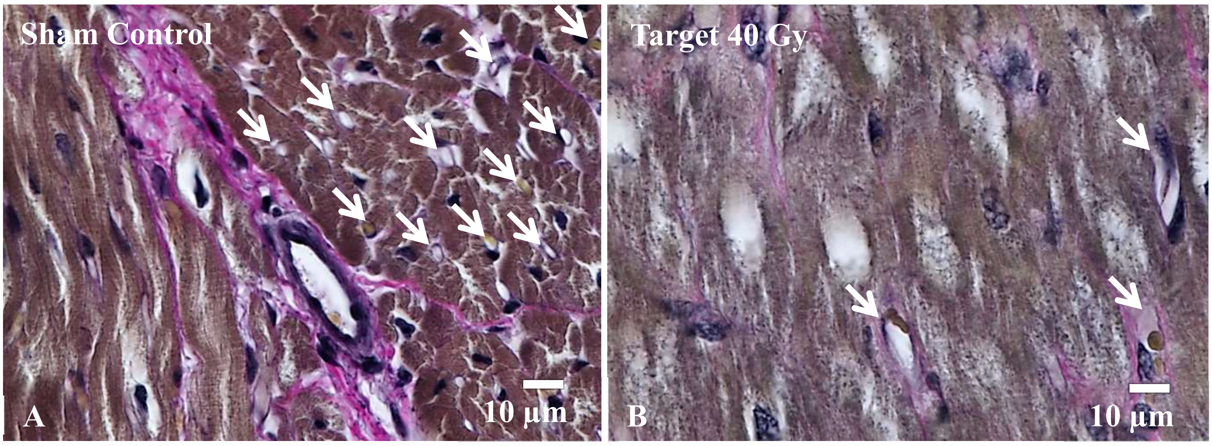

Figure 18: Microvessels in the LV of a sham control and after 40 Gy of carbon ion irradiation. The microvessels are indicated with arrows. A large number of small vessels was detected in sham control tissue (A) compared to vessels with a bigger diameter in fewer number, which is exemplarily shown for LV target irradiation. Reprinted from (Erbeldinger et al., 2015).

A pilot study based on the data collected for the mean diameter of microvessels in control animals collection revealed that the mean diameter of microvessels in the LV without any treatment decreased until three months after irradiation and increased again until six months after irradiation (Figure 19A). These changes were based on the varying number of microvessels, because in the beginning, only few small vessels with a diameter between 2 and 5 µm were measured. In accordance with the mean diameter of microvessels, the number of small vessels with the respective diameters increased until three months and was not detected until six months after irradiation anymore (Figure 19B). Therefore, the investigation of the effect of irradiation required a comparison with the respective time control. Interestingly, a similar mean diameter of small vessels in the LV outfield and target regions of the sham control after three months were detected, although the outfield region comprised a higher number of microvessels. This result led to the investigation of the diameter of microvessels in different cardiac substructures (Figure 19B).

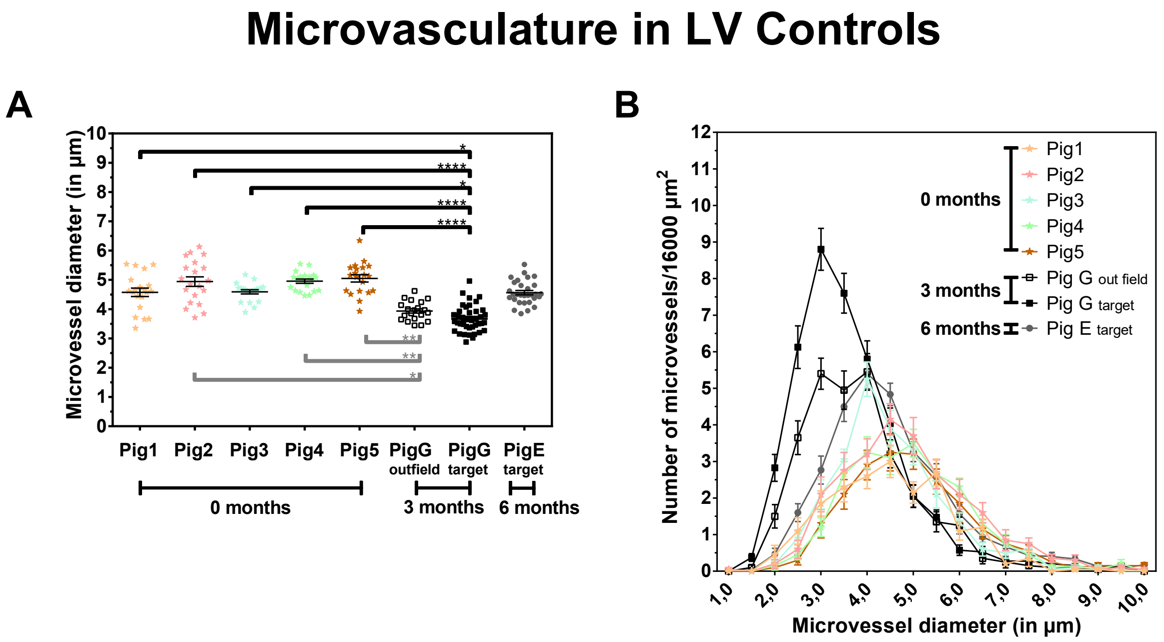

Figure 19: Diameter of microvessels over time in the LV. Mean diameter (A) and the corresponding frequency distribution (B) were measured in myocardium tissue of different control animals. Mean diameter, mean and SEM are shown. * = p-value ≤ 0.05, ** = p-value ≤ 0.01, *** = p-value ≤ 0.001, **** = p-value ≤ 0.0001. Significance is tested with Kruskal Wallis Test for non-parametric distributions and for multiple comparisons Dunn´s correction is applied.

As shown in Figure 20, the mean diameter and number of small vessels is specific for the cardiac substructure. The mean diameter of small vessels in the sham control pig for six months after irradiation was especially narrow in the AVN and IVS, which are comparably located in the middle of the heart (Figure 20A). The distribution of occurrences reveals that this diversion can be attributed to a higher number of vessels with a very small diameter (Figure 20B). In addition, fewer microvessels were detected in the left than the right side of the heart, although the mean diameter of microvessels was similar for these cardiac substructures. Taken together, these findings demonstrate that the number of microvessels is not identical for every substructure and requires detailed analyses.

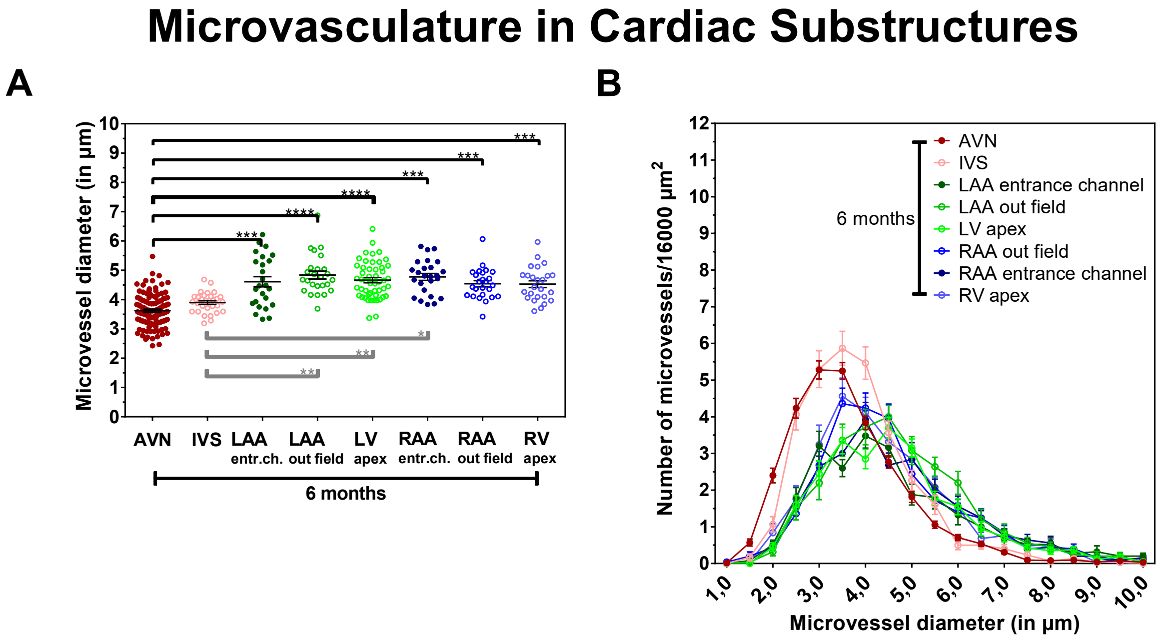

Figure 20: Diameter of microvessels in different cardiac areas. Mean diameter (A) and the corresponding frequency distribution (B) were measured in myocardium tissue of the control animal, which was sacrificed six months after irradiation. Mean diameter, mean and SEM are shown. * = p-value ≤ 0.05, ** = p-value ≤ 0.01, *** = p-value ≤ 0.001, **** = p-value ≤ 0.0001. Significance is tested with Kruskal Wallis Test for non-parametric distributions and for multiple comparisons Dunn´s correction is applied.

In addition to the distribution of the diameter of small vessels, which changed over time and were specific for the different cardiac substructures, the distribution of the diameter of microvessels varied in particular after irradiation. This is exemplarily depicted for the LV target three months after irradiation Figure 21. Hence, the number of pictures analysed per sample were adjusted to the respective areas of the heart to cover the distribution of the diameter of small vessels (Table 7).

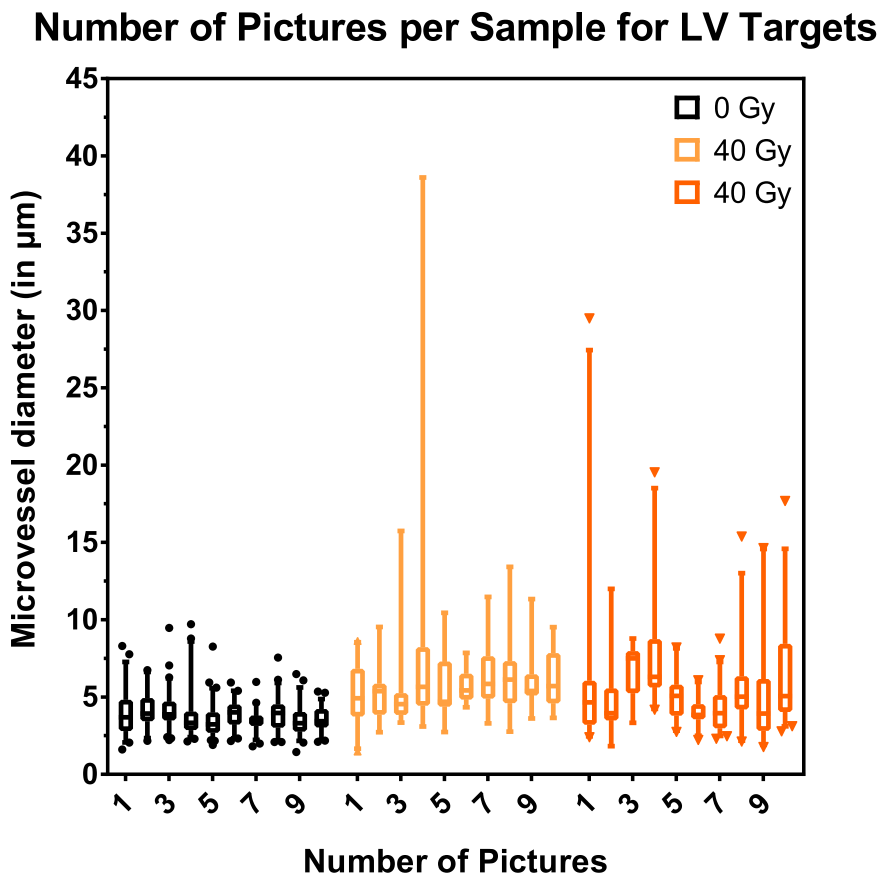

Figure 21: Diameter of microvessels in LV targets, representatively shown after 3 months. The different diameters of small vessel per visual field were measured in the myocardium tissue for the LV of a sham control and two irradiated pigs. The data are depicted as a box plot wit median, first and third quantile and the 2.5 and 97.5 percentile for every visual field.

Table 7: Number of analysed pictures per sample for diameter of microvessels.

Target Areas		**Entrance Channel Regions and other Structures**	
LV	**AVN**	**LV, RV, and apices**	**LAA, RAA, and IVS**
2x10 pictures	2x 15 pictures	2x10 pictures	1x10 and 1x15 pictures

2.2.7. ELISA

The release of soluble factors, like cytokines, is important for cell signalling, because they serve the communication between cells, which are not directly adjoined. For the detection of soluble factors, an enzyme-linked immunosorbent assay (ELISA) was performed. The assays were provided as kits from different manufacturers and were carried out according to their instructions. The principle of this assay is based on an antigen-antibody-interaction, which can be quantified by a colorimetric reaction at the end. For this procedure, a so-called capture antibody is immobilized on the bottom of a 96 well-plate, which binds specifically to the molecule, which is investigated in this particular test and hereinafter referred to as analyte. In the next step, a biotinylated antibody, the detection antibody, binds to another domain of the analyte. The biotin forms a stable complex with streptavidin, which is coupled to HRP. The substrate for HRP is tetramethylbenzidine (TMB), whose oxidation leads to a blue colouring. This reaction is proportional to the original concentration of the analyte. The reaction is stopped with sulphuric acid, which causes a colour change from blue to yellow. The optical density (OD) can then be measured with a microplate reader set to 450 nm with a wavelength correction at 570 nm to compensate for imperfections of the plate. A standard series of known analyte concentrations and blanks for every assay allows for the calculation of the investigated analyte concentration for every sample.

2.2.8. Statistical Analyses

In this section, the statistical methods applied for the data analyses are introduced. The scoring of haemorrhage, inflammation and siderophages as well as the diameters of small vessels per visual field were given together with the arithmetic mean of all collected data points (hereinafter referred to as mean) and the standard error of the mean (SEM). The analysis of the distribution of small vessels was carried out categorizing the diameter of small vessels per visual field. In the following step, the mean and SEM were calculated for every category and shown as distribution of occurrences.

Significant increases in the tissue responses in comparison to the sham control or between different animals were assessed with the Kruskal-Wallis statistics and *post hoc* analysis were performed using Dunn´s test. This one-way analysis of variance method was applied, because it is the standard test for multiple comparisons of metric and ordinally scaled data of equal or different sample sizes (Rudolf & Kuhlisch, 2008). As the data in the presented thesis were both metric (diameter of microvessels, soluble markers) and ordinally scaled (haemorrhage, inflammation and siderophages), this testing method was applied. The analyses and representation of the investigated effects were performed with the GraphPad Prism version 7.02 for Windows, GraphPad Software, La Jolla California USA, www.graphpad.com.

3. Results

Effects of high dosed carbon ion irradiation were investigated in a porcine model three and six months after irradiation of small volumes (1 – 1.5 cm^3). The experiments of this thesis have been carried out in the frame of a project to investigate the application of carbon ion irradiation for cardiac ablation. Therefore, the left ventricle (LV) and atrioventricular node (AVN), as clinically relevant targets of cardiac ablation, were irradiated. The aim of this thesis was to investigate vascular changes as initial events of fibrogenic mechanisms after carbon ion irradiation of cardiac substructures as a putative cause for ablation. As shown in Figure 22, irradiation–induced histological changes included haemorrhage, inflammation and scar formation, which were among the effects that were further investigated in this thesis.

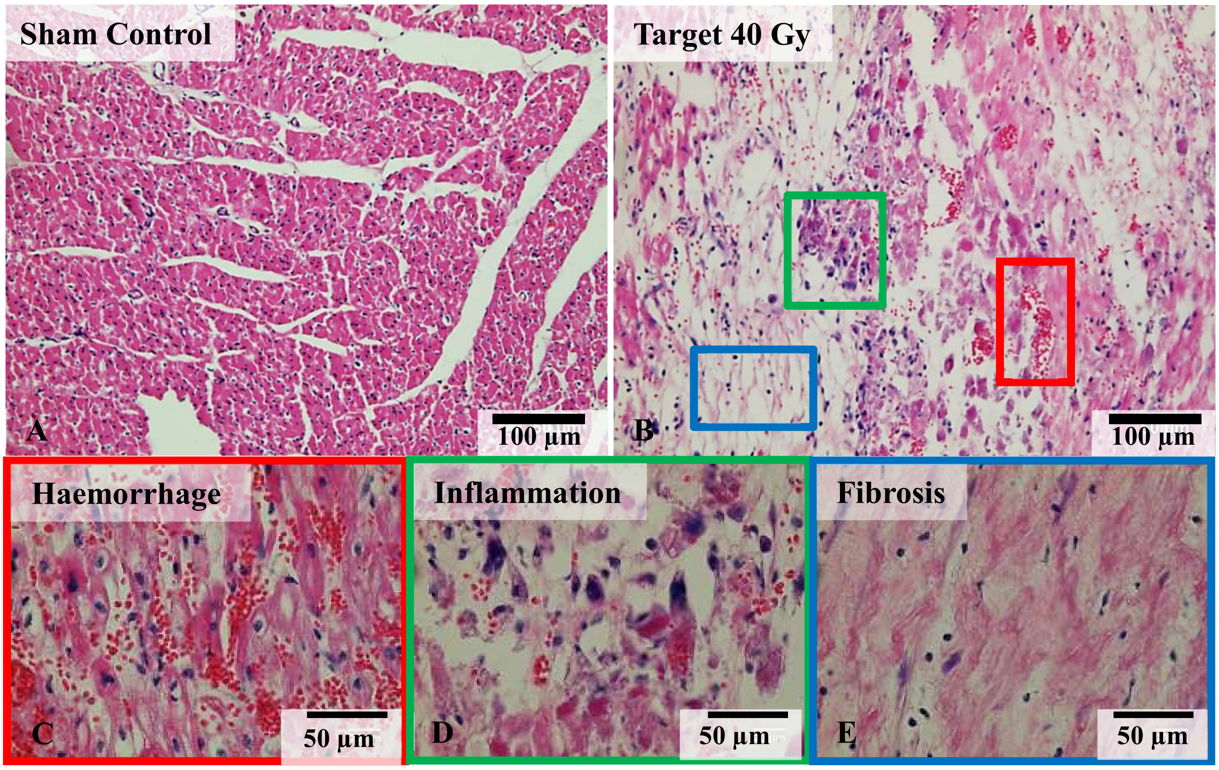

Figure 22: Representative images of irradiation–induced damage. Healthy cardiac tissue was observed in the sham control (A), whereas after irradiation, scar formation manifested (B) comprising haemorrhage (C), inflammation (D) and fibrosis (E) (H&E staining).

In addition to haemorrhage and inflammation, other types of vascular damage were studied. Examples on the changes of medium sized vessels are depicted in Figure 23, but were only rarely observed. Furthermore, the exchange of nutrients and oxygen of myocardium is provided by the microvasculature. Therefore, the effect of irradiation on microvessels was investigated, because their damage is directly linked to tissue damage like hypoxia and cell death, which are crucial events for further tissue remodelling.

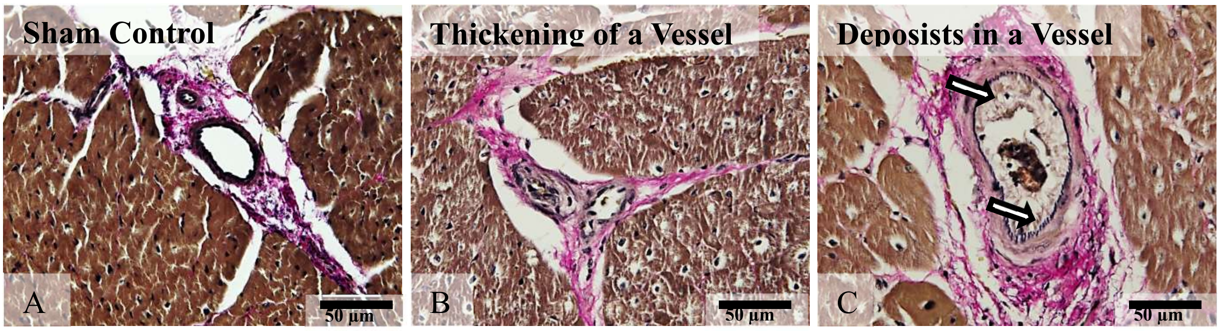

Figure 23: Representative images of vascular remodelling, which was only observed sporadically in target areas. A) Sham controls display normal cardiac tissue and vasculature. Irradiation of target areas (40 – 55 Gy) leads to occlusion via B) thickening of vascular wall and C) deposits on vascular wall as indicated by arrows (Verhoeff van Gieson staining).

3.1. Tissue Remodelling in the Target Areas

Although ionizing irradiation is described to cause fibrosis after fractionated low doses of X-irradiation to big volumes of the heart years after treatment (Gyenes, Rutqvist, Liedberg, & Fornander, 1998; Schultz-Hector & Trott, 2007), the time frame for effects after high dosed carbon ion irradiation of a small volume is not known. Therefore, time- and dose-dependent effects of high dosed carbon ion irradiation were investigated in this thesis.

Time-dependent effects of carbon ion irradiation were investigated at two time points (three and six months) in the LV of three pigs (Pig R, S and T, 40 Gy) and compared to two sham controls (Pig G and E) (Table 8).

Table 8: Treatment and macroscopic outcome of LV pigs in target areas three and six months after irradiation.

Time after irradiation	Sham control	LV Target (40 Gy)	LV Target (40 Gy)
Three months	Pig G	Pig R (weak fibrotic response)	Pig S (strong fibrotic response)
Six months	Pig E		Pig T (strong fibrotic response)

After three months, three pigs were sacrificed, Pig G, Pig R and Pig S. The two remaining pigs, Pig E and Pig T, were sacrificed after six months. Macroscopic analysis revealed only minor scar formation in the LV of Pig R. In contrast, Pig S and T both displayed major scar formation in targeted areas, which was more advanced after six months. Morphological examinations were performed in order to correlate cellular changes with lesion formation and functionality of the tissue. An overview of the investigated effects in the target region is given in Table 9, whereas the complete results of more detailed analyses are presented in the following chapters. Inflammation and haemorrhage indicated persistent tissue remodelling, while microvascular density and scar formation point to the progression of fibrosis. Compared to the control animal sacrificed at three months, the irradiated animals showed pronounced effects in terms of haemorrhage, inflammation, decrease of small vessels and scar formation. These tissue responses were more pronounced in Pig S than Pig R. In contrast, six months after irradiation the target region of Pig T displayed less haemorrhage and inflammation than Pig S after three months, but still elevated compared to the respective control at six months. Comparison of scar formation in the target regions of Pig S and T three and six months after irradiation points to progression of fibrosis over time.

Table 9: Effects in the whole LV target tissue in percentage three and six months after carbon ion irradiation.

Treatment and Time after Irradiation	**Haemorrhage**	**Inflammation**	**Small vessels (2-5 µm) in myocardium**	**Scar Tissue**
Pig G **(sham control, 3 months)**	0.6 %	1.6 %	100 %	0.4 %
Pig R **(LV 40 Gy, 3 months)**	4 %	17 %	33 %	1 %
Pig S **(LV 40 Gy, 3 months)**	51 %	89 %	30 %	53 %
Pig E **(sham control, 6 months)**	5.5 %	17 %	100 %	3.1 %
Pig T **(LV 40 Gy, 6 months)**	22 %	66 %	36 %	78 %

While haemorrhage and inflammation manifested between three and six months, loss of microvasculature and scar formation were established prior to the investigation and represent ongoing irradiation induced effects at three and six months (Table 9).

After obtaining the results, that fibrosis was not induced in the whole target area in LV targets after three months, AVN targeted pigs were sacrificed six months after irradiation. The tissue of six pigs was analysed for dose-dependent effects of carbon ions irradiation to cardiac substructures. As shown in Table 10, the doses for ablation of AVN were 25 Gy in two pigs (Pig H and Pig O), 40 Gy in one pig (Pig I) and 55 Gy in another two pigs (Pig F and Pig N). In addition, one pig served as sham control (Pig E).

Table 10: Treatment and electrophysiological outcome of AVN pigs in target areas.

Time after irradiation	**Sham control**	**AVN Target (25 Gy)**		**AVN Target (40 Gy)**	**AVN Target (55 Gy)**	
Six months	Pig E	Pig H	Pig O	Pig I (transient AV block)	Pig F (persistent AV block)	Pig N

After six months, two out of three high dose irradiated pigs had AV block (Pig I and F). Histological changes in the target area six months after irradiation with high dosed carbon ion irradiation are displayed in Table 11. Because carbon ion irradiation of 55 Gy caused an AV block in only one out of two pigs (Lehmann et al., 2016), underlying histological changes were investigated. The complete results of more complex analyses are presented in the following chapters.

Table 11: Effects in the whole AVN target tissue in percentage six months after carbon ion irradiation.

Treatment and Time after Irradiation	**Haemorrhage**	**Inflammation**	**Small vessels (2-5 µm) in myocardium**	**Scar Tissue**
Pig E **(sham control, 6 months)**	12 %	24 %	100 %	20 %
Pig H **(25 Gy, 6 months)**	10 %	36 %	47 %	34 %
Pig O **(25 Gy, 6 months)**	21 %	38 %	37 %	44 %
Pig I **(40 Gy, 6 months)**	29 %	47 %	38 %	39 %
Pig F **(55 Gy, 6 months)**	80 %	70 %	28 %	59 %
Pig N **(55 Gy, 6 months)**	32 %	63 %	26 %	58 %

As shown in Table 11, pronounced effects in terms of haemorrhage and inflammation were observed with increasing dose compared to the control animal. In addition, scar formation and a decreased number of small vessels were also detected in the target areas of irradiated animals. These results indicate no clear connection between histological changes, in particular scar formation, and the development of an AV block in only two out of three high dose irradiated animals.

3.1.1. Haemorrhage in Target Areas

One prevalent effect after irradiation was haemorrhage. The disruption of blood vessels is an established consequence of irradiation and can induce further tissue remodelling (Chrastina, Pokreisz, & Schnitzer, 2014). The quantification of haemorrhage was performed for the whole target area tissue and also separately conducted for myocardium and scar tissue of the target areas.

As displayed in Figure 24 for the whole LV target tissue, no significant difference in haemorrhage compared to the control animal was observed in the target area of Pig R (weak fibrotic response). In target areas with strong fibrotic response (Pig S and T), a substantial amount of haemorrhage was observed for both time points (Figure 24A). Similar observations were made in the myocardium and scar tissue (Appendix, Figure 48B and C). Comparing animals sacrificed at three and six months indicated diminished haemorrhage over time.

In the whole tissue of AVN targets (Figure 24B), haemorrhage was more pronounced than in the corresponding target area of the respective control (Pig E) and it increased with dose. The highest amount of haemorrhage was detected in the AVN target with persistent AV block after 55 Gy (Pig F). Equivalent patterns as in the whole tissue were found in myocardium and scar tissue, although higher levels of haemorrhage (in relation to the myocardium) were measured in scar tissue (Appendix, Figure 48E and F).

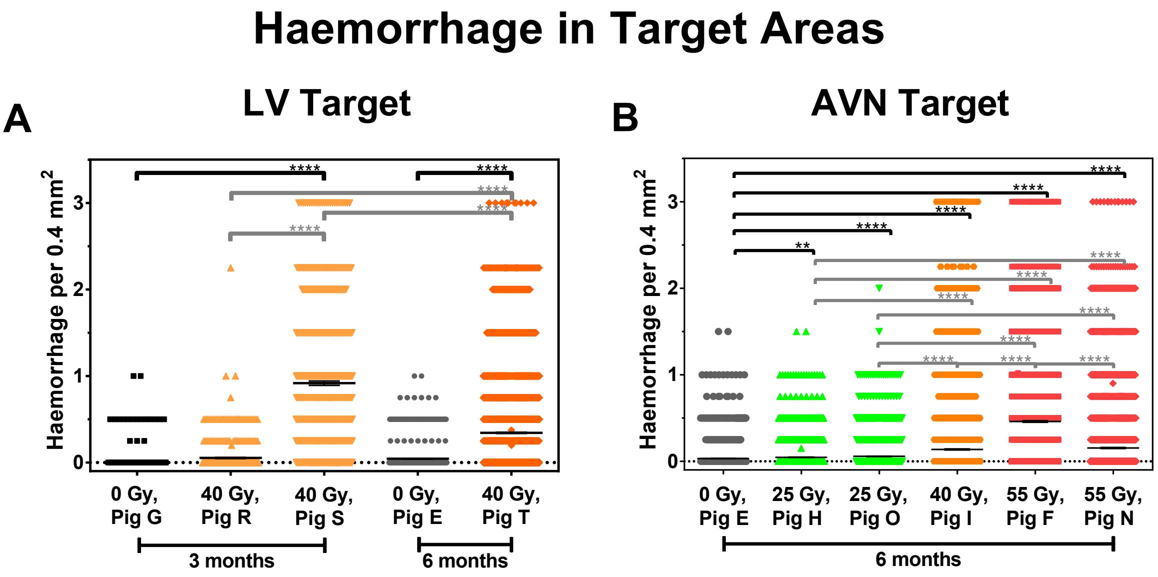

Figure 24: Haemorrhage in target areas was most pronounced three and six months after 40 Gy of carbon ion irradiation in animals with strong fibrotic response and increased with dose. Whole target areas were analysed either after LV (A) or AVN (B) targeted irradiation. Scoring per visual field, mean and SEM are shown. * = p-value ≤ 0.05, ** = p-value ≤ 0.01, *** = p-value ≤ 0.001, **** = p-value ≤ 0.0001. Significance was tested with one-way Kruskal Wallis statistic and Dunn´s post hoc test.

3.1.2. Inflammation in Target Areas

Another prevailing observation after irradiation was the infiltration of immune cells. When tissue is damaged by various stimuli, for instance ionizing irradiation, a protective response of the immune system is triggered (Reece & Urry, 2011), which in turn can contribute to substantial organ damage (Adams et al., 2003; Ricardo, Van Goor, & Eddy, 2008; Schultz-Hector & Trott, 2007). In this thesis, inflammation was scored by the application of histological methods. Scoring of inflammation included the differentiation between the whole target area and its myocardium and scar tissue.

The appearance of inflammation over time and the dependence on dose is shown in Figure 25. In LV targets, elevated levels of inflammation were detected in the whole target area compared to corresponding LV areas of control animals. In target areas with strong fibrotic response (Pig S and T), the highest amount of inflammation was observed, which diminished between three and six months (Figure 25A). Inflammation was most marked in scar tissue (Appendix, Figure 52B and C). As shown in Figure 25B for the whole tissue, AVN targets exhibited lower levels of inflammation than LV targets after irradiation with the same dose (40 Gy) at the same time point (six months after irradiation). The quantification of inflammation revealed that the number of infiltrating immune cells increased with dose. The findings on inflammation in the whole tissue of LV and AVN target areas were most reflected by scar tissue (Appendix, Figure 52E and F).

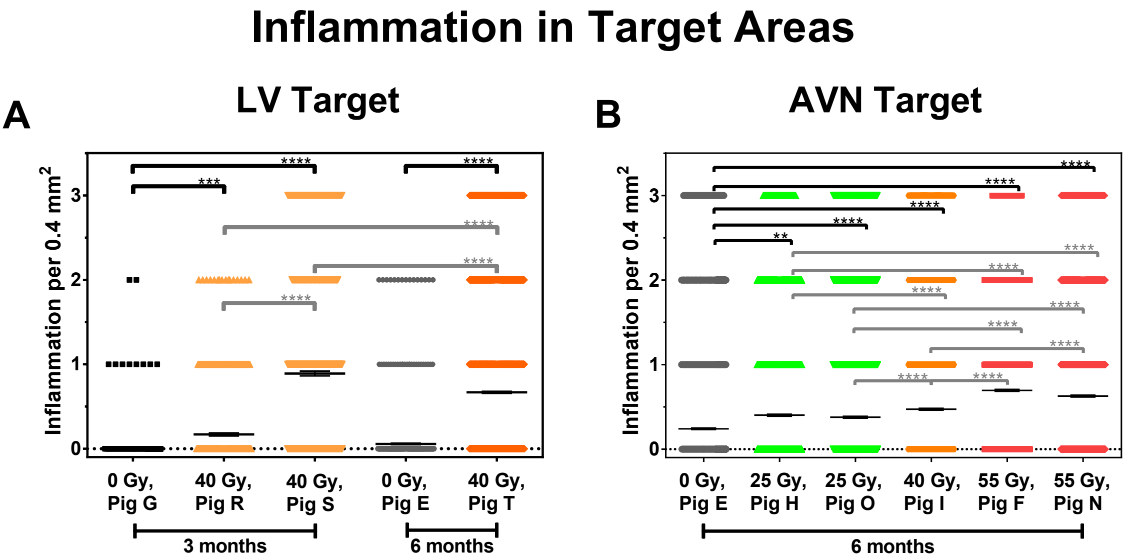

Figure 25: Inflammation in target areas was most pronounced in animals with strong fibrotic response and increased with dose. Whole target areas were analysed either after LV (A) or AVN (B) targeted irradiation. Scoring per visual field, mean and SEM are shown. * = p-value ≤ 0.05, ** = p-value ≤ 0.01, *** = p-value ≤ 0.001, **** = p-value ≤ 0.0001. Significance was tested with one-way Kruskal Wallis statistic and Dunn´s post hoc test.

3.1.3. Distribution of Microvascular Diameters in Target Areas

The exposure to high doses of ionizing radiation is a known cause for vascular remodelling. This holds especially true for the microvasculature, blood vessels with a diameter between 2 and 10 µm (Hopewell et al., 1986; Seemann et al., 2012). Furthermore, haemorrhage was a prevalent effect in this study. This motivated investigations on the reorganization of blood vessels. The dominantly occurring blood vessel type in cardiac tissue are capillaries (Schmidt & Lang, 2007; Taunk et al., 2015). Consequently, the diameter of microvessels was quantified in the myocardium.

In Figure 26, the distribution of the diameter of small vessels in myocardium of targets after carbon ion irradiation is displayed after different time points (LV target) and different doses (AVN target). The mean diameter of microvasculature increased after irradiation at both time points compared to the corresponding tissue of control animals. This increase was similar after the application of the same dose, independent of the time point (Figure 26A), but became more pronounced with an increasing dose (Figure 26C). As depicted by the distribution of occurrences, a decreased number of small vessels with a diameter between 2 and 5 µm was found (Figure 26B and D). As a consequence, this loss of small vessels led to an increased mean diameter.

As the main function of microvessels is the alimentation of tissue, their loss is usually associated with hypoxia (Prech et al., 2010; Uchida, Uchida, Maezawa, Maezawa, & Tabata, 2012). However, hypoxia could not be verified in this work (Figure 47 and Figure 46).

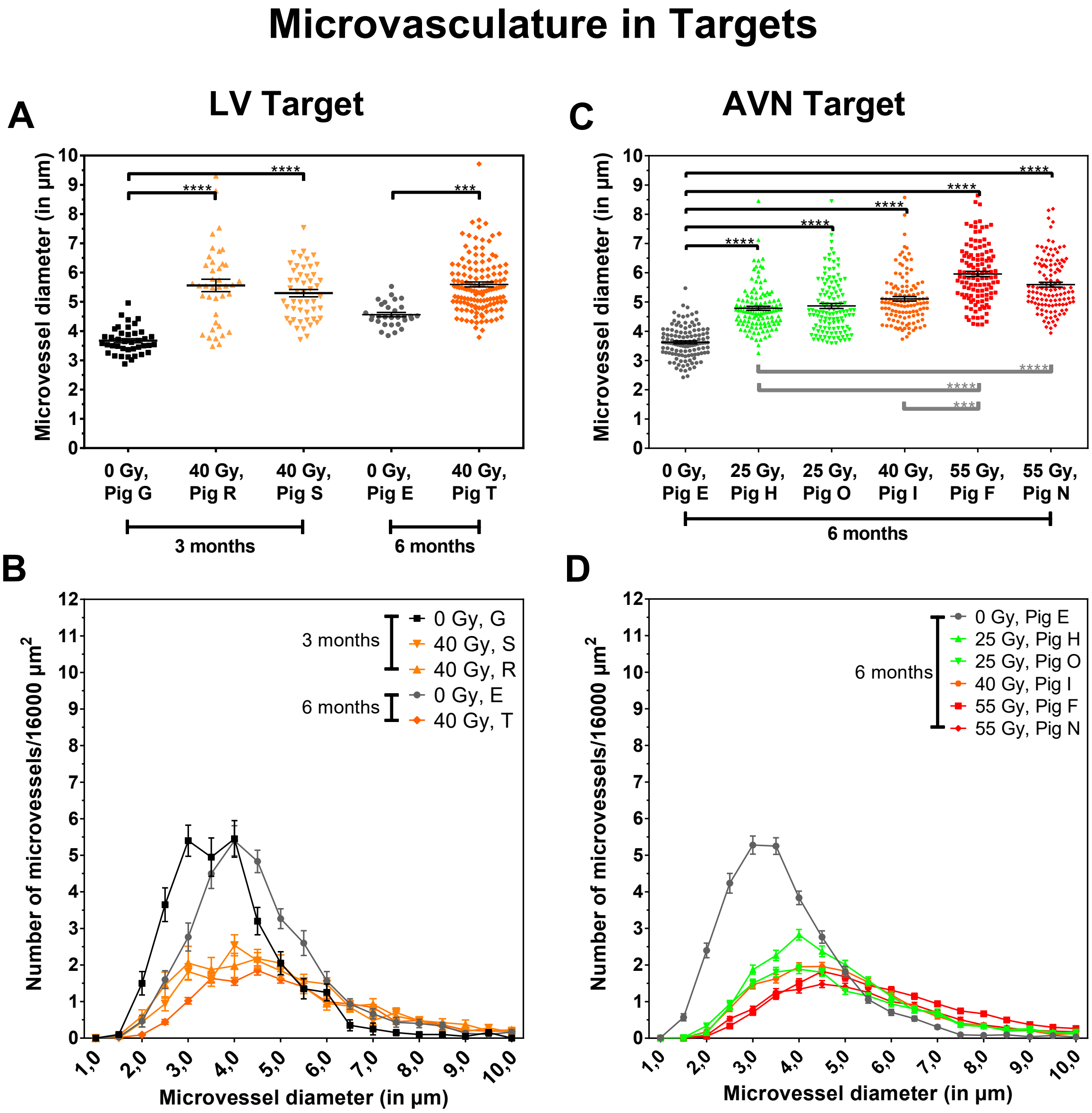

Figure 26: Dose-, but not time-dependent loss of small vessels in target areas. The mean diameter of microvessels after LV (A) or AVN (C) targeted irradiation and the corresponding distribution of occurrences (B and D) were measured in the myocardium. Mean diameter, mean and SEM are shown. * = p-value ≤ 0.05, ** = p-value ≤ 0.01, *** = p-value ≤ 0.001, **** = p-value ≤ 0.0001. Significance was tested with one-way Kruskal Wallis statistic and Dunn´s post hoc test.

3.1.4. Presence of Iron-Containing Macrophages in Target Areas

The disruption of blood vessels and subsequent haemorrhage and decreased number of microvessels after exposure to ionizing radiation is a well-known effect (Chrastina et al., 2014). Accordingly, haemorrhage and loss of microvessels were also observed in this study. During haemorrhage, blood cells, including erythrocytes, are deposited in tissue. Afterwards, the tissue is repaired by cells of the immune system, mostly macrophages. The accumulation of iron in macrophages leads to their conversion into so-called siderophages, which can be visualized by Perl´s staining. The quantification of siderophages allows the assessment of a Golde score (Lederer et al., 2014). Similar to haemorrhage and inflammation, this analysis was carried out in whole target area, which was further discriminated into myocardium and scar tissue.

In whole target areas, a larger number of siderophages were detected only in targets with strong fibrotic response (Pig S and T, Figure 27A). They were most frequently observed after six months and increased with dose (Figure 27B). Similar results were obtained in myocardium and scar tissue of both target areas, although in myocardium Golde score only manifested six months after irradiation (Appendix, Figure 56B, C, E, and F).

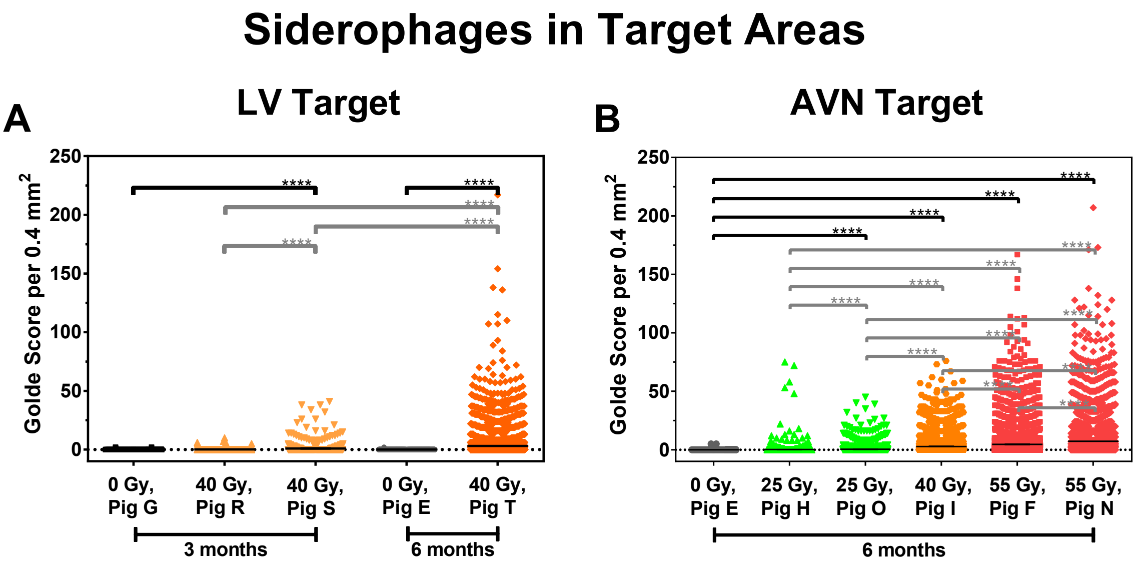

Figure 27: Increased formation of siderophages over time and with dose. Whole target areas were analysed either after LV (A) or AVN (B) targeted irradiation. Scoring per visual field, mean and SEM are shown. * = p-value ≤ 0.05, ** = p-value ≤ 0.01, *** = p-value ≤ 0.001, **** = p-value ≤ 0.0001. Significance was tested with one-way Kruskal Wallis statistic and Dunn´s post hoc test.

3.2. Tissue Remodelling in Entrance Channel and Non-Targeted Regions

The ablation of target areas was intended with high dosed carbon ion irradiation. In the course of this treatment, two horizontal pencil beams penetrated the heart tissue before they reached the target areas. This condition led to deposition of medium doses (7-17 Gy) in the entrance channel regions. Therefore, the following sections focused on the effects of medium doses (7-17 Gy).

In addition, the spreading of damage to surrounding tissue is a late effect of tissue remodelling after vascular damage (Adams et al., 2003; Baldi et al., 2002; Dusek et al., 1971; Heidenreich & Kapoor, 2009; Schultz-Hector & Trott, 2007; Taunk et al., 2015; Virag & Murry, 2003). This motivated the investigation of potential outfield effects. The beam fields for target irradiation and the respective entrance channel regions are depicted in Figure 28. For irradiation of the LV target, the pencil beams for irradiation of the LV target traversed the right ventricle (RV) and another part of the LV before they reached the target (Figure 28A). As shown in Figure 28B, the treatment of AVN target entailed the exposure of the right atrial appendage (RAA) and the left atrial appendage (LAA).

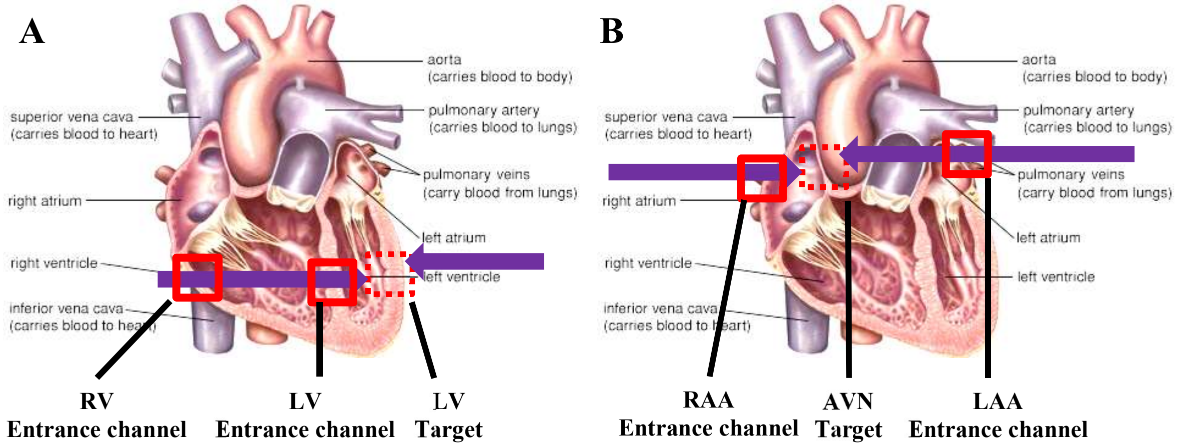

Figure 28: Depiction of the respective entrance channel during after LV (A) and the AVN (B) target irradiation. The harvested entrance channel regions are indicated with red boxes consisting of solid lines, whereas the red boxes consisting of dashed lines show the target areas. Modified after (Britannica, 2006).

The estimated maximum dose per entrance channel region is indicated in the respective figures. The interventricular septum (IVS), which separates both cardiac ventricles, was in near vicinity of the AVN targets and thus was potentially accidentally irradiated (A. Eichhorn and C. Graeff, GSI, personal communication). As the manifestation of damage in this area might contribute to an AV block, effects in the IVS were also investigated. The studies on irradiation-induced tissue responses presented in this chapter were carried out analogously to the target areas.

Exemplarily for the histological findings in the entrance channel areas after LV targeted irradiation, an overview is presented in Table 12 for the RV entrance channel. The complete results are depicted in the following chapters. Compared to the corresponding sham controls, the amount of haemorrhage and inflammation was only increased six months after irradiation (Pig T, 16 Gy), whereas the number of small vessels was only decreased in one animal three months after irradiation (Pig R, 16 Gy). Despite these occasional histological alterations, the amount of scar tissue was similar to the sham controls. In contrast, damage occurred more frequently in the LV entrance channel areas compared to the RV entrance channel regions after irradiation (Appendix, Table 15). In addition, the irradiation of LV entrance channel regions caused an increased amount of scar tissue. However, the extent of histological changes was less pronounced than in the target areas.

Table 12: Effects in the whole RV entrance channel areas in percentage three and six months after carbon ion irradiation.

Treatment and Time after Irradiation	**Haemorrhage**	**Inflammation**	**Small vessels (2-5 µm) in myocardium**	**Scar Tissue**
Pig G **(sham control, 3 months)**	6.2 %	26 %	100 %	9.5 %
Pig R **(LV 16 Gy, 3 months)**	6.6 %	33 %	62 %	9.9 %
Pig S **(LV 16 Gy, 3 months)**	1.1 %	12 %	93 %	4.1 %
Pig E **(sham control, 6 months)**	4.3 %	26 %	100 %	5.9 %
Pig T **(LV 16 Gy, 6 months)**	10.3 %	61 %	104 %	6.3 %

During AVN target irradiation, the IVS was also irradiated. As the applied doses to the IVS could not be further approximated, the doses in the following figures were labelled with “irr.#”. A gross inspection on histological changes indicated that at least 1 cm^3 IVS tissue adjacent to target areas was irradiated with high doses. As shown in Table 13, the irradiation of the IVS caused pronounced manifestations of haemorrhage, inflammation and scar formation in particular in the IVS of Pig F (persistent AV block). For both pigs with the highest target dose (AVN 55 Gy, Pig F and N), a fewer number of small vessels was detected in the IVS.

Table 13: Effects in the whole IVS tissue in percentage six months after carbon ion irradiation.

Treatment and Time after Irradiation	**Haemorrhage**	**Inflammation**	**Small vessels (2-5 µm) in myocardium**	**Scar Tissue**
Pig E **(sham control, 6 months)**	1.7 %	3 %	100 %	2.2 %
Pig H **(irr.#, 6 months)**	4.3 %	21 %	93 %	6.4 %
Pig O **(irr.#, 6 months)**	2.6 %	5 %	78 %	6.3 %
Pig I **(irr.#, 6 months)**	3.7 %	11 %	82 %	9 %
Pig F **(irr.#, 6 months)**	37 %	78 %	38 %	37.9 %
Pig N **(irr.#, 6 months)**	1.7 %	14 %	49 %	6.5 %

Comparably to LV target irradiation, an overview on the effects on the dextral entrance channel regions, the RAA, are exemplarily shown for both entrance channel sites of AVN target irradiation. More detailed results are shown in the following chapters. As presented in Table 14, the amount of inflammation, but not vascular damage (haemorrhage and number of microvessels), was increased after irradiation with medium doses compared to the sham control. Only in the RAA entrance channel region of one pig (Pig F), more scar tissue than in the sham control was detected. In the LAA entrance channel region (Appendix, Table 16), the level of vascular damage and inflammation were comparable to the sham control and an increased amount of scar formation was also only detected in one pig (Pig N). However, the tissue responses in the LAA and RAA entrance channel regions were less marked than in the target areas.

Table 14: Effects in the whole RAA entrance channel areas in percentage six months after carbon ion irradiation.

Treatment and Time after Irradiation	**Haemorrhage**	**Inflammation**	**Small vessels (2-5 µm) in myocardium**	**Scar Tissue**
Pig E **(sham control, 6 months)**	6.1 %	37 %	100 %	27 %
Pig H **(7 Gy, 6 months)**	3 %	87 %	77 %	26 %
Pig O **(9 Gy, 6 months)**	5.6 %	37 %	83 %	19 %
Pig I **(14 Gy, 6 months)**	1.7 %	85 %	103 %	16 %
Pig F **(17 Gy, 6 months)**	4.5 %	77 %	89 %	43 %
Pig N **(17 Gy, 6 months)**	2.8 %	46 %	88 %	25 %

Investigations in several outfield regions (Appendix, Table 17, Table 18, Table 19, and Table 20) demonstrated that tissue responses did not appear in unirradiated areas. Moreover, these measurements showed that the effects in target and entrance channel areas were not only more pronounced than in sham controls, but also compared to outfield regions within the same heart.

3.2.1. Haemorrhage in Entrance Channel and Non-Targeted Regions

In Figure 29, the appearance of haemorrhage in the IVS is shown. In the whole tissue, only the IVS of Pig F (persistent AV block) showed more pronounced haemorrhage than the corresponding areas of the control and the other irradiated animals, exposed to either the same dose (Pig N) or a lower dose (Pigs H, O and I). Comparable patterns were observed in myocardium and scar tissue (Appendix, Figure 49 B and C).

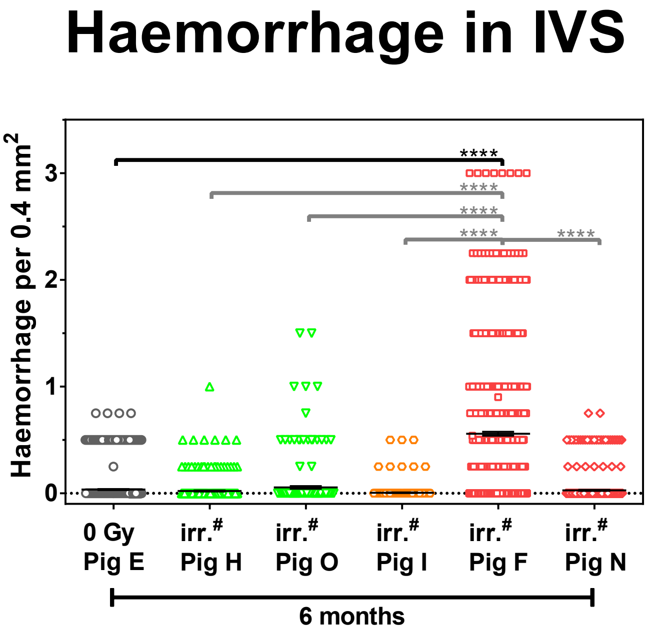

Figure 29: Increased amounts of haemorrhage were only detected in IVS of the one animal with persistent AV block (Pig F). The whole area of IVS was analysed six months after AVN targeted irradiation. The doses to the IVS were not determined = irr.$^{\#}$. Scoring per visual field, mean and SEM are shown. * = p-value $\leq$ 0.05, ** = p-value $\leq$ 0.01, *** = p-value $\leq$ 0.001, **** = p-value $\leq$ 0.0001. Significance was tested with one-way Kruskal Wallis statistic and Dunn´s post hoc test.

In Figure 30, the results for the scoring of haemorrhage in the whole sinistral entrance channel are depicted. No damage was observed. Investigations differentiating myocardium and scar tissue revealed a slightly increased manifestation of haemorrhage only in the myocardium (Appendix, Figure 50B, C, E, and F).

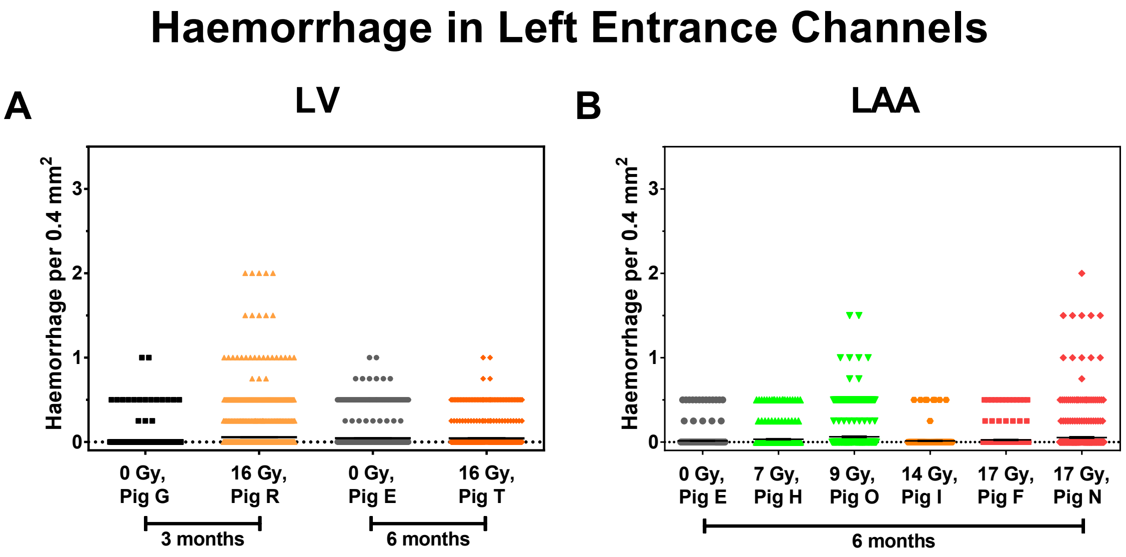

Figure 30: Haemorrhage was not frequently observed in sinistral entrance channel regions. The whole area of sinistral entrance channel regions was analysed after LV (A) or AVN (B) targeted irradiation. Scoring per visual field, mean and SEM are shown. * = p-value ≤ 0.05, ** = p-value ≤ 0.01, *** = p-value ≤ 0.001, **** = p-value ≤ 0.0001. Significance was tested with one-way Kruskal Wallis statistic and Dunn´s post hoc test.

Haemorrhage in the whole dextral entrance channel regions is visualized in Figure 31. In contrast to the sinistral entrance channel regions (Figure 30), a low amount of haemorrhage was detected. These observations were only obtained after LV and not AVN irradiation. This manifestation was mainly based on the tissue response in the myocardium (Appendix, Figure 51B, C, E, and F).

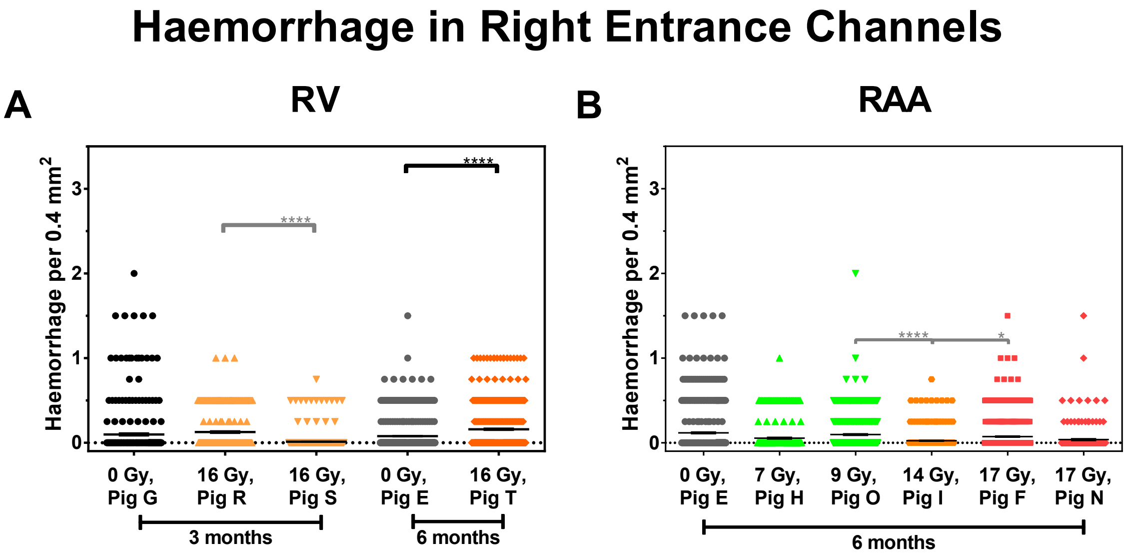

Figure 31: Pronounced levels of haemorrhage compared to the sham control were only observed in the RV six months after irradiation. The whole area of dextral entrance channel regions was analysed after LV (A) or AVN (B) targeted irradiation. Scoring per visual field, mean and SEM are shown. * = p-value ≤ 0.05, ** = p-value ≤ 0.01, *** = p-value ≤ 0.001, **** = p-value ≤ 0.0001. Significance was tested with one-way Kruskal Wallis statistic and Dunn´s post hoc test.

3.2.2. Inflammation in Entrance Channel and Non-Targeted Regions

The infiltration of immune cells into IVS tissue after AVN irradiation is shown in Figure 32. In the whole tissue, IVS of two animals (Pig H and F) exhibited larger amounts of inflammation than the corresponding area of the respective control and the other animals. These results were particularly mirrored by the myocardium (Appendix, Figure 53Figure 57B and C).

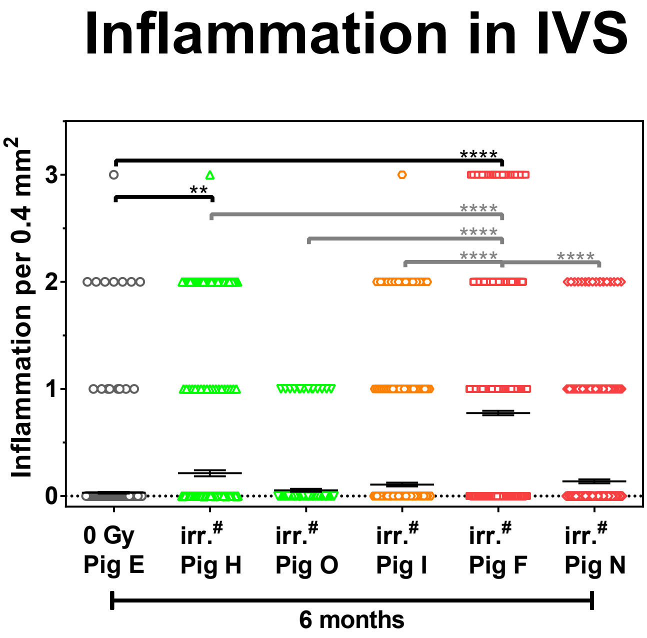

Figure 32: Increased infiltration of immune cells was detected in IVS after irradiation. The whole area of IVS was analysed six months after AVN targeted irradiation. The doses to the IVS were not determined = irr.#. Scoring per visual field, mean and SEM are shown. * = p-value ≤ 0.05, ** = p-value ≤ 0.01, *** = p-value ≤ 0.001, **** = p-value ≤ 0.0001. Significance was tested with one-way Kruskal Wallis statistic and Dunn´s post hoc test.

In Figure 33, inflammation in the whole tissue of left entrance channel regions is shown after LV and AVN irradiation. In the areas of the LV entrance channel slightly enhanced inflammation was detected compared to the corresponding areas of the respective control animal. These changes were more pronounced at six months than at three months (Figure 33A). As depicted in Figure 33B, the LAA entrance channel of only one animal exhibited a small amount of immune cells (Pig H, AVN 25 Gy) compared to the respective tissue of the control animal (Pig E) after AVN irradiation. The comparison of myocardium and scar tissue of left entrance channel regions shows that the described tissue responses were most pronounced in the myocardium (Appendix, Figure 54B, C, E, and F).

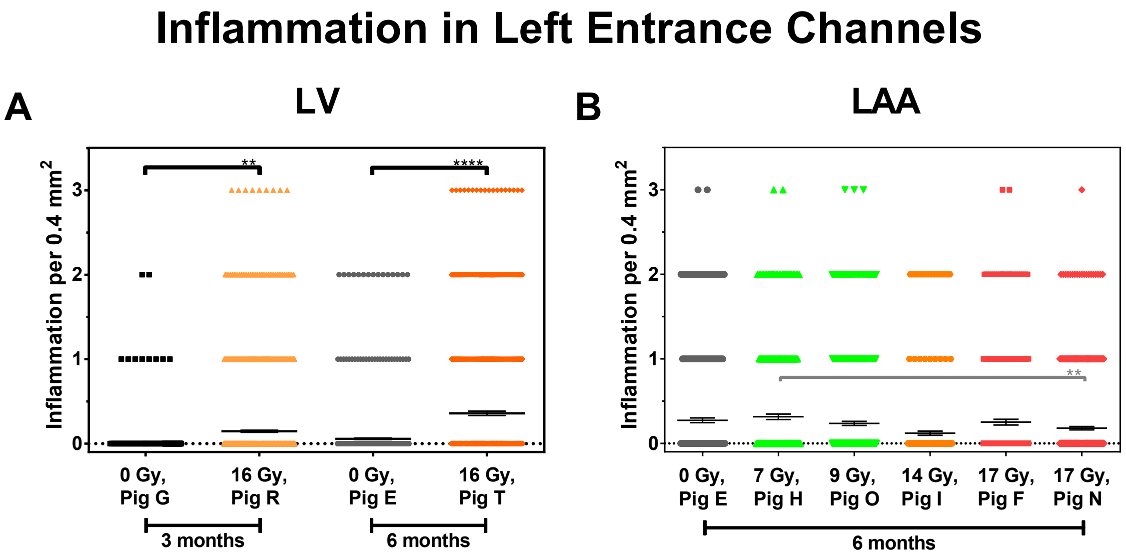

Figure 33: Increased levels of inflammation were only detected in sinistral entrance channel regions after LV-targeted irradiation. The whole area of sinistral entrance channel regions was analysed after LV (A) or AVN (B) targeted irradiation. Scoring per visual field, mean and SEM are shown. * = p-value ≤ 0.05, ** = p-value ≤ 0.01, *** = p-value ≤ 0.001, **** = p-value ≤ 0.0001. Significance was tested with one-way Kruskal Wallis statistic and Dunn´s post hoc test.

The detection of infiltrating immune cells into right entrance channel regions is illustrated in Figure 34. In the whole tissue of the RV after LV irradiation, more immune cells were observed than in any other entrance channel and unirradiated tissue at both time points (Figure 34A). After AVN irradiation, pronounced levels of inflammation were obtained in the whole tissue of RAA entrance channel regions after irradiation with different doses (7 Gy in Pig H, 14 Gy in Pig I and 17 Gy in Pig F) compared to the control animal (Pig E, Figure 34B). These effects were more marked in myocardium than scar tissue (Appendix, Figure 55B, C, E, and F).

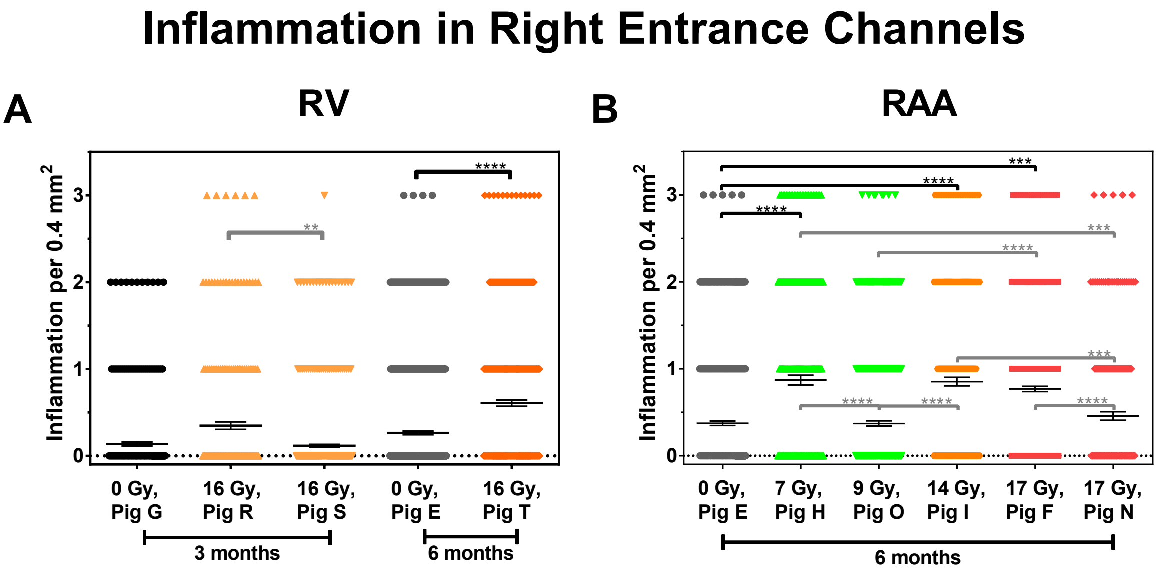

Figure 34: Inflammation was most pronounced six months after irradiation in dextral entrance channel regions. The whole area of dextral entrance channel regions was analysed after LV (A) or AVN (B) targeted irradiation. Scoring per visual field, mean and SEM are shown. * = p-value ≤ 0.05, ** = p-value ≤ 0.01, *** = p-value ≤ 0.001, **** = p-value ≤ 0.0001. Significance was tested with one-way Kruskal Wallis statistic and Dunn´s post hoc test.

3.2.3. Distribution of Microvascular Diameters in Entrance Channel and Non-Targeted Regions

In Figure 35, the mean diameter of small vessels and the corresponding distribution of occurrences in the myocardium of the IVS of AVN targeted hearts are displayed. As shown in Figure 35A, the mean diameter of microvasculature only increased after AVN irradiation with the highest dose (Pig F and N, AVN 55 Gy). In parallel, a decreased number of small vessels with a diameter between 2 and 5 µm was observed in the distribution of occurrences (Figure 35B). This incident was interpreted as a loss of small vessels and caused the increased mean diameter.

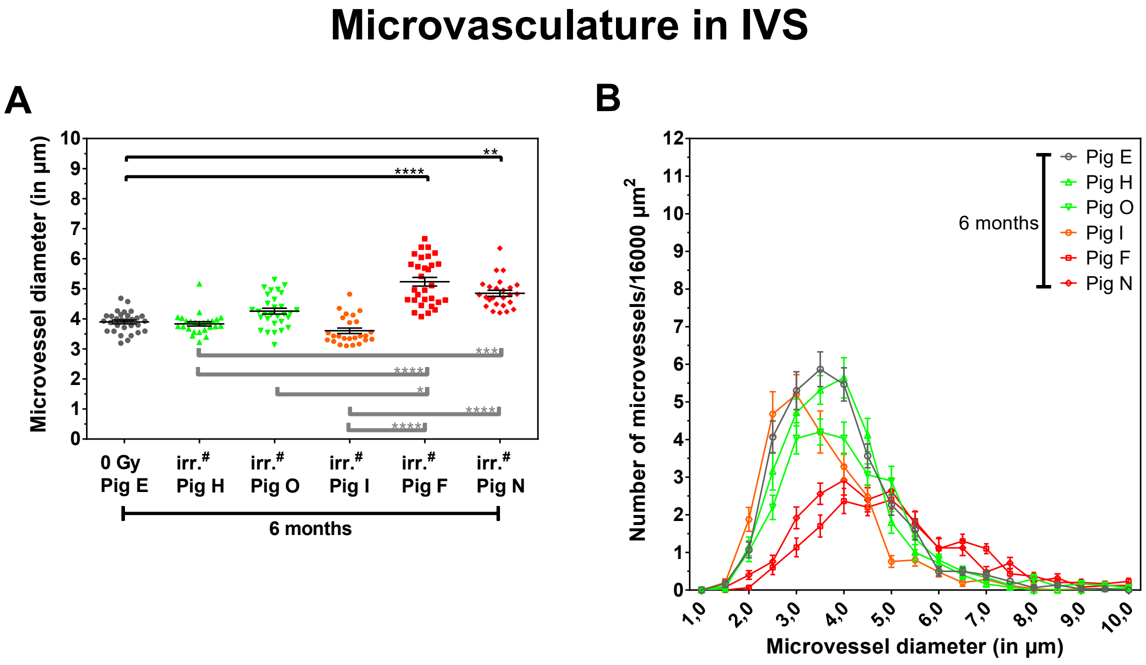

Figure 35: Loss of small vessels in the IVS only after high dose irradiated pigs six months after AVN carbon ion irradiation. The mean diameter of microvessels in the IVS (A) and the corresponding distribution of occurrences (B) were measured in myocardium six months after AVN targeted irradiation. The doses to the IVS were not determined = irr.$^{\#}$. Mean diameter, mean and SEM are shown. * = p-value ≤ 0.05, ** = p-value ≤ 0.01, *** = p-value ≤ 0.001, **** = p-value ≤ 0.0001. Significance was tested with one-way Kruskal Wallis statistic and Dunn´s post hoc test.

The distribution of the microvascular diameter in the myocardium of the sinistral entrance channel regions is in depicted in Figure 36. After LV irradiation, increased mean diameters were only detected three months after irradiation (Figure 36A). Likewise, there were also no changes in LAA six months after AVN irradiation with different doses (Figure 36C). As shown in the distribution of occurrences, a loss of small vessels with a diameter between 2 and 5 µm appeared in the LV entrance channel only three months after irradiation (Figure 36B and D) corresponding to the increase of the mean diameter.

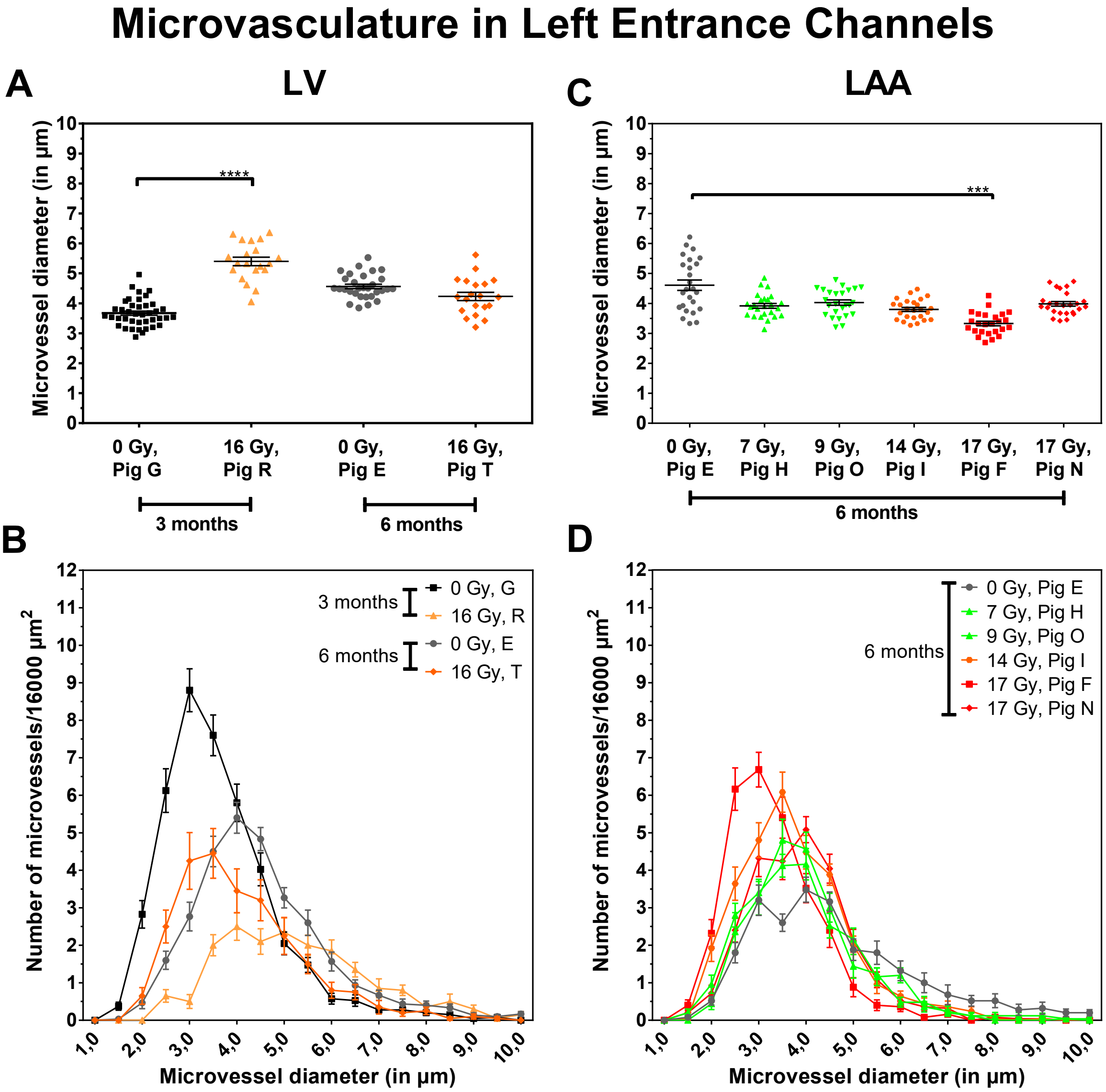

Figure 36: Loss of small vessels only three months after treatment in LV entrance channel regions. The mean diameter of microvessels in the LV (A) or LAA (C) entrance channel region and the corresponding frequency distribution (B and D) were measured in the myocardium. Mean diameter, mean and SEM are shown. * = p-value ≤ 0.05, ** = p-value ≤ 0.01, *** = p-value ≤ 0.001, **** = p-value ≤ 0.0001. Significance was tested with one-way Kruskal Wallis statistic and Dunn´s post hoc test.

In Figure 37, the mean diameter and the distribution of occurrences of the microvascular diameter in the myocardium of dextral entrance channel regions are depicted. No significant differences were observed over time in RV entrance channel regions after LV targeted irradiation (Figure 37A and B). In addition, no changes were detected in RAA entrance channel regions after AVN targeted irradiation irrespective of the doses (Figure 37C and D).

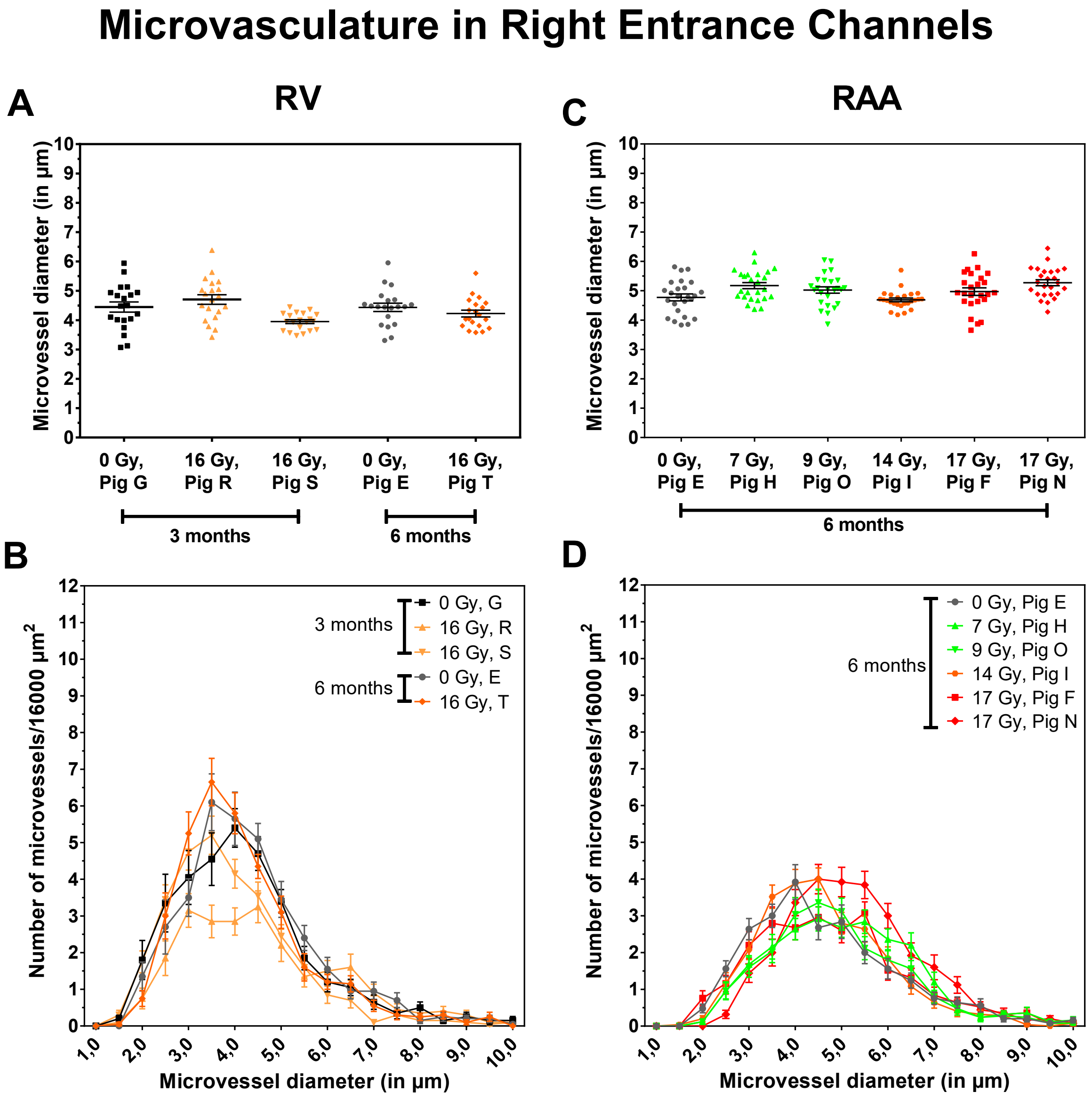

Figure 37: No changes in the distribution of the diameter of microvessels in dextral entrance channel regions. The mean diameter of microvessels in the RV (A) or RAA (C) entrance channel region and the corresponding frequency distribution (B and D) were measured in the myocardium of right entrance channel regions. Mean diameter, mean and SEM are shown. * = p-value ≤ 0.05, ** = p-value ≤ 0.01, *** = p-value ≤ 0.001, **** = p-value ≤ 0.0001. Significance was tested with one-way Kruskal Wallis statistic and Dunn´s post hoc test.

3.2.4. Presence of Iron-Containing Macrophages in Entrance Channel and Non-Targeted Regions

In Figure 38, the formation of siderophages, which was assessed as Golde score, is displayed for the whole IVS tissue six months after AVN target irradiation. Similar to the observations on haemorrhage and inflammation, higher Golde score levels were only observed in the IVS of the only one animal with persistent AV block (Pig F). The found patterns did not differ between myocardium and scar tissue (Appendix, Figure 57B and C). As shown above, different manifestations of damage (haemorrhage, inflammation and loss of microvessels) were mainly observed in the IVS of Pig F, which was the only animal with a persistent AV block. The parallel occurrence of damage in the IVS and the development of a persistent AV block lead to the hypothesis, that these two incidences were related. However, this hypothesis is speculative and requires further evidentiary proof.

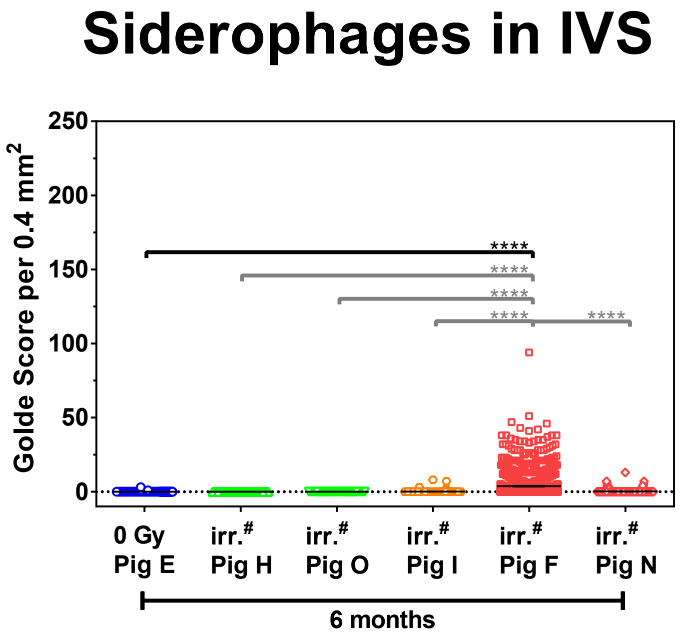

Figure 38: Augmented formation of siderophages was measured in the IVS of the one animal with persistent AV block (Pig F). The whole area of IVS was analysed six months after AVN targeted irradiation. The doses to the IVS were not determined = irr.$^{\#}$. Scoring per visual field, mean and SEM are shown. * = p-value ≤ 0.05, ** = p-value ≤ 0.01, *** = p-value ≤ 0.001, **** = p-value ≤ 0.0001. Significance was tested with one-way Kruskal Wallis statistic and Dunn´s post hoc test.

As shown in Figure 39 and Figure 40, the measurement of siderophages revealed, that they were not present in the whole area of sinistral and dextral entrance channel regions. This is in agreement with the low amount of haemorrhage in these areas (see Figure 30 and Figure 31).

Similar to the results obtained for the IVS, siderophages were evenly distributed among myocardium and scar tissue (Appendix, Figure 58and Figure 59B, C, E, and F).

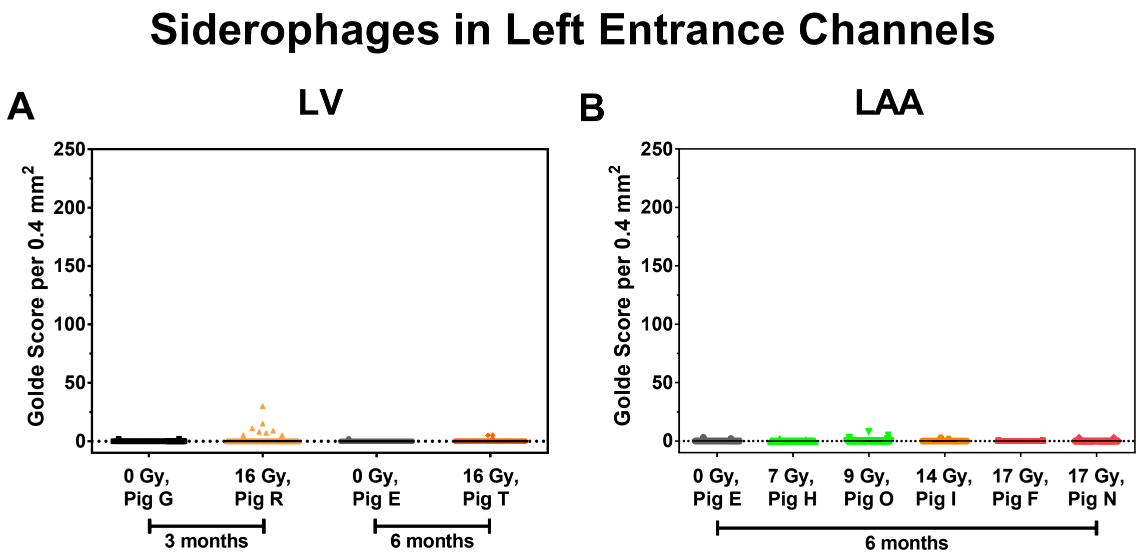

Figure 39: No detection of increased formation of siderophages in sinistral entrance channel regions. The whole area of sinistral entrance channel regions was analysed after LV (A) or AVN (B) targeted irradiation. Scoring per visual field, mean and SEM are shown. * = p-value ≤ 0.05, ** = p-value ≤ 0.01, *** = p-value ≤ 0.001, **** = p-value ≤ 0.0001. Significance was tested with one-way Kruskal Wallis statistic and Dunn´s post hoc test.

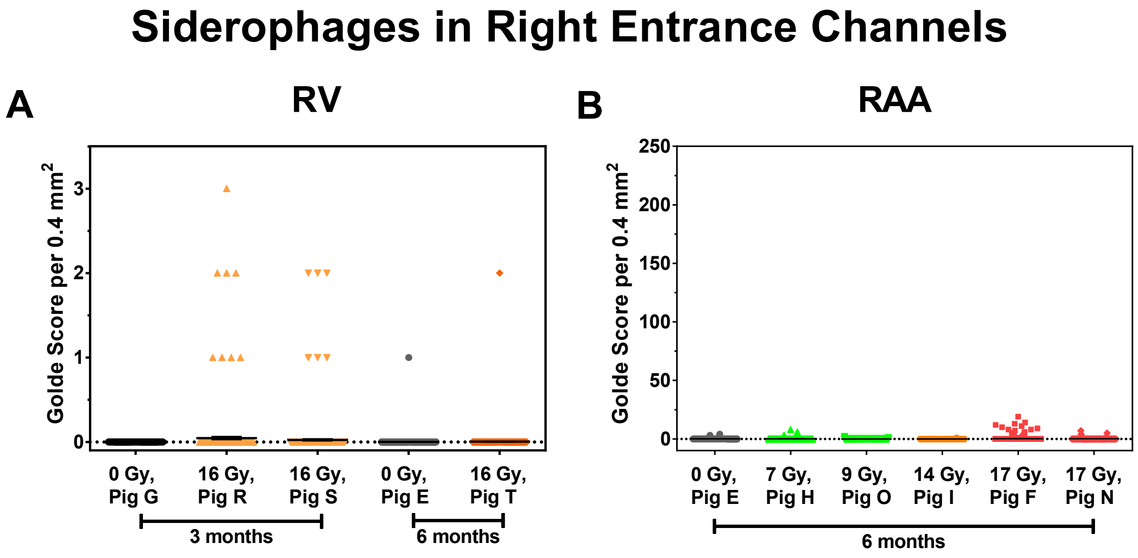

Figure 40: Similar to sinistral entrance channel regions, no evidence for formation of siderophages in dextral entrance channel regions. The whole area of dextral entrance channel regions was analysed after LV (A) or AVN (B) targeted irradiation. Scoring per visual field, mean and SEM are shown. * = p-value ≤ 0.05, ** = p-value ≤ 0.01, *** = p-value ≤ 0.001, **** = p-value ≤ 0.0001. Significance was tested with one-way Kruskal Wallis statistic and Dunn´s post hoc test.

3.3. Release of Soluble Necrotic Markers in Serum and Pericardial Fluid

Morphological analyses of LV and AVN targets after high dosed irradiation indicated the maturation of scar formation between three and six months after irradiation. One event in the course of myocardial remodelling is necrosis, in particular after high dosed irradiation (Strickberger, Tokano, Kluiwstra, Morady, & Cain, 1999) and cardiovascular events (Newby, 2004). In the course of necrosis, the cellular membrane becomes leaky causing cells to swell and subsequently disrupt. This process leads to the release of cellular components into the extracellular space and inflammation of the tissue. Therefore, necrosis is characterized by the release of cellular fragments into their immediate surroundings, which can be detected as soluble markers (Pezzutto, Ulrichs, & Burmester, 2007). In the presented study necrotic markers were analysed in pericardial fluid (PF) and serum. PF was only available six months after irradiation for technical reasons and serum was collected shortly before and again at several time points after irradiation (four, eight, twelve and twenty-four weeks after irradiation). One cellular component, which is released only after necrosis, is HMGB1, a DNA binding protein (Lin, Chen, Li, & Fang, 2015). Consequently, HMGB1 was used as a general soluble marker of necrosis in the presented study. As the detection of HMGB1 was inconclusive (Appendix, Figure 62), markers of the necrosis of specific cell types were investigated.

The von Willebrand factor (vWF) is released by necrotic endothelial cells (EC). Accordingly, the loss of microvasculature was found after the application of high to medium doses to cardiac tissue (3.1.3 and 3.2.3), which could be related to the necrosis of EC. The measurement of vWF demonstrated no significant changes after LV and AVN irradiation in the PF or the serum at different time points (Appendix, Figure 62).

Cardiac troponin T is part of the cytoskeleton of cardiomyocytes. It is typically released due to ischemia after for example a myocardial infarct (MI). For that reason, the detection of cardiac troponin T is also performed in clinical routine (Gonzalez et al., 2009; Kemp, Donovan, Higham, & Hooper, 2004; Newby, 2004). The measurement of cardiac troponin T in PF demonstrated no significant changes of cardiac troponin T concentration compared to respective control. Only in the PF of Pig T (LV 40 Gy), a significant increase of cardiac troponin T compared to Pig I (AVN 40 Gy, AV block) was detected (Figure 41).

In serum samples, the absence of changes over time (Appendix, Figure 61 and Figure 62) confirmed the overall results of necrotic markers in PF. In summary, irradiation–induced necrosis was only observed for cardiomyocytes after the irradiation of the largest target volume.

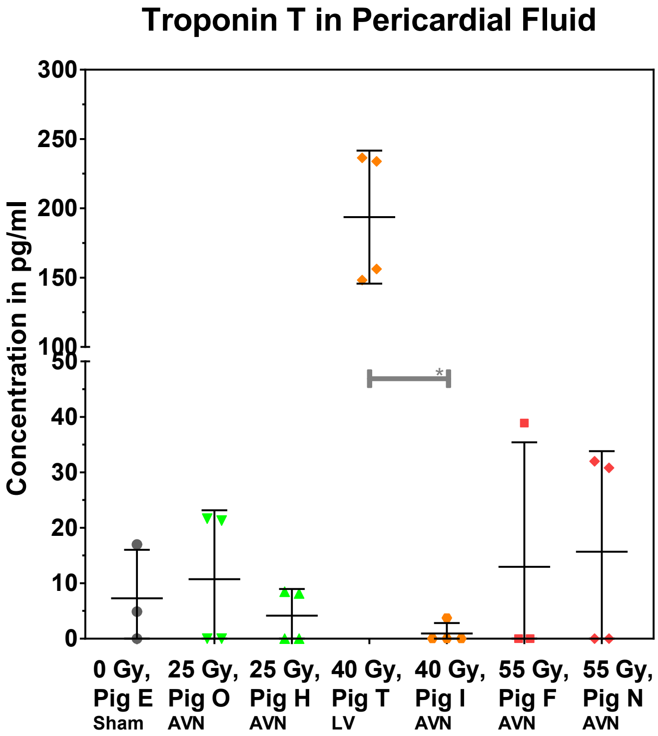

Figure 41: Raised levels of troponin T were only detected after LV target irradiation. Troponin T concentrations were measured six months after irradiation in PF. Concentration of technical replicates, mean and SEM are shown. * = p-value ≤ 0.05, ** = p-value ≤ 0.01, *** = p-value ≤ 0.001, **** = p-value ≤ 0.0001. Significance was tested with one-way Kruskal Wallis statistic and Dunn´s post hoc test.

3.4. Cytokine Release in Serum and Pericardial Fluid

As morphological analyses revealed time- and dose-dependent inflammation of irradiated cardiac tissue (3.1.2 and 3.2.2), cardiac and systemic inflammation were investigated more closely. For the quantification of inflammation, pro- and anti-inflammatory cytokines were measured in PF and serum. The collection of PF was only possible after six months, whereas serum was available at several time points after irradiation. The detection of pro– and anti–inflammatory cytokines in the serum revealed no changes at any time point (Appendix, Figure 63, Figure 64, Figure 65, Figure 66, and Figure 67). Likewise, no changes in the release of IL-6, IFN-γ and IL-4 in the PF were detected (Appendix, Figure 64, Figure 66, and Figure 67).

The irradiation-induced release of pro-inflammatory markers in PF is depicted in Figure 42: Only in the PF of Pig T (LV 40 Gy), increased TNFα, IL-1β and IL-8 release were measured, which indicates no correlation with dose, but maybe with the size of the targeted area. For CRP, no changes in the PF of irradiated pigs were detected compared to the sham control. Only in the PF of Pig O (AVN 25 Gy) and N (AVN 55 Gy), increased CRP concentrations were measured compared to other irradiated pigs (I and F, both with AV block). These results indicate no acute inflammation correlating with AV block or dose.

Pro-Inflammatory Cytokines in Pericardial Fluid

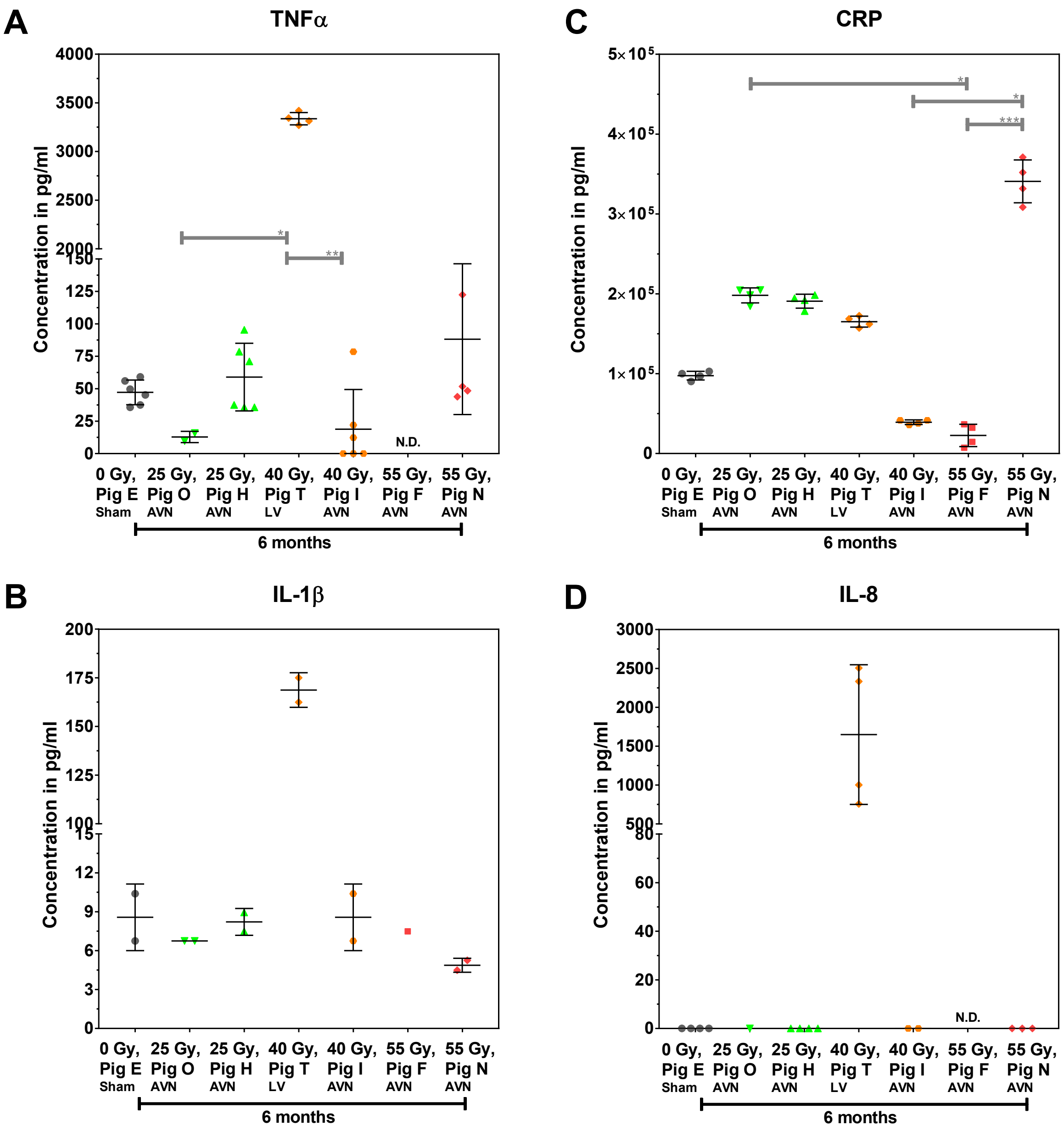

Figure 42: An increased release of pro-inflammatory cytokines was recurrently measured in the PF of the LV targeted animal (Pig T). TNFα (A), IL-1β (B), CRP (C) and IL-8 (D) concentrations were measured six months after irradiation in PF. Concentration of technical replicates, mean and SEM are shown. N.D. = not determined. * = p-value ≤ 0.05, ** = p-value ≤ 0.01, *** = p-value ≤ 0.001, **** = p-value ≤ 0.0001. Significance was tested with one-way Kruskal Wallis statistic and Dunn´s post hoc test.

The detection of pro–inflammatory cytokines was complemented with the identification of the release of anti–inflammatory cytokines, represented by IL-10, which also has anti–fibrotic properties (Behrends, Bischofberger, & Deutzmann, 2012; Wynn, 2004). An increased release of IL-10 was only observed in PF of Pig T (LV 40 Gy) compared to the respective control and other pigs (Figure 43). With respect to the IL-10 release in serum of Pig T (LV 40 Gy) at the day of irradiation, no irradiation-induced changes were observable in the serum of LV and AVN irradiated pigs (Appendix, Figure 67). In addition to the measurements of IL-10, IL-4 release was also examined, which acts as an anti–inflammatory and pro–fibrotic mediator (Biernacka & Frangogiannis, 2011; Jakubzick et al., 2003; Taunk et al., 2015; Wynn, 2004). No changes were detected for the release of IL-4 in PF and serum at several time points (Appendix, Figure 67). In summary, these results indicate that a regulation of inflammatory processes occurred six months after irradiation without further induction of fibrosis by soluble mediators.

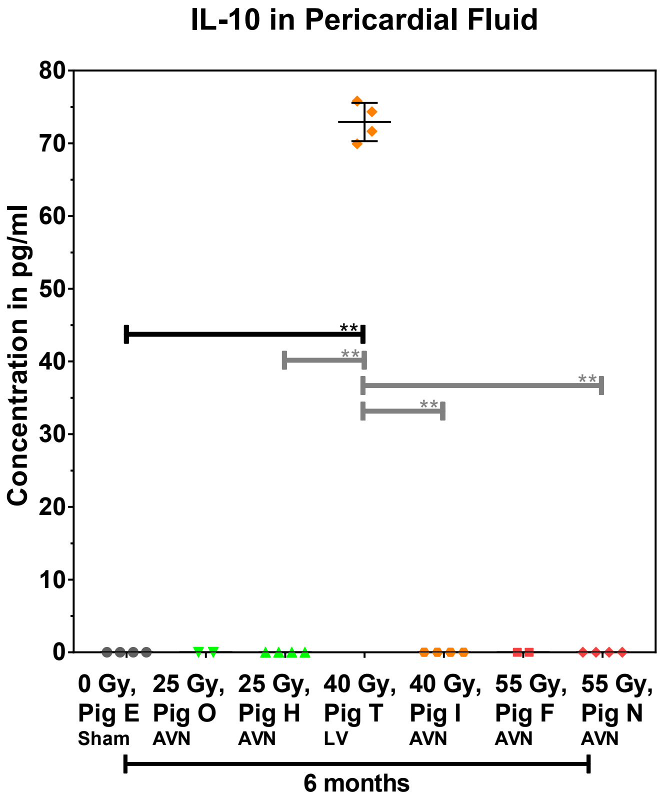

Figure 43: Similar to pro-inflammatory cytokines, higher concentrations of IL-10 were only discovered after LV irradiation. IL-10 concentrations were measured six months after irradiation in PF. Concentration of technical replicates, mean and SEM are shown. * = p-value ≤ 0.05, ** = p-value ≤ 0.01, *** = p-value ≤ 0.001, **** = p-value ≤ 0.0001. Significance was tested with one-way Kruskal Wallis statistic and Dunn´s post hoc test.

4. Discussion

This thesis was performed in the frame of a project for cardiac ablation using high dosed irradiation of small volumes. For this approach, two cardiac substructures clinically relevant for the treatment of cardiac arrhythmias (CA), namely the left ventricle (LV) and the atrio-ventricular node (AVN), were irradiated in a porcine model. A successful ablation of target areas might show that carbon ion irradiation can serve as innovative treatment method of CA (Lehmann et al., 2016). The challenge was to achieve the ablation of target areas without damaging non-targeted areas. The successful ablation of target areas is putatively accomplished by the induction of fibrogenic mechanisms (Lehmann et al., 2016; Taunk et al., 2015).

However, the exact underlying biological effects of this project are unknown. Preliminary results indicated the repeated appearance of haemorrhage and inflammation (Lehmann et al., 2016). As scar formation was apparently not completed, the detection of microvascular damage gave hints on the persistence of tissue remodelling, which presumably leads to the formation of a mature fibrous scar (Adams et al., 2003; Biernacka & Frangogiannis, 2011; Fajardo & Stewart, 1971; Schultz-Hector & Trott, 2007; Talman & Ruskoaho, 2016). Therefore, the goal of this thesis was to analyse microvascular damage and subsequent tissue responses after carbon ion irradiation of small volumes (1 – 1.5 cm^3). Within these studies, the intended damage in target areas and the unwanted effects in non-targeted areas were investigated.

Consequently, different aspects of microvascular damage were studied in the pig hearts. Haemorrhage and loss of microvasculature were detected at both investigated time points (three and six months after irradiation) indicating that they appeared repeatedly. In parallel to vascular damage, inflammation and the presence of macrophages, which had engulfed iron particles (siderophages), were observed at both investigated time points. The presence of siderophages indicates precedent haemorrhage. To summarize, vascular damage had appeared before the first investigated time point and persisted until the end of the project. In the target tissue, scar formation was observed side by side with almost unaffected myocardium. Consequently, both tissue types were analysed separately. For the complementation of histological analyses, the measurement of soluble markers of necrosis and inflammation gave hints on the necrosis of cardiomyocytes after irradiation. The results of these analyses demonstrated that no systemic inflammation developed after carbon ion irradiation of cardiac substructures.

4.1. Haemorrhage and Inflammation as Early Events of Tissue Remodelling

Prevalent observations in this study were haemorrhage and inflammation in target areas as well as entrance channel regions. These tissue responses are described as early events of tissue remodelling (Chrastina et al., 2014; Hall & Giaccia, 2006; Reece & Urry, 2011; Talman & Ruskoaho, 2016). Both responses were assessed with a scoring system for the amount of either erythrocytes or immune cells and compared to sham controls of the respective time point.

In the target tissue, both haemorrhage and inflammation were most pronounced three months after irradiation with high doses and declined until six months after irradiation. However, they did not reach control level again. Substantial amounts were found in targets with strong fibrotic response (Figure 24 and Figure 25). Remarkably, the irradiation with medium doses in entrance channel regions also caused higher levels of haemorrhage and inflammation than in the sham control at both time points. These effects were less marked than in the target areas. In contrast to target areas, the occurrence of haemorrhage and inflammation remained unchanged over time in entrance channel regions (Figure 30, Figure 31, Figure 33, and Figure 34).

4.1.1. Delayed Manifestation of Haemorrhage and Inflammation after the Exposure to High Doses

The vascular damage caused by the ligation of a blood vessel is similar to the one caused by the initial events of irradiation as shown in models for myocardial infarct (MI) (Baldi et al., 2002; Prech et al., 2010; Virag & Murry, 2003). However, their induction is more controlled and isolated from other influences during ligation. Accordingly, Virag and Murry elicited a defined damage to the myocardium by ligating the supplying blood vessel (Virag & Murry, 2003). Similar to the findings of this thesis, Virag and Murry reported the dysfunction of endothelial cells (EC) after the ligation of a coronary artery in murine hearts, which was related to haemorrhage and inflammation. In contrast to irradiation-induced damage, ligation caused the manifestation of damage in an earlier time frame (between a few days and two weeks after treatment) (Virag & Murry, 2003).

However, the delayed manifestation of irradiation–induced tissue reactions is well-known (Chrastina et al., 2014; Hall & Giaccia, 2006; Reece & Urry, 2011; Talman & Ruskoaho, 2016). Accordingly, the repeated occurrence of vascular damage and inflammation was reported for at least 7 – 60 weeks after the irradiation of whole hearts with 8 – 20 Gy X-ray in murine and rabbit models, (Fajardo & Stewart, 1971; Seemann et al., 2012; Washington et al., 2013). This is in agreement with the observations presented here. The difference between the exclusively early occurrence of vascular damage and inflammation after ligation and their repeated appearance over a longer period of time by irradiation can be explained with the following hypothesis: Vascular damage due to ligation manifested at once because of the instant malnourishment of the tissue. In contrast, irradiation causes DNA damage, which can be tolerated by EC up to a certain degree. If this threshold of tolerable damage is exceeded and regular or irradiation–induced tissue turnover leads to angiogenic signalling, the proliferation of EC fails, because the DNA damage cannot be repaired. This order of events eventually leads to the depletion of EC. Accordingly, Hopewell et al. as well as Fajardo and Stewart also observed EC damage and loss over a period of months. They stated that vascular cells in the heart have a slow turnover, which was accelerated, but still slow after irradiation with 25 Gy X-ray (Fajardo & Stewart, 1971; Hopewell et al., 1986). Consequently, this slow turnover could be the reason for the repeated manifestation of vascular damage over a long period of time.

4.1.2. Occurrence of Haemorrhage and Inflammation in parallel to the Degeneration of the Myocardium

In the presented work, the recurrent occurrence of haemorrhage and inflammation was observed in myocardium and scar tissue. Their appearance in myocardium corresponds to the current understanding of the first stage of cardiac fibrosis. In this stage, the replacement of healthy myocardium takes place due to their deterioration and cell death (Biernacka & Frangogiannis, 2011; Talman & Ruskoaho, 2016). However, a morphologically altered myocardium was not recognized as myocardium in this thesis. Instead it was termed as scar tissue (Material and Methods, Figure 13). Consequently, the appearance of haemorrhage and inflammation in morphologically unaffected myocardium occurred in parallel also in already deteriorated tissue. This finding can be interpreted as a later phase of the first stage of cardiac fibrosis. To summarize, the observation of haemorrhage and inflammation in an increasing amount of scar tissue suggests the parallel appearance of different phases of the first stage of cardiac fibrosis.

4.1.3. Delayed Manifestation of Haemorrhage and Inflammation after the Exposure to Medium Doses

In addition to the target regions, entrance channel areas were also analysed. These investigations were performed to determine, if the exposure upon medium doses induced potential side effects. Although the amount of scar formation did not increase in most entrance channel regions, haemorrhage and inflammation appeared in both myocardium and cardiac connective tissue, which was referred to as scar tissue (Material and Methods, Figure 13). These results demonstrate that early stages of tissue remodelling also occurred in the entrance channel regions. However, they appeared less pronounced compared to target areas. The unvarying levels of their appearance points to a slower manifestation of these responses. Therefore, these observations were interpreted as a delayed occurrence. Comparably, the later occurrence of tissue damage after medium doses compared to higher doses was also shown in various sources (Adams et al., 2003; Fajardo & Stewart, 1970; Kiscsatári et al., 2016; Schultz-Hector & Trott, 2007).

The lower amount of haemorrhage and inflammation in the entrance channel regions compared to target areas might be based on less DNA damage following medium dosed irradiation. This DNA damage was then tolerated and therefore accumulated for a longer period of time. This incidence was also described for cell cultures (Hall & Giaccia, 2006). Consequently, cell death at a certain time point occurred in a smaller fraction of cells during regular or irradiation-induced tissue turnover, which is also already established (Hopewell et al., 1986).

In summary, tissue remodelling was more advanced after high doses. Moreover, the exposure to medium doses led to a comparably slower progression of tissue remodelling than in target areas. This observation matches an exclusively early phase of the first stage of tissue remodelling in entrance channel regions.

4.1.4. Induction of Cardiac Fibrosis by the Applied Doses

In radiobiology, tissue remodelling leading to fibrosis is a deterministic effect, meaning it is only induced above a threshold dose. This means for the presented thesis that, if the threshold dose for this process was already exceeded by the application of medium doses in the entrance channels, fibrosis was induced. This implication is a limiting factor for carbon ion irradiation as alternative treatment method for CA. With regard to the induction of fibrosis, early events of tissue remodelling were observed in most entrance channel regions in this study. Moreover, the LV entrance channel region also exhibited an increasing proportion of scar tissue until six months after irradiation. However, the scar formation was less marked than in target areas. This implies that the threshold dose for the development of fibrosis was already crossed applying medium dosed carbon ion irradiation in entrance channel regions.

Accordingly, Yan and co-workers published a study on the induction of cardiac fibrosis after whole body irradiation of mice with charged particles. They proved the development of cardiac fibrosis three months after irradiation with low doses (0.5 Gy protons and 0.15 Gy Fe ions) (Yan et al., 2014). The results of this study confirm the findings of the presented thesis. They also indicate that the threshold dose for the induction of cardiac fibrosis after charged particle irradiation is below the applied doses in this presented work.

The influence of the volume effect for the progression of fibrosis after carbon ions irradiation was further investigated in rat lungs: When only 50 % of the lung instead of the whole organ was irradiated with medium doses (17.25 Gy), less fibrosis was detected in the irradiated areas (Dettmering, 2013; Ghobadi et al., 2012).

To synopsise, as only cardiac substructures (1 - 1.5 cm^3) were irradiated with medium doses of carbon ions in the presented study, the time frame for the development of cardiac fibrosis cannot be directly deduced from the findings of Yan and co-workers as described above. However, the comparison of this study with other sources validate that the progression of cardiac fibrosis is slower after the exposure upon medium doses in entrance channel regions than after high doses in the target areas.

Moreover, Yan et al. detected further progression of cardiac fibrosis until at least ten months after irradiation (Yan et al., 2014). The ongoing tissue remodelling in target areas proves that irradiation-induced fibrosis was not completed until the last investigated time point (six months after irradiation) in the presented study. As discussed above, the reason for the delayed occurrence of scar formation after medium doses could be the later manifestation of vascular damage in the course of tissue turnover. This delayed damage manifestation would subsequently also cause the formation of scar tissue over a longer period of time.

Comparably, the mortality of patients after exposure to low or medium dosed irradiation is often related to the spreading of fibrosis through the myocardium over decades (Adams et al., 2003; Heidenreich & Kapoor, 2009; Schultz-Hector & Trott, 2007; Taunk et al., 2015). These findings support the hypothesis of a slower progression of fibrogenic mechanisms upon low to medium doses. Inferring from these data, the formation of a fibrous scar in entrance channel regions might occur decades after this treatment. As the ablation of arrhythmogenic substrates is mainly applied in older individuals, these late manifestations would not constitute urgent limitations of this method. These implications were also described in other sources (Calkins et al., 2012; Chugh et al., 2014; Schultz-Hector & Trott, 2007; Verdino, 2015).

4.2. Loss of Microvessels in Non-Fibrotic Myocardium

In accordance with the three stages of tissue remodelling, the loss of microvascular density is established as an early step in the development of cardiac fibrosis. This was shown in animal models and patient studies (Fajardo & Stewart, 1971; Prech et al., 2010; Seemann et al., 2012; Virag & Murry, 2003; Washington et al., 2013). In this thesis, the investigations on small vessels in the myocardium comprised the measurement of their diameter per visual field.

In target areas, a dose-dependent loss of up to 74 % of the microvasculature with a small diameter (between 2 and 5 µm) was observed at both time points (Figure 26). Consequently, the mean microvascular diameter of the remaining vessels was larger in the irradiated tissue than in the respective control. In parallel, the extension of scar tissue was detected in target areas (Table 9 and Table 11). In contrast to high dosed irradiation in target areas, medium doses (7 – 17 Gy) in the entrance channel regions only caused the loss of small vessels in the LV entrance channel region and not in the other entrance channel areas (Figure 36, Figure 37, Table 15, and Table 16). This could be attributed to the treatment planning, which lead to a higher dose deposition in the LV entrance channel region, because it was closer to the target areas than the other examined entrance channel regions (Figure 44). However, the precise doses in the entrance channel regions areas were not reconstructed. Furthermore, the LV entrance channel region was the only one, where more scar tissue was observed than in sham controls (Table 12, Table 14, Table 15, and Table 16). Nevertheless, the increased amount of scar tissue in the LV entrance channel compared to controls was less pronounced than in target areas.

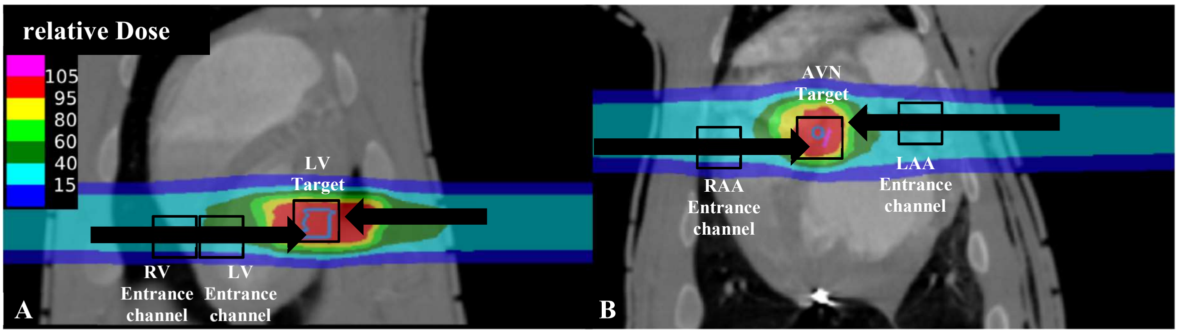

Figure 44: CT scans of the heart with exemplary dosecuts from the coronal (right) view. Targets and entrance channel regions are indicated for the irradiation of the LV (A) and the AVN (B). Regions, where tissue was harvested for analyses, are highlighted with boxes. Modified after (Eichhorn, 2016).

4.2.1. Dose-Dependent Loss of Microvessels

In the presented thesis, a dose-dependent loss of microvessels was detected. This held in particular true for the target areas and LV entrance channel region. In the following section, these findings are discussed with the results of other sources.

In contrast to the observed loss of microvasculature, more capillaries were transiently observed in murine and rabbit hearts within the first days to 20 weeks after whole heart irradiation with 2 to 20 Gy X-irradiation (Fajardo & Stewart, 1970; Seemann et al., 2012; Washington et al., 2013). Furthermore, a dose-dependent proliferation of EC was reported one to twelve months after 17.5 – 25 Gy X-irradiation of whole rabbit hearts and rat brain tissue (Fajardo & Stewart, 1971; Hopewell et al., 1986). However, simultaneously to EC proliferation (measured with radioactive labelling of EC), the loss of EC was detected (determined by the total number of EC), which was interpreted as an increased EC turnover (Fajardo & Stewart, 1971; Hopewell et al., 1986). Apparently, this increased overall turnover of EC does not prevent the loss of microvasculature after irradiation as the damage was too severe to be repaired. This inference was also reported by other groups (Adams et al., 2003; Fajardo & Stewart, 1971; Hopewell et al., 1986; Prech et al., 2010; Schultz-Hector & Trott, 2007).

In the presented study, no indication for a transient increase of microvasculature was obtained in the small irradiated volume of pig hearts. Assuming that the observed loss of microvasculature is preceded by a transient increase of capillaries, it is possible that the investigation of the tissue at the first time point (three months after irradiation) was already too late to detect an increased capillary density. In contrast, the detected loss of microvessels was also reported in literature. It mainly occurred after the transient increase (Fajardo & Stewart, 1970; Seemann et al., 2012; Washington et al., 2013).

Moreover, the loss of microvessels was dose-dependent. This finding indicates that a *de novo* formation of microvessels is impeded by the highest doses (40 and 55 Gy). This observation could be attributed to a suppression of angiogenesis with dose, which is also described in literature (Seemann et al., 2012).

4.2.2. Indirect Causes for the Loss of Small Vessels

The observed loss of microvessels can also be evoked by additional, indirect irradiation effects like a partial or complete occlusion of bigger vessels. This occlusion of bigger vessels might cause local hypertension, which would subsequently result in the loss of EC (Ghobadi et al., 2012). Within this project, no coronary artery was irradiated, which excludes the influence of occluded bigger blood vessels. However, the occlusion of medium sized vessels was observed sporadically in the target areas (Figure 23). In order to quantify the occlusion of medium sized vessels, further investigations need to be carried out. They could give insights into the interplay between the occlusion of medium sized vessels and its relevance for the loss of microvessels. However, these investigations are not as essential for the prediction of further tissue remodelling as the analyses of microvessels.

4.2.3. Indications of a Threshold Dose for the Loss of Microvessels

The microvascular changes after the application of medium doses (7 – 17 Gy), which were most prominent in the LV entrance channel region, points to a potential threshold for this particular effect. Below this threshold, tissue damage can be compensated by the migration and differentiation of progenitor cells into functional cells or proliferation of resident tissue cells as reported in literature (Biernacka & Frangogiannis, 2011; Talman & Ruskoaho, 2016; Uchida et al., 2012). In addition, a threshold also depends on the irradiated volume, which is tissue-specific (Ghobadi et al., 2012; Hopewell et al., 1986; Karger et al., 2006). However, such a threshold can be used to predict the induction of tissue damage after irradiation. This knowledge is crucial for the irradiation of normal tissue during radiotherapy.

Until now, no definite threshold was described for the loss of microvessels in cardiac tissue. An underlying mechanism for such a threshold could be DNA damage induction after irradiation exceeding the repair capacity of EC. Consequently, cell death might occur. Besides failed DNA repair, a threshold could also be based on a changed phenotype of EC: Surviving EC after irradiation were reported to acquire a senescence–associated phenotype, which is more prone to cause a pro–inflammatory environment and has less angiogenic capabilities. The doses to cause this change in phenotypes in endothelial cell culture systems was 2 – 8 Gy x-ray (Cervelli et al., 2014; Chen et al., 2009; Potiron et al., 2013; Ungvari et al., 2013). Whole heart X-irradiation in animal models caused endothelial cell death between 12 and 20 Gy (Fajardo & Stewart, 1971; Washington et al., 2013).

In the presented work, irradiation with medium doses to entrance channel regions was performed with carbon ions, which are known to have a higher RBE than photon irradiation (Gemmel et al., 2011; Hall & Giaccia, 2006; Kraft, 2000). Although the exact RBE for the loss of microvessels was not evaluated, the doses to the entrance channel regions were presumably high enough to cause a level of DNA damage in EC resulting in their depletion.

Accordingly, the loss of microvessels in the LV entrance channel region was detected at three months but not at six months after irradiation in the presented study. One interpretation of this result could be that the vascular damage caused morphological changes of the affected myocardium. Consequently, the myocardium underwent morphological changes due to tissue remodelling and was therefore identified as scar tissue (Material and Methods, Figure 13). Correspondingly, an increased amount of scar tissue was measured in LV entrance channel regions.

4.2.4. Alternative Stainings for Vascular Remodelling and their Prospects

In the presented thesis, microvasculature could only be detected in the myocardium, because the applied histological staining method (Verhoeff van Gieson stain) was not reliable in scar or cardiac connective tissue. If the detection of microvessels in scar tissue would be available, the analysis on microvasculature could serve as an indicator for the maturation of scar tissue as described in literature (Biernacka & Frangogiannis, 2011; Talman & Ruskoaho, 2016). Moreover, specific markers would allow for the distinct identification of microvessels (blood or lymph vessels). Unfortunately, specific marker labelling for EC (CD31, CD34 and vWF) was only reliable for bigger and not for small vessels during the preparation of this thesis. As shown in the presented thesis (Figure 45), microvessels were not stained sufficiently using typical EC markers alone or in combination (CD31, CD34 and vWF). Similar technical problems are reported in other sources: In murine and human heart tissue, typical markers of EC (CD31, CD34, vWF, VE-cadherin, etc.) were only irregularly or not at all presented by capillaries (Pusztaszeri, Seelentag, & Bosman, 2006; Schrage et al., 2008).

The occurrence of vascular damage is often associated with malnourishment and hypoxic conditions in the tissue (Adams et al., 2003; Meyer et al., 2016; Washington et al., 2013). Hypoxia is classically shown by the visualization of EF5 or pimonidazole, which needs to be applied already in the living animals. Another possibility for detection of hypoxia are HBFP staining or the investigation of the expression and subsequent translocation of HIF-1α into the nucleus (Bergeron et al., 1999; Lee, Bae, Jeong, Kim, & Kim, 2004; Varia et al., 1998). In the presented project, neither EF5 nor pimonidazole were applied before the sacrifice. Instead, TTC was injected, which is a marker for hypoxia in brain tissue (Bederson et al., 1986). However, TTC was not detectable in cardiac tissue sections due to the limited staining contrast. The analysis of HBFP and HIF-1α staining was inconclusive (Figure 47 and Figure 46) in the presented study, most likely because the niche for cardiomyocyte progenitor cells requires hypoxic conditions (Kocabas et al., 2012), which led to inconsistent results. However, the detection of released troponin T in the pericardial fluid (PF) (Figure 41) after irradiation points to hypoxic areas in the irradiated myocardium.

Comprehensively, irradiation–induced microvascular changes could only be detected in the myocardium. The loss of microvessels appeared presumably due to a change of phenotypes or DNA damage, which exceeded the vascular repair capability. However, the investigations on subsequent hypoxia in the myocardium require further evidentiary proof.

4.3. Link between Haemorrhage and Scar formation

The prior manifestation of haemorrhage in tissue can be retraced by the presence of siderophages: After the disruption of blood vessels, inflammation and subsequent phagocytosis of blood components by immune cells occurs. In case of a surplus of iron in cells, the transformation into siderophages is induced. The appearance of siderophages can be quantified using the Golde score (Lederer et al., 2014), which was adapted for this thesis.

The visualization of siderophages in myocardium and scar tissue gave insights into scar formation: In myocardium, an increased number of siderophages points to prior haemorrhage, which are indicators of the first phase of tissue remodelling (Biernacka & Frangogiannis, 2011; Fajardo & Stewart, 1970, 1971; Talman & Ruskoaho, 2016). In scar tissue, similar observations show either previous haemorrhage in myocardium, which was then re-organized, or recurrent appearance of haemorrhage in scar tissue, because the maturation process was not yet completed. Therefore, the pronounced number of siderophages in scar tissue only demonstrated that haemorrhage occurred, but cannot be assigned to a designated stage of tissue remodelling. In target areas, the number of siderophages increased over time and with dose in scar tissue (Appendix, Figure 56C and F). In the myocardium of target areas, the formation of siderophages was exclusively observed six months after irradiation (Appendix, Figure 56B and E). In myocardium and scar tissue of entrance channel regions, the formation of siderophages was not observed after the exposure to medium doses (Appendix, Figure 58 and Figure 59).

4.3.1. Location of Siderophages after the Exposure to High Doses

Haemorrhage is a typical early event of cardiac fibrosis, although the connection between haemorrhage and scar formation after irradiation is only hypothesized (Chrastina et al., 2014; Fajardo & Stewart, 1971; Washington et al., 2013). Nevertheless, this link was already established in other conditions than irradiation-induced cardiac fibrosis. Investigations of these syndromes were carried out using siderophages as indicators of prior haemorrhage (Fisher et al., 2010; Lederer et al., 2014; Shirota et al., 2013). Accordingly, siderophages were found in the myocardium and scar tissue of target areas in the presented thesis. As one major concern was to find a link between the occurrence of microvascular damage and tissue remodelling, the interpretation of the location of siderophages is crucial.

As indicated above (4.3), the presence of siderophages in myocardium point to the appearance of haemorrhage, which did not lead to histological alterations yet. The occurrence of siderophages in scar tissue however can indicate that A) haemorrhage in myocardium already caused morphological changes or B) repeated appearance of haemorrhage in scar tissue. The larger amount of scar tissue after irradiation points to earlier manifestations of microvascular damage like haemorrhage. Therefore, the higher number of siderophages in the extending scar tissue indicate that haemorrhage in the myocardium already led to its remodelling into scar tissue (option A). Consequently, the occurrence of haemorrhage and siderophages in myocardium at six months after irradiation shows that the remodelling of the myocardium into scar tissue was still ongoing.

4.3.2. Delayed Formation of Siderophages after the Exposure to Medium Doses

In contrast to the target areas, siderophages were not found upon the exposure to medium doses in the entrance channel regions. Interestingly, haemorrhage was observed three and six months after irradiation in entrance channel regions, but to a lower extent than in target areas (Appendix, Figure 56, Figure 58, and Figure 59). Consequently, the amount of haemorrhage until the investigated time points was not sufficient to trigger the formation of siderophages, which can be detected after at least a few days after haemorrhage (Lederer et al., 2014).

Another possibility for the absence of siderophages in entrance channel areas could be that siderophages were formed, but migrated out of the entrance channel areas and were subsequently not detectable anymore. This hypothesis though does not concur with the measurement of siderophages in target areas and was neither observed in other studies (Fisher et al., 2010; Lederer et al., 2014; Shirota et al., 2013). Therefore, the differentiation of macrophages and other cell types into siderophages was presumably not triggered in entrance channel regions, because this damage could be repaired without causing the formation of siderophages.

In literature, the formation of siderophages was observed between two and forty weeks after the irradiation of whole hearts with a laser beam (72 J/cm and additional photosensitizer) or different doses of X-rays (8 – 16 Gy). They occurred simultaneously to increased ECM production (Chrastina et al., 2014; Lederer et al., 2014; Seemann et al., 2012), which is a marker of the second and third stage of cardiac fibrosis (Biernacka & Frangogiannis, 2011; Talman & Ruskoaho, 2016).

In contrast to these findings, similar medium doses in the entrance channel regions did not lead to the formation of siderophages, although they were detected after irradiation with higher doses in target areas. As discussed above, the absence of siderophages proves that the amount of haemorrhage was not sufficient to trigger this process in entrance channel regions. The discrepancy between the results reported in literature and the presented study can be related to differences of the irradiated volume (whole hearts in literature and only 1 – 1.5 cm^3 in the presented thesis): The irradiation of a greater volume in other experimental setups caused a larger amount of haemorrhage subsequently activating the formation of siderophages.

The results of this thesis are confirmed by the studies of Ghobadi as well as Karger and their co-workers. They demonstrated that the application of lower doses in larger volumes leads to more damage than the application of high doses to small volumes. These effects were investigated in lung and spinal cord tissue of rats (Ghobadi et al., 2012; Karger et al., 2006).

This supports the assumption that comparable doses to smaller volumes caused less damage than to larger volumes during the investigated periods of time. Furthermore, the repeated occurrence of haemorrhage, which manifested during tissue turnover (4.1.3 and 4.2.1), point towards an ongoing tissue remodelling process. Therefore, also the low amount of haemorrhage in entrance channel regions after the application of medium doses will lead to the formation of siderophages and finally fibrosis.

4.3.3. Role of Siderophages in Scar Tissue

The function of siderophages besides clearance of blood components from damaged tissue was not determined further. So far it was hypothesized that they contribute to the progression of fibrogenic processes (Fisher et al., 2010; Lederer et al., 2014; Seemann et al., 2012; Shirota et al., 2013). In the course of inflammation and fibrosis, two main groups of macrophages (M1 and M2) were designated. M1 macrophages were described as cytotoxic, contributing to a pro-inflammatory microenvironment and iron retention. In contrast, M2 macrophages are often tissue-resident and associated with wound healing and recycling of iron (Mantovani & Locati, 2016).

The differentiation of macrophages into siderophages is based on the production of hemosiderin, which serves persistent iron storing without later recycling. Therefore, siderophages would be M1-type macrophages. However, recent studies report the plasticity of macrophages, which were already polarized into M1 or M2. This change of phenotypes was attributed to environmental cues, such as angiogenic factors (Mantovani & Locati, 2016). Therefore, the macrophage subtype of siderophages in the course of cardiac fibrosis cannot be inferred from the main source of their formation, but requires further validation.

In summary, the investigations on siderophages as marker of previous haemorrhage point to their connection to the formation of fibrosis. In accordance with the markers of vascular damage in this thesis, the results obtained on the formation of siderophages suggest ongoing remodelling of myocardium into scar tissue. In addition, the presented results confirm, that the occurrence of vascular damage did not only depend on the applied dose, but also on the irradiated volume.

4.4. Cell Death and Inflammatory Burden

High dosed target irradiation was shown to induce vascular damage like haemorrhage and loss of microvessels, which are considered an initial event of tissue remodelling. As a consequence of these processes, necrosis can occur in the affected tissue due to malnourishment and inflammatory reactions can be triggered in turn (Baldi et al., 2002; Bolick, Hackel, Reimer, & Ideker, 1986; Newby, 2004; Prech et al., 2010; Vigliano et al., 2011; Virag & Murry, 2003). The detection of cytokines as inflammatory markers in the PF and serum was performed to assess the risk of cardiovascular events due to a pro–inflammatory environment and subsequent development of cardiovascular diseases (Gonzalez et al., 2009; Kemp et al., 2004; Newby, 2004; Wynn, 2004). In addition, morphological analyses were complemented with the detection of soluble markers of necrosis and inflammation were analysed in PF six months after irradiation.

As a marker of the necrosis of several cell types, HMGB1 was used (Karuppagounder et al., 2016; Lin et al., 2015). In addition, the release of troponin T, indicative of cardiomyocyte necrosis (Gonzalez et al., 2009; Kemp et al., 2004; Newby, 2004), and von Willebrand factor (vWF), revealing necrosis of EC (Boerma et al., 2004; Kleef et al., 2000), were measured. Furthermore, the release of several cytokines was detected to investigate, if pro-inflammatory reactions were still ongoing (first stage of cardiac fibrosis) or if they were regulated and pro-fibrotic signalling was taking over (second stage of cardiac fibrosis).

Troponin T concentrations were elevated only after LV irradiation (Figure 41). However, the release of other necrotic markers was not changed after irradiation (Appendix, Figure 62). In addition, an increased concentration of TNFα, IL-8 and IL-10 was detected after LV irradiation (Figure 42 and Figure 43). After AVN irradiation, only the CRP concentration was elevated after the exposure to the highest dose (55 Gy, Figure 42). The release of other tested factors remained unchanged after irradiation of both targets (Appendix, Figure 64, Figure 66, and Figure 67).

4.4.1. Connection between the Detection of Necrosis and the Affected Volume

Among the investigated markers of necrosis, only troponin T concentrations were elevated after the irradiation of the largest target volume (LV 1.5 cm^3 compared to AVN 1 cm^3). However, cell death of several cell types is a well-known effect of irradiation (Hall & Giaccia, 2006; Washington et al., 2013). Consequently, these discrepancies are discussed in the following peragraphs.

The absence of changes in the release of HMBG1 as a general marker of necrosis was not in line with the detection of troponin T, a marker of necrosis in cardiomyocytes. This challenges the sensitivity of the HMGB1 detection. Therefore, this method should not be further employed for this approach.

The absence of any changes in vWF release in PF indicates that no endothelial necrosis was present at six months after irradiation. This would mean that the occurrence of bleeding and loss of microvessels (Figure 24, Figure 26, Figure 29, Figure 30, Figure 35, and Figure 36) was not related to necrosis. This interrelation seems unlikely to be true. In accordance with this doubt, an increased release of vWF in cell culture supernatants was detected 66 h after 20 Gy X-irradiation of EC culture systems. In addition, the accumulation of vWF in EC culture systems and also higher concentrations of vWF in serum was reported 12 to 40 weeks after 15 to 20 Gy X-irradiation of whole organs (kidney and heart) (Boerma et al., 2004; Kleef et al., 2000). Therefore, the sensitivity of the vWF detection is also challenged and should not be further employed for this approach.

Only the concentrations of troponin T were elevated after high dosed irradiation of the largest target volume (LV). However, the occurrence of cell death only after the treatment of the largest target volume does not seem convincing. Therefore, the difference between the results of the presented thesis to other sources could be based on the irradiated volumes, which might be too small to detect these changes in the presented project. Consequently, necrosis was only detectable in PF, if the damaged tissue area was large enough.

4.4.2. No Increased Risk for Cardiovascular Events

In clinical routine, only serum (and not PF) is used for the analysis of necrotic and inflammatory markers: The detection of troponin T is the gold standard for diagnosis of MI in patients and a marker of myocardial necrosis due to hypoxia. Increased levels of troponin T are associated with mortality within one year and predicts future risk of MI (Kemp et al., 2004; Newby, 2004). Similarly, elevated serum levels of IL-6 and CRP are also linked to mortality within one year after MI (Newby, 2004). The unchanged serum concentrations of troponin T, IL-6 and CRP in the presented study, suggest the absence of an increased risk for cardiovascular events after LV and AVN irradiation.

4.4.3. Parallel Occurrence of Several Stages of Cardiac Fibrosis and No Systemic Inflammation

The increased levels of inflammatory markers only in the PF demonstrate that inflammatory reactions were limited to cardiac tissue. The detection of pro- and anti-inflammatory mediators at six months after irradiation indicates a parallel occurrence of the first and second stage of cardiac fibrosis: Although inflammation was still ongoing in certain areas (first stage of cardiac fibrosis), it was also regulated due to the manifestation of other processes like the activation of myofibroblasts (second stage of cardiac fibrosis). These findings are line with the histological results of the presented thesis.

As inflammation was only found within the irradiated areas, the cell types contributing to the elevated levels of cytokines are most likely localized in irradiated tissue. However, these cell types could not be defined. Taken together, these investigations show that inflammation was restricted to irradiated cardiac tissue and does not entail risks for future cardiovascular events.

4.4.4. Alternative Stainings for Cell Death and their Prospects

In this work, typical immuno-histological markers of the detection of cell death like apoptosis and necrosis were applied in tissue. In detail, cleaved caspase 3 and TUNEL staining serve as markers of apoptosis and complement factor 9 for oncosis, which is considered a cardiac variation of necrosis (Vigliano et al., 2011). These staining protocols were not reliable due to the unspecific binding of antibodies. Activated caspase 3, indicating apoptosis, was solely detected in protein extracts of irradiated cardiac tissue (Lehmann et al., 2016). However, this method is not suited to detect the cell types undergoing apoptosis. Successful labelling with specific antibodies against ubiquitin or beclin-1 in tissue sections would have allowed investigation of autophagy as detected in other studies after vascular damage in cardiac tissue. Its occurrence is linked to the restoration of cellular and tissue homoeostasis (Lekli, Haines, Balla, & Tosaki, 2016; Vigliano et al., 2011). As the histological detection of cell death was not successful, soluble necrotic markers were investigated in the PF and serum.

4.5. Effects in Non-Targeted Tissue

The spreading of fibrosis to outfield regions is described as a hallmark of fibrotic lesion formation. These observations were obtained for fibrosis due to age, irradiation or MI. Moreover, it always appeared as a longterm effect (Adams et al., 2003; Biernacka & Frangogiannis, 2011; Talman & Ruskoaho, 2016). If there were any indications for this process in the investigated time frame of the presented thesis, it would be a limiting factor for the application of the treatment. Consequently, hints for tissue remodelling in outfield regions were systematically investigated.

4.5.1. Damage in the IVS Contributes to the Ablation of the AVN

In this thesis, the interventricular septum (IVS) was the only outfield region, where damage was induced. The reason for this observation might be that the IVS is in close vicinity to AVN targets and was presumably accidentally irradiated (personal communication with A. Eichhorn and C. Graeff). Macroscopic scar formation indicated that at least 1 cm^3 of IVS tissue, which resembles 30 % to 50 % of the investigated volume of this sample, was irradiated with high doses (data not shown). The detection of different tissue reactions in the IVS confirmed this assumption (Figure 29, Figure 32, Figure 35, and Figure 38). Moreover, these findings confirmed that the other outfield regions were not exposed to carbon ion irradiation.

The manifestation of several tissue responses particularly in the IVS of the animal with persistent AV block (Pig F) points to a connection between the abrogation of electrical signalling and tissue remodelling in both, target and IVS areas. Similarly, catheter ablation of arrhythmogenic substrates is also based on the lesion formation in several locations around the substrate. This approach ensures a higher efficacy of the treatment (Calkins et al., 2012). These data validate that the irradiation of the IVS and that subsequent tissue remodelling contributes to the ablation of the AVN. Therefore, the absence of damage in the IVS of other animals might be the reason that no other animal developed a persistent AV block.

4.5.2. No Spreading of the Damage within the Investigated Period of Time

In contrast to the results for the IVS, no indications for tissue remodelling were observed in other outfield regions (Table 17, Table 18, Table 19, and Table 20, Figure 60). However, these results are not in line with other sources, where propagation of tissue remodelling to outfield regions was detected after vascular damage (Baldi et al., 2002; Biernacka & Frangogiannis, 2011; Dusek et al., 1971; Talman & Ruskoaho, 2016; Virag & Murry, 2003).

In contrast to these studies and in accordance with the results of the presented thesis, Fajardo and Stewart showed that irradiation of a portion of the heart does not lead to lesion formation in unirradiated areas or interfere with lesion formation in irradiated areas (Fajardo & Stewart, 1970). These findings are also confirmed by other studies, which investigated cardiac ablation with 20 – 100 Gy β- and X-irradiation in canine and porcine models. In these studies, the well-demarcated lesions were only found in target areas until one to six months after irradiation (Bode et al., 2015; Franceschi et al., 2012; Guerra et al., 2004; Sharma et al., 2010).

As described in literature, the spreading of fibrosis is caused by mechanical stress due to the stiffening of the damaged tissue and soluble factors from lesion areas such as IL-6 (pro–inflammatory cytokine), TGF-β (pro–fibrotic cytokine) and Ang II (factor for myofibroblast transdifferentiation and proliferation) (Biernacka & Frangogiannis, 2011; Dusek et al., 1971; Talman & Ruskoaho, 2016). Although the propagation of damage did not occur in the investigated time frames, investigations in patients suffering from radiation–induced heart diseases (RIHD) demonstrated that the expansion of fibrotic tissue manifests over decades (Adams et al., 2003; Heidenreich & Kapoor, 2009; Schultz-Hector & Trott, 2007; Taunk et al., 2015; Wynn, 2004). Therefore, the expansion of fibrosis might also occur at some point after the irradiation procedure applied in the presented project.

4.6. Summary and Outlook

The focus of this thesis was the investigation of vascular damage in cardiac tissue as an initial event of tissue remodelling after the exposure of small volumes to carbon ion irradiation. The results revealed persistent tissue remodelling marked by haemorrhage, inflammation, and loss of microvessels. These tissue responses were accompanied by the occurrence of siderophages, which indicate prior haemorrhage. For the first time, these changes were systematically investigated in scar tissue and myocardium. The results demonstrate that scar formation in target areas was not completed and will spread further. The investigations of this thesis also showed that fibrotic processes were induced in the entrance channel regions, too. However, they progressed comparably slowly indicating their manifestation as scar tissue over a longer period of time. Furthermore, irradiation-induced histological changes were put into context with soluble markers of necrosis and inflammation. They indicated that cell death and inflammation were restricted to irradiated cardiac tissue.

As one major limitation of this study was the small number of available animals, the investigated tissue reactions and subsequently postulated hypotheses require further validation. In addition, the small number of available animals did not allow for the identification of inter-individual differences, such as different sensitivities or time frames for the development of fibrosis. Another limitation of this thesis was the lack of a direct proof for the connection between tissue remodelling and ablation of cardiac tissue. The only exception was the parallel appearance of damage in the AVN target and the IVS, which was associated with a persistent AV block. However, the link between the development of cardiac fibrosis and an impaired function is established in literature (Adams et al., 2003; Biernacka & Frangogiannis, 2011; Fajardo & Stewart, 1971; Schultz-Hector & Trott, 2007; Talman & Ruskoaho, 2016).

Comprehensively, this thesis provides evidentiary proof on ongoing tissue remodelling after the unique approach of cardiac ablation with high dosed carbon ion irradiation until at least six months after irradiation.
Moreover, the findings of this thesis on vascular damage can be complemented with the analyses of further implications of vascular damage, maturation of scar tissue and investigations on the functionality of the cardiac conduction system:

a. Vascular damage was described to cause ischemia and subsequently reduced oxygen and nutrition supply. In addition, the results of this thesis demonstrated the loss of microvessels probably leading to hypoxic conditions. One common marker of hypoxia is HIF-1α. However, the association of HIF-1α with fibrosis is not clear (Cai, Luo, Zhan, & Semenza, 2013; Talman & Ruskoaho, 2016). Moreover, the expression of HIF-1α in epicardium and subepicardium is associated with the microenvironment of cardiomyocyte progenitor cells (Kocabas et al., 2012) rendering HIF-1α not as definite marker of irradiation-induced hypoxia. The standard method to investigate hypoxia in cardiac tissue relies on the detection of EF5 or pimonidazole. However, these markers need to be administered before the sacrifice. Therefore, the link between vascular damage and hypoxia are more feasibly realizable in upcoming animal experiments after the application of EF5 or pimonidazole.

b. The death of cardiomyocytes can have different appearances: Coagulation necrosis and contraction band necrosis are both basic types of ischemic myocardial necrosis and present with loss of structural proteins (desmin and myoglobin) and sarcomeres (Brinkmann, Sepulchre, & Fechner, 1993; Virag & Murry, 2003; Washington et al., 2013). Furthermore, the appearance of cell death at several time points gives indications for the progression of tissue remodelling. However, the occurrence of cell death was probably more frequently observable before the comparably late investigated time points of this project. Therefore, the investigation of earlier time points might give hints on the progression of scar formation. In addition, the histological identification of apoptosis, necrosis and autophagy will complement the investigations of necrotic markers of the presented work.

c. Aside from the occurrence of early tissue responses, the formation of a fibrous scar requires the activation of different cell types (Biernacka & Frangogiannis, 2011; Ghobadi et al., 2012; Talman & Ruskoaho, 2016). The identification of contributing cell types undergoing phenotypic transition into myofibroblasts is conversely discussed. The putatively involved cell types ranges from fibroblasts and macrophages to the further involvement of EC, SMC and Gli1+ mesenchymal stem-cell-like cells (Biernacka & Frangogiannis, 2011; Talman & Ruskoaho, 2016; Wynn, 2004). In addition, the role of senescence in myofibroblasts is discussed to restrict infarct areas (Meyer et al., 2016). Fate mapping of different cell types into myofibroblasts would give further insights on fibrogenic mechanisms.

d. Hypertrophy of cardiomyocytes is described as a typical feature of surviving cardiomyocytes after ischemia. They were observed in parallel to atrophic cardiomyocytes in areas of increased collagen deposition (Biernacka & Frangogiannis, 2011; Dusek et al., 1971; Prech et al., 2010; Talman & Ruskoaho, 2016; Vigliano et al., 2011). Dusek et al. suggested an increased energy metabolism as cause for the hypertrophy of cardiomyocytes and, as results of metabolic exhaustion, atrophy of cardiomyocytes in parallel to later stages of cardiac fibrosis (Dusek et al., 1971). As the parallel occurrence of enlarged and shrunk cardiomyocytes was also obtained in target areas of the presented project, the status of energy metabolism might give insights on the faith of irradiated cardiomyocytes.

e. The onset of fibrosis can differ widely among patients, who underwent radiotherapy. Similarly, the animals in this project also displayed inter-individually heterogenic results concerning the development of fibrosis. Investigations on DNA methylation might reveal, if epigenetic regulation was the cause for these responses. The methylation of diacylglycerol kinase alpha (DGKA) was shown to interfere with the pro-fibrotic transcription factor EGR1. Consequently, the inhibition of DGKA lead to a decreased pro-fibrotic activation of fibroblasts (Weigel et al., 2016). Therefore, DNA methylation profiling could be applied to predict the radiation response of animals and later also on patients.

f. The interruption of conductivity in myocardium can also be achieved by other processes than fibrosis: Cardiomyocytes are connected to fibroblasts, neurons, and to each other by connexin (cx) 40, cx43 and cx45 (Talman & Ruskoaho, 2016). Carbon ion irradiation (15 Gy) of LV after experimentally induced MI was shown to interfere with the conduction of electrical signals in rabbits (Amino et al., 2010). Therefore, the blockage of impulse propagation could be assessed investigating gap junction proteins, ion channel regions etc. between cardiomyocytes and other cell types. Furthermore, the functionality of neurons in the myocardium could be evaluated analysing for example the maintenance of the myelin sheath.

5. Bibliography

Adams, M. J., Hardenbergh, P. H., Constine, L. S., & Lipshultz, S. E. (2003). Radiation-associated cardiovascular disease. *Critical Reviews in Oncology/Hematology*, *45*(1), 55–75. https://doi.org/10.1016/S1040-8428(01)00227-X

Amino, M., Yoshioka, K., Fujibayashi, D., Hashida, T., Furusawa, Y., Zareba, W., … Tanabe, T. (2010). Year-long upregulation of connexin43 in rabbit hearts by heavy ion irradiation. *American Journal of Physiology. Heart and Circulatory Physiology*, *298*(3), H1014–H1021. https://doi.org/10.1152/ajpheart.00160.2009

Atkins, P. W. (Peter W. (2010). *Atkins' physical chemistry / Peter Atkins, Julio de Paula. Physical chemistry*.

Baldi, A., Abbate, A., Bussani, R., Patti, G., Melfi, R., Angelini, A., … Di Sciascio, G. (2002). Apoptosis and post-infarction left ventricular remodeling. *Journal of Molecular and Cellular Cardiology*, *34*(2), 165–174. https://doi.org/10.1006/jmcc.2001.1498

Behrends, J., Bischofberger, J., & Deutzmann, R. (2012). *Duale Reihe Physiologie*. *The American journal of clinical nutrition* (Vol. 86). https://doi.org/10.1055/b-002-23567

Bergeron, M., Evans, S. M., Sharp, F. R., Koch, C. J., Lord, E. M., & Ferriero, D. M. (1999). Detection of hypoxic cells with the 2-nitroimidazole, EF5, correlates with early redox changes in rat brain after perinatal hypoxia-ischemia. *Neuroscience*, *89*(4), 1357–66. Retrieved from http://www.ncbi.nlm.nih.gov/pubmed/10362320

Bert, C., & Durante, M. (2011). Motion in radiotherapy: particle therapy. *Physics in Medicine and Biology*, *56*(16), R113–R144. https://doi.org/10.1088/0031-9155/56/16/R01

Bert, C., Grozinger, S. O., & Rietzel, E. (2008). Quantification of interplay effects of scanned particle beams and moving targets. *Phys Med Biol*, *53*(9), 2253–2265. https://doi.org/10.1088/0031-9155/53/9/003

Bi, H., Yang, Y., Huang, J., Li, Y., Ma, C., & Cong, B. (2013). Immunohistochemical detection of S100A1 in the postmortem diagnosis of acute myocardial infarction. *Diagnostic Pathology*, *8*(1), 84. https://doi.org/10.1186/1746-1596-8-84

Biernacka, A., & Frangogiannis, N. G. (2011). Aging and Cardiac Fibrosis. *Aging and Disease*, *2*(2), 158–173. https://doi.org/10.1016/j.bbi.2008.05.010

Bode, F., Blanck, O., Gebhard, M., Hunold, P., Grossherr, M., Brandt, S., … Rades, D. (2015). Pulmonary vein isolation by radiosurgery: Implications for non-invasive treatment of atrial fibrillation. *Europace*, *17*(12), 1868–1874. https://doi.org/10.1093/europace/euu406

Boerma, M., Kruse, J. J. C. M., Van Loenen, M. M., Klein, H. R., Bart, C. I., Zurcher, C., & Wondergem, J. (2004). Increased Deposition of von Willebrand Factor in the Rat Heart after Local Ionizing Irradiation. *Strahlentherapie Und Onkologie*, *180*(2), 109–116. https://doi.org/10.1007/s00066-004-1138-0

Bolick, D. R., Hackel, D. B., Reimer, K. A., & Ideker, R. E. (1986). Quantitative analysis of myocardial infarct structure in patients with ventricular tachycardia. *Circulation*, *74*(6), 1266–1279. https://doi.org/10.1161/01.CIR.74.6.1266

Brinkmann, B., Sepulchre, M. A., & Fechner, G. (1993). The application of selected histochemical and immunohistochemical markers and procedures to the diagnosis of early myocardial damage. *International Journal of Legal Medicine*, *106*(3), 135–141. https://doi.org/10.1007/BF01225234

Britannica, E. (2006). Britannica Concise Encyclopedia. *Nature*. https://doi.org/10.1108/09504120310503656

Cai, Z., Luo, W., Zhan, H., & Semenza, G. L. (2013). Hypoxia-inducible factor 1 is required for remote ischemic preconditioning of the heart. *Pnas*, *110*(43), 17462–17467. https://doi.org/10.1073/pnas.1317158110/-

/DCSupplemental.www.pnas.org/cgi/doi/10.1073/pnas.1317158110

Calkins, H., Kuck, K. H., Cappato, R., Brugada, J., John Camm, A., Chen, S. A., … Wilber, D. (2012). 2012 HRS/EHRA/ECAS expert consensus statement on catheter and surgical ablation of atrial fibrillation: Recommendations for patient selection, procedural techniques, patient management and follow-up, definitions, endpoints, and research trial design. *Journal of Interventional Cardiac Electrophysiology*, *33*(2), 171–257. https://doi.org/10.1007/s10840-012-9672-7

Cervelli, T., Panetta, D., Navarra, T., Andreassi, M. G., Basta, G., Galli, A., … Del Turco, S. (2014). Effects of single and fractionated low-dose irradiation on vascular endothelial cells. *Atherosclerosis*, *235*(2), 510–518. https://doi.org/10.1016/j.atherosclerosis.2014.05.932

Chen, F.-H., Chiang, C.-S., Wang, C.-C., Tsai, C.-S., Jung, S.-M., Lee, C.-C., … Hong, J.-H. (2009). Radiotherapy Decreases Vascular Density and Causes Hypoxia with Macrophage Aggregation in TRAMP-C1 Prostate Tumors. *Clinical Cancer Research*, *15*(5), 1721–1729. https://doi.org/10.1158/1078-0432.CCR-08-1471

Chrastina, A., Pokreisz, P., & Schnitzer, J. E. (2014). Experimental model of transthoracic, vascular-targeted, photodynamically induced myocardial infarction. *American Journal of Physiology - Heart & Circulatory Physiology*, *306*(2), H270-8. https://doi.org/http://dx.doi.org/10.1152/ajpheart.00818.2012

Chugh, S. S., Havmoeller, R., Narayanan, K., Singh, D., Rienstra, M., Benjamin, E. J., … Murray, C. J. L. (2014). Worldwide epidemiology of atrial fibrillation: A global burden of disease 2010 study. *Circulation*, *129*(8), 837–847. https://doi.org/10.1161/CIRCULATIONAHA.113.005119

Crick, S. J., Sheppard, M. N., Ho, S. Y., & Anderson, R. H. (1999). Localisation and quantitation of autonomic innervation in the porcine heart I: conduction system. *J Anat*, *195 (Pt 3*, 341–357. https://doi.org/10.1046/j.1469-7580.1999.19530359.x

Demtröder, W. (1997). Experimentalphysik 3, Atome, Moleküle und Festkörper. *Zeitschrift Für Physikalische Chemie*. https://doi.org/10.1524/zpch.1997.200.Part_1_2.278

Dettmering, T. (2013). *Effects of carbon ion irradiation on inflammatory processes and normal tissue damage in the endothelium and the rat lung*.

Dusek, J., Rona, G., & Kahn, D. S. (1971). Healing process in the marginal zone of an experimental myocardial infarct. Findings in the surviving cardiac muscle cells. *The American Journal of Pathology*, *62*(3), 321–38. Retrieved from http://www.pubmedcentral.nih.gov/articlerender.fcgi?artid=2047415&tool=pmcentrez&rendertype=abstract

Eichhorn, A. V. (2016). *In-Vivo Feasibility Study and Developments for Cardiac Arrhythmia Ablation using Scanned Carbon Ions*.

Elsässer, T., Gemmel, A., Scholz, M., Schardt, D., & Krämer, M. (2009). The relevance of very low energy ions for heavy-ion therapy. *Physics in Medicine and Biology*, *54*(7), N101–N106. https://doi.org/10.1088/0031-9155/54/7/N03

Elsässer, T., Weyrather, W. K., Friedrich, T., Durante, M., Iancu, G., Krämer, M., … Scholz, M. (2010). Quantification of the relative biological effectiveness for ion beam radiotherapy: Direct experimental comparison of proton and carbon ion beams and a novel approach for treatment planning. *International Journal of Radiation Oncology Biology Physics*, *78*(4), 1177–1183. https://doi.org/10.1016/j.ijrobp.2010.05.014

Erbeldinger, N., Merz, F., Simoniello, P., Lehmann, H. I., Lugenbiel, P., Eichhorn, A., … Fournier, C. (2015). Vascular and fibrotic changes in irradiated myocard after cardiac ablation with carbon ions in a pig model. *GSI Scientific Report*, 1657.

Fajardo, L. F., & Stewart, J. R. (1970). Experimental radiation-induced heart disease. I. Light microscopic studies. *The American Journal of Pathology*, *59*(2), 299–316.

Fajardo, L. F., & Stewart, J. R. (1971). Capillary injury preceding radiation-induced myocardial fibrosis. *Radiology*, *101*(2), 429–433. https://doi.org/10.1148/101.2.429

Fisher, M., French, S., Ji, P., & Kim, R. C. (2010). Cerebral microbleeds in the elderly: A pathological analysis. *Stroke*, *41*(12), 2782–2785. https://doi.org/10.1161/STROKEAHA.110.593657

Franceschi, F., Bonan, R., Khairy, P., Dubuc, M., Thibault, B., MacLe, L., … Guerra, P. G. (2012). Histopathological effects and evolution of transvenous ??-radiation applications in right and left atria: An animal study. *Europace*, *14*(5), 745–751. https://doi.org/10.1093/europace/eur351

Gemmel, A., Rietzel, E., Kraft, G., Durante, M., & Bert, C. (2011). Calculation and experimental verification of the RBE-weighted dose for scanned ion beams in the presence of target motion. *Physics in Medicine and Biology*, *56*(23), 7337–7351. https://doi.org/10.1088/0031-9155/56/23/001

Ghobadi, G., Bartelds, B., van der Veen, S. J., Dickinson, M. G., Brandenburg, S., Berger, R. M. F., … van Luijk, P. (2012). Lung irradiation induces pulmonary vascular remodelling resembling pulmonary arterial hypertension. *Thorax*, *67*(4), 334–341. https://doi.org/10.1136/thoraxjnl-2011-200346

Gonzalez, A., Lopez, B., Ravassa, S., Beaumont, J., Arias, T., Hermida, N., … Diez, J. (2009). Biochemical markers of myocardial remodelling in hypertensive heart disease. *Cardiovascular Research*. https://doi.org/10.1093/cvr/cvn235

Grözinger, S. O., Rietzel, E., Li, Q., Bert, C., Haberer, T., & Kraft, G. (2006). Simulations to design an online motion compensation system for scanned particle beams. *Physics in Medicine and Biology*, *51*(14), 3517–3531. https://doi.org/10.1088/0031-9155/51/14/016

Guerra, P. G., Talajic, M., Thibault, B., Dubuc, M., Roy, D., Made, L., … Bonan, R. (2004). beta-radiation for the creation of linear lesions in the canine atrium. *Circulation*, *110*(8), 911–914. https://doi.org/10.1161/01.CIR.0000139865.39885.03

Gyenes, G., Rutqvist, L. E., Liedberg, A., & Fornander, T. (1998). Long-term cardiac morbidity and mortality in a randomized trial of pre- and postoperative radiation therapy versus surgery alone in primary breast cancer. *Radiotherapy and Oncology : Journal of the European Society for Therapeutic Radiology and Oncology*, *48*(2), 185–190. https://doi.org/10.1016/S0167-8140(98)00062-0

Hall, E. J., & Giaccia, A. J. (2006). *Radiobiology for the Radiologist, 6th ed., by Eric J. Hall and Amato J. Giaccia*. *Radiation Research* (Vol. 166). https://doi.org/10.1667/RR0771.1

Heidenreich, P. A., & Kapoor, J. R. (2009). Radiation induced heart disease. *Education in Heart*, *95*, 252–258. https://doi.org/10.1136/hrt.2008.149088

Hopewell, J. W., Campling, D., Calvo, W., Reinhold, H. S., Wilkinson, J. H., & Yeung, T. K. (1986). Vascular irradiation damage: its cellular basis and likely consequences. *The British Journal of Cancer. Supplement*, 181–191.

Iliakis, G. (1991). The role of DNA double strand breaks in ionizing radiation-induced killing of eukaryotic cells. *BioEssays : News and Reviews in Molecular, Cellular and Developmental Biology*, *13*(12), 641–8. https://doi.org/10.1002/bies.950131204

Jakubzick, C., Choi, E. S., Joshi, B. H., Keane, M. P., Kunkel, S. L., Puri, R. K., & Hogaboam, C. M. (2003). Therapeutic attenuation of pulmonary fibrosis via targeting of IL-4- and IL-13-responsive cells. *Journal of Immunology (Baltimore, Md. : 1950)*, *171*(5), 2684–93. https://doi.org/10.4049/jimmunol.171.5.2684

Kaderka, R., Schardt, D., Durante, M., Berger, T., Ramm, U., Licher, J., & Tessa, C. La. (2012). Out-of-field dose measurements in a water phantom using different radiotherapy modalities. *Physics in Medicine and Biology*, *57*(16), 5059–5074.

https://doi.org/10.1088/0031-9155/57/16/5059

Karger, C. P., Peschke, P., Sanchez-Brandelik, R., Scholz, M., & Debus, J. (2006). Radiation tolerance of the rat spinal cord after 6 and 18 fractions of photons and carbon ions: Experimental results and clinical implications. *International Journal of Radiation Oncology*Biology*Physics*, *66*(5), 1488–1497. https://doi.org/10.1016/j.ijrobp.2006.08.045

Karuppagounder, V., Giridharan, V. V., Arumugam, S., Sreedhar, R., Palaniyandi, S. S., Krishnamurthy, P., … Thandavarayan, R. A. (2016). Modulation of Macrophage Polarization and HMGB1-TLR2/TLR4 Cascade Plays a Crucial Role for Cardiac Remodeling in Senescence-Accelerated Prone Mice. *PLoS ONE*, *11*(4), 1–11. https://doi.org/10.1371/journal.pone.0152922

Kemp, M., Donovan, J., Higham, H., & Hooper, J. (2004). Biochemical markers of myocardial injury, *93*(1). https://doi.org/10.1093/bja/aeh148

Kiscsatári, L., Sárközy, M., Kővári, B., Varga, Z., Gömöri, K., Morvay, N., … Kahán, Z. (2016). High-dose Radiation Induced Heart Damage in a Rat Model. *In Vivo (Athens, Greece)*, *30*(5), 623–31. Retrieved from http://www.ncbi.nlm.nih.gov/pubmed/27566082

Kleef, E. Van, Verheij, M., Poele, H., Oussoren, Y., Dewit, L., & Stewart, F. (2000). In Vitro and In Vivo Expression of Endothelial von Willebrand Factor and Leukocyte Accumulation after Fractionated Irradiation In Vitro and In Vivo Expression of Endothelial von Willebrand Factor and Leukocyte Accumulation after Fractionated Irradiation, *154*(4), 375–381. https://doi.org/10.1667/0033-7587(2000)154

Kocabas, F., Mahmoud, A. I., Sosic, D., Porrello, E. R., Chen, R., Garcia, J. A., … Sadek, H. A. (2012). The hypoxic epicardial and subepicardial microenvironment. *Journal of Cardiovascular Translational Research*, *5*(5), 654–665. https://doi.org/10.1007/s12265-012-9366-7

Kraft, G. (2000). Tumor therapy with heavy charged particles. *Progress in Particle and Nuclear Physics*, *45*(Supplement 2), S473--S544. https://doi.org/10.1016/S0146-6410(00)00112-5

Krämer, M. (2009). Swift ions in radiotherapy - Treatment planning with TRiP98. *Nuclear Instruments and Methods in Physics Research, Section B: Beam Interactions with Materials and Atoms*, *267*(6), 989–992. https://doi.org/10.1016/j.nimb.2009.02.015

Krämer, M., Weyrather, W. K., & Scholz, M. (2003). The increased biological effectiveness of heavy charged particles: from radiobiology to treatment planning. *Technology in Cancer Research & Treatment*, *2*(5), 427–436.

Lederer, H., Muggli, B., Speich, R., Treder, U., Stricker, H., Goede, J., … Breitenstein, A. (2014). Haemosiderin-laden sputum macrophages for diagnosis in pulmonary veno-occlusive disease. *PLoS ONE*, *9*(12), 1–10. https://doi.org/10.1371/journal.pone.0115219

Lee, J.-W., Bae, S.-H., Jeong, J.-W., Kim, S.-H., & Kim, K.-W. (2004). Hypoxia-inducible factor (HIF-1)α: its protein stability and biological functions. *Experimental & Molecular Medicine*, *36*(1), 1–12. https://doi.org/10.1038/emm.2004.1

Lehmann, H. I., Graeff, C., Durante, M., & Packer, D. (2016). Feasibility Study on Cardiac Arrhythmia Ablation Using High-Energy Heavy Ion Beams. *Scientific Reports*, (August), 1–13. https://doi.org/10.1038/srep38895

Lehmann, H. I., Richter, D., Prokesch, H., Graeff, C., Prall, M., Simoniello, P., … Packer, D. L. (2015). AV Node Ablation in Langendorff-Perfused Porcine Hearts Using Carbon Ion Particle Therapy: Methods and an In vivo Feasibility Investigation for Catheter-Free Ablation of Cardiac Arrhythmias. *Circulation: Arrhythmia and Electrophysiology*, *8*(2), 429–438. https://doi.org/10.1161/CIRCEP.114.002436

Lekli, I., Haines, D. D., Balla, G., & Tosaki, A. (2016). Autophagy: an adaptive physiological countermeasure to cellular senescence and ischaemia/reperfusion-associated cardiac arrhythmias. *Journal of Cellular and Molecular Medicine*. https://doi.org/10.1111/jcmm.13053

Libby, P.; Ridker, P. M.; Hansson, G. K. (2011). Progress and challenges in translating the biology of atherosclerosis. *Nature*, *473*, 317–325. https://doi.org/10.1038/nature10146

Libby, P. (2002). Inflammation in atherosclerosis. *Nature*, *420*(6917), 868–74. https://doi.org/10.1038/nature01323

Lie, J. T., Holley, K. E., Kampa, W. R., & Titus, J. L. (1971). New histochemical method for morphologic diagnosis of early stages of myocardial ischemia. *Mayo Clinic Proceedings*, *46*(5), 319–27. Retrieved from http://www.ncbi.nlm.nih.gov/pubmed/4102906

Lie, J. T., Pairolero, P. C., Holley, K. E., & Titus, J. L. (1975). Macroscopic enzyme-mapping verification of large, homogeneous, experimental myocardial infarcts of predictable size and location in dogs. *The Journal of Thoracic and Cardiovascular Surgery*, *69*(4), 599–605. Retrieved from http://www.ncbi.nlm.nih.gov/pubmed/1117748

Lin, Y., Chen, L., Li, W., & Fang, J. (2015). Role of high-mobility group box-1 in myocardial ischemia/reperfusion injury and the effect of ethyl pyruvate. *Experimental and Therapeutic Medicine*, *9*(4), 1537–1541. https://doi.org/10.3892/etm.2015.2290

Mantovani, A., & Locati, M. (2016). Macrophage Metabolism Shapes Angiogenesis in Tumors. *Cell Metabolism*. https://doi.org/10.1016/j.cmet.2016.10.016

Meyer, K., Hodwin, B., Ramanujam, D., Engelhardt, S., & Sarikas, A. (2016). Essential Role for Premature Senescence of Myofibroblasts in Myocardial Fibrosis. *Journal of the American College of Cardiology*, *67*(17), 2018–2028. https://doi.org/10.1016/j.jacc.2016.02.047

Newby, L. K. (2004). Markers of cardiac ischemia, injury, and inflammation. *Progress in Cardiovascular Diseases*. https://doi.org/10.1016/j.pcad.2003.12.006

Pezzutto, A., Ulrichs, T., & Burmester, G.-R. (2007). *Taschenatlas der Immunologie : Grundlagen, Labor, Klinik*. Thieme.

Ponka, P. (1999). Cellular iron metabolism. *Kidney International. Supplement*, *69*(S69), S2–S11. https://doi.org/10.1046/j.1523-1755.1999.055Suppl.69002.x

Potiron, V. A., Abderrahmani, R., Clément-Colmou, K., Marionneau-Lambot, S., Oullier, T., Paris, F., & Supiot, S. (2013). Improved functionality of the vasculature during conventionally fractionated radiation therapy of prostate cancer. *PloS One*, *8*(12), e84076. https://doi.org/10.1371/journal.pone.0084076

Prech, M., Marszałek, A., Schröder, J., Filas, V., Lesiak, M., Jemielity, M., … Grajek, S. (2010). Apoptosis as a Mechanism for the Elimination of Cardiomyocytes After Acute Myocardial Infarction. *American Journal of Cardiology*, *105*(9), 1240–1245. https://doi.org/10.1016/j.amjcard.2009.12.039

Pusztaszeri, M. P., Seelentag, W., & Bosman, F. T. (2006). Immunohistochemical Expression of Endothelial Markers CD31, CD34, von Willebrand Factor, and Fli-1 in Normal Human Tissues. *Journal of Histochemistry & Cytochemistry*, *54*(4), 385–395. https://doi.org/10.1369/jhc.4A6514.2005

Reece, J., & Urry, L. (2011). *Campbell biology. Campbell Biology*. https://doi.org/10.1039/c3ra44507k

Ricardo, S. D., Van Goor, H., & Eddy, A. A. (2008). Macrophage diversity in renal injury and repair. *Journal of Clinical Investigation*. https://doi.org/10.1172/JCI36150

Richter, D. (2012). Treatment planning for tumors with residual motion in scanned ion beam therapy. *Thesis*.

Rudolf, M., & Kuhlisch, W. (2008). *Biostatistik : eine Einführung für Biowissenschaftler*. Pearson Studium.

Schardt, D., Elsässer, T., & Schulz-Ertner, D. (2010). Heavy-ion tumor therapy: Physical and radiobiological benefits. *Reviews of Modern Physics*. https://doi.org/10.1103/RevModPhys.82.383

Scherer, A. T., & Masi, A. T. (1975). Technical aspects of the Haematoxylin-Basic Fuchsin-picric acid (HBFP) stain applied to skeletal muscle. *The Histochemical Journal*, *7*(4), 335–341. https://doi.org/10.1007/BF01007018

Schmidt, R. F., & Lang, F. (2007). *Physiologie des Menschen : mit Pathophysiologie*. Springer Medizin Verlag Heidelberg.

Schrage, A., Loddenkemper, C., Erben, U., Lauer, U., Hausdorf, G., Jungblut, P. R., … Klugewitz, K. (2008). Murine CD146 is widely expressed on endothelial cells and is recognized by the monoclonal antibody ME-9F1. *Histochemistry and Cell Biology*, *129*(4), 441–51. https://doi.org/10.1007/s00418-008-0379-x

Schultz-Hector, S., & Trott, K. R. (2007). Radiation-induced cardiovascular diseases: Is the epidemiologic evidence compatible with the radiobiologic data? *International Journal of Radiation Oncology Biology Physics*. https://doi.org/10.1016/j.ijrobp.2006.08.071

Seemann, I., Gabriels, K., Visser, N. L., Hoving, S., Te Poele, J. A., Pol, J. F., … Stewart, F. A. (2012). Irradiation induced modest changes in murine cardiac function despite progressive structural damage to the myocardium and microvasculature. *Radiotherapy and Oncology*, *103*(2), 143–150. https://doi.org/10.1016/j.radonc.2011.10.011

Sharma, A., Wong, D., Weidlich, G., Fogarty, T., Jack, A., Sumanaweera, T., & Maguire, P. (2010). Noninvasive stereotactic radiosurgery (CyberHeart) for creation of ablation lesions in the atrium. *Heart Rhythm*, *7*(6), 802–810. https://doi.org/10.1016/j.hrthm.2010.02.010

Shirota, M., Kawashima, J., Nakamura, T., Ogawa, Y., Kamiie, J., & Shirota, K. (2013). Vascular Hamartoma in the Uterus of a Female Sprague-Dawley Rat with an Episode of Vaginal Bleeding. *Toxicologic Pathology*, *41*(7), 1011–1015. https://doi.org/10.1177/0192623313476575

Strickberger, S. a, Tokano, T., Kluiwstra, J. U., Morady, F., & Cain, C. (1999). Extracardiac ablation of the canine atrioventricular junction by use of high-intensity focused ultrasound. *Circulation*, *100*(2), 203–8. https://doi.org/10.1161/01.CIR.100.2.203

Talman, V., & Ruskoaho, H. (2016). Cardiac fibrosis in myocardial infarction-from repair and remodeling to regeneration. *Cell and Tissue Research*. https://doi.org/10.1007/s00441-016-2431-9

Tam, S. Y., Wu, V. W. C., & Law, H. K. W. (2017). Influence of autophagy on the efficacy of radiotherapy. *Radiation Oncology*, *12*(1), 57. https://doi.org/10.1186/s13014-017-0795-y

Taunk, N. K., Haffty, B. G., Kostis, J. B., & Goyal, S. (2015). Radiation-induced heart disease: pathologic abnormalities and putative mechanisms. *Frontiers in Oncology*, *5*, 39. https://doi.org/10.3389/fonc.2015.00039

Uchida, Y., Uchida, Y., Maezawa, Y., Maezawa, Y., & Tabata, T. (2012). Migration of mononuclear cells expressing β-actin through the adventitia into media and intima in coronary arteriogenesis and venogenesis in ischemic myocardium. *International Heart Journal*, *53*(1), 54–63. https://doi.org/10.1536/ihj.53.54

Ungvari, Z., Podlutsky, A., Sosnowska, D., Tucsek, Z., Toth, P., Deak, F., … Sonntag, W. E. (2013). Ionizing radiation promotes the acquisition of a senescence-associated secretory phenotype and impairs angiogenic capacity in cerebromicrovascular endothelial cells: Role of increased dna damage and decreased dna repair capacity in microvascular radiosens. *Journals of Gerontology - Series A Biological Sciences and Medical Sciences*, *68*(12 A), 1443–1457. https://doi.org/10.1093/gerona/glt057

Varia, M. A., Calkins-Adams, D. P., Rinker, L. H., Kennedy, A. S., Novotny, D. B., Fowler, W. C., & Raleigh, J. A. (1998). Pimonidazole: A Novel Hypoxia Marker for

Complementary Study of Tumor Hypoxia and Cell Proliferation in Cervical Carcinoma. *Gynecologic Oncology*, *71*(2), 270–277. https://doi.org/10.1006/gyno.1998.5163

Verdino, R. J. (2015). Untreated atrial fibrillation in the United States of America: Understanding the barriers and treatment options. *Journal of the Saudi Heart Association*. https://doi.org/10.1016/j.jsha.2014.09.003

Vigliano, C. A., Cabeza Meckert, P. M., Diez, M., Favaloro, L. E., Cortés, C., Fazzi, L., … Laguens, R. P. (2011). Cardiomyocyte hypertrophy, oncosis, and autophagic vacuolization predict mortality in idiopathic dilated cardiomyopathy with advanced heart failure. *Journal of the American College of Cardiology*, *57*(14), 1523–1531. https://doi.org/10.1016/j.jacc.2010.09.080

Virag, J. I., & Murry, C. E. (2003). Myofibroblast and endothelial cell proliferation during murine myocardial infarct repair. *The American Journal of Pathology*, *163*(6), 2433–40. https://doi.org/10.1016/S0002-9440(10)63598-5

Washington, I., Jeffords, L. B., Rodrigues, R. C., Ma, Y., & Das, S. (2013). NIH Public Access, *5*(234). https://doi.org/10.1126/scisignal.2002918.p53

Weigel, C., Veldwijk, M. R., Oakes, C. C., Seibold, P., Slynko, A., Liesenfeld, D. B., … Popanda, O. (2016). Epigenetic regulation of diacylglycerol kinase alpha promotes radiation-induced fibrosis. *Nature Communications*, *7*, 10893. https://doi.org/10.1038/ncomms10893

Welsch, U., & Mulisch, M. (2010). Romeis Mikroskopische Technik. *Springer Spektrum*, 551. https://doi.org/10.1128/AAC.03728-14

Wondergem, J., Boerma, M., Kodama, K., Stewart, F. A., & Trott, K. R. (2013). Cardiovascular effects after low-dose exposure and radiotherapy: What research is needed? *Radiation and Environmental Biophysics*, *52*(4), 425–434. https://doi.org/10.1007/s00411-013-0489-2

Wynn, T. a. (2004). Fibrotic disease and the T(H)1/T(H)2 paradigm. *Nature Reviews. Immunology*, *4*(8), 583–594. https://doi.org/10.1038/nri1412

Yan, X., Sasi, S. P., Gee, H., Lee, J., Yang, Y., Mehrzad, R., … Kirchmair, R. (2014). Cardiovascular Risks Associated with Low Dose Ionizing Particle Radiation. https://doi.org/10.1371/journal.pone.0110269

6. Appendix

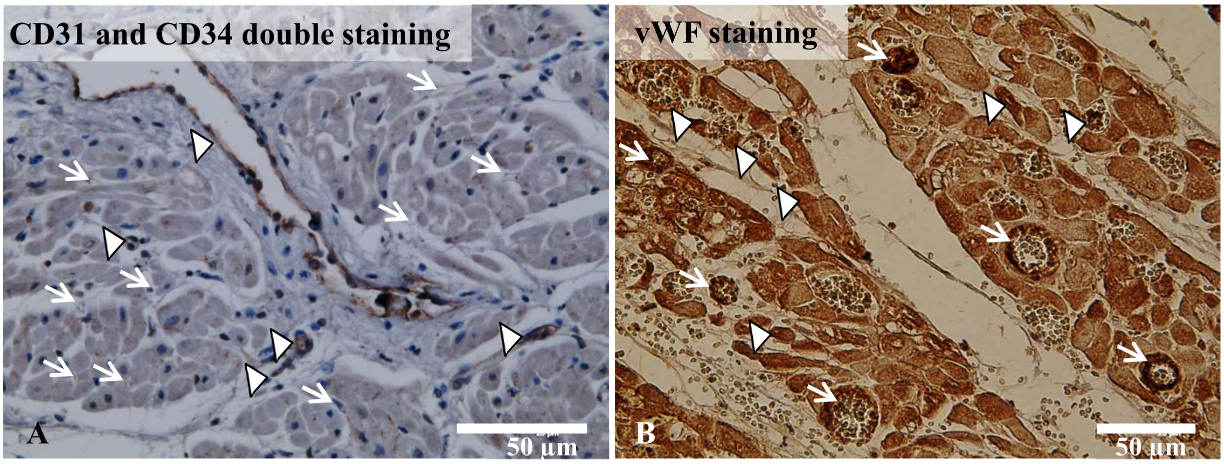

Figure 45: Antibody labelling of specific EC markers. The depicted markers were described to stain EC, which was only accomplished in a subset of microvessels for CD31 and CD34 (brown staining) (A). The presentation of both markers in a subset of blood vessels is shown with an arrow head. Unstained microvessels are indicated with arrows. The staining for vWF was also positive for damaged blood vessels (arrows) and vWF deposition in the tissue (arrow heads) (B). This staining did not lead to labelling of EC, but was also present after disruption of blood vessels. Therefore, none of the tested markers were used to investigate vascular damage, because they did not provide reliable results.

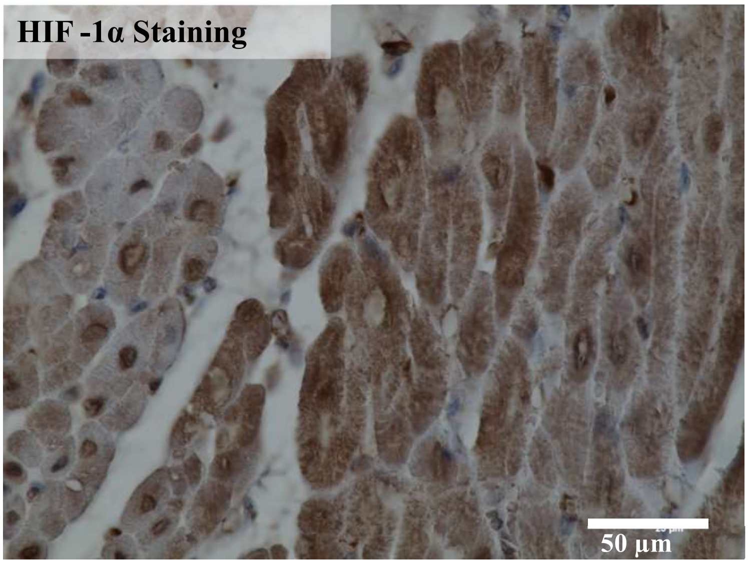

Figure 46: HIF-1α staining (brown) in cardiac tissue revealed its expression in the cytoplasm and its translocation into the nucleus, here representatively shown for the LV of the sham control. HIF-1α is only translocated into the nucleus under hypoxic conditions. Although loss of microvessels was observed, there were no irradiation– induced changes of HIF-1α translocation. As no positive control was available, this staining was not further employed.

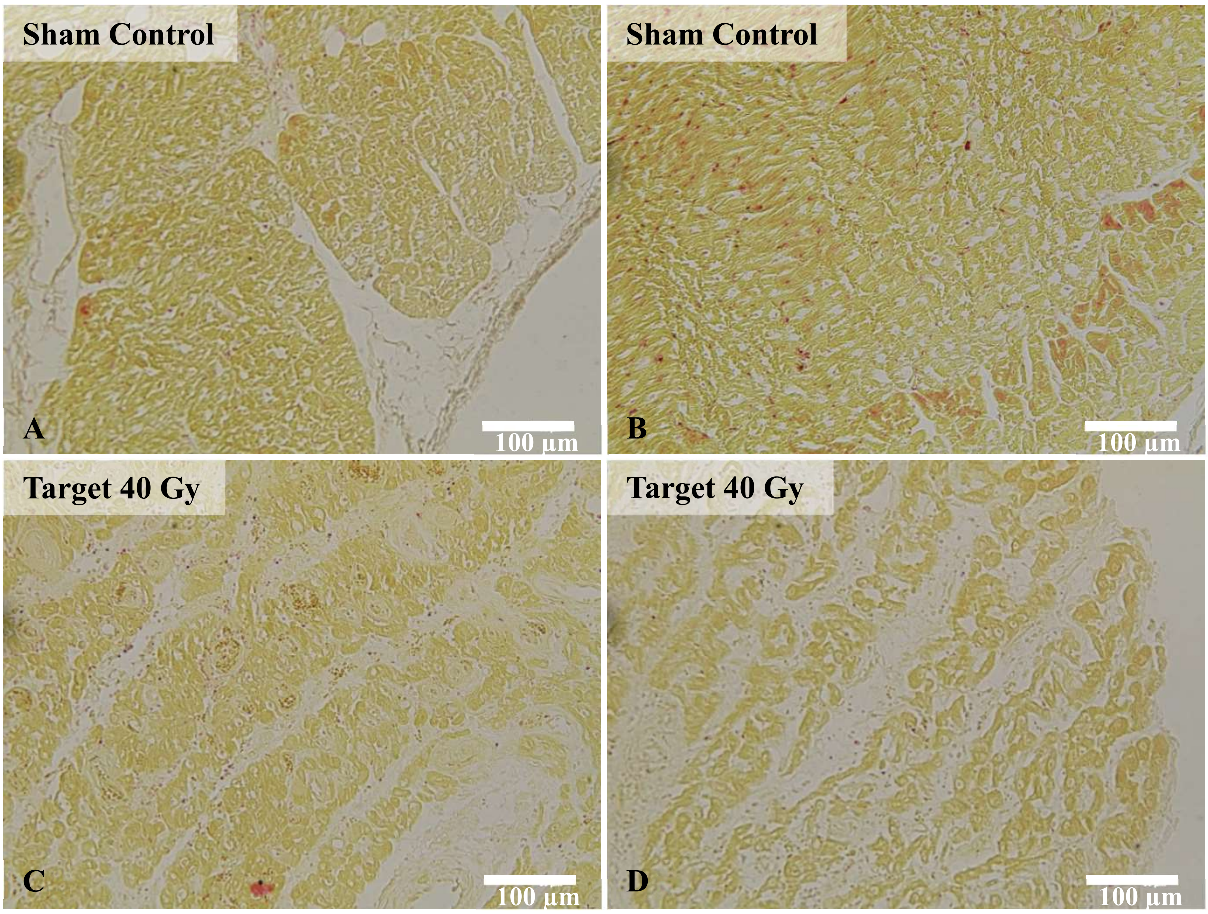

Figure 47: Representative images of the HBFP staining for the detection of hypoxia, which are exemplarily shown in the sham control (A and B) and after 40 Gy irradiation of the LV target (C and D). The background signal of the sham control tissue was comparable to the staining of the target areas, which was independently of the application of a counterstaining and the differentiation time. As no positive control was available, this staining was not further employed.

Table 15: Effects in the LV entrance channel region in percentage three and six months after carbon ion irradiation. No hints for an increased amount of haemorrhage were found, but the number of infiltrating immune cells area after irradiation was significantly higher than in sham controls. A loss of small vessels was only detected after three months. The amount of scar tissue increased after irradiation with time. These data suggest the appearance of damage in the LV entrance channel regions by the application of medium doses, but to a lower extent than in target areas.

Treatment and Time after Irradiation	**Haemorrhage**	**Inflammation**	**Small vessels (2-5 µm) in myocardium**	**Scar formation**
Pig G **(sham control, 3 months)**	0.6 %	1.6 %	100 %	0.4 %
Pig R **(LV 16 Gy, 3 months)**	3.3 %	15 %	27 %	5.6 %
Pig E **(sham control, 6 months)**	5.5 %	17 %	100 %	3.1 %
Pig T **(LV 16 Gy, 6 months)**	2.8 %	36 %	91 %	17.1 %

Table 16: Effects in the LAA entrance channel region in percentage six months after carbon ion irradiation. No changes in the amount of haemorrhage and inflammation were detected after the irradiation with medium doses during histological examinations. The investigations on the diameter of microvessels revealed a trend towards more small vessels compared to the sham control. The amount of scar tissue was tendencially only higher in one out of two pigs irradiated with the highest dose (Pig N, 17 Gy). In summary, there was no clear evidence for damage in the LAA entrance channel.

Treatment and Time after Irradiation	**Haemorrhage**	**Inflammation**	**Small vessels (2-5 µm) in myocardium**	**Scar formation**
Pig E **(sham control, 6 months)**	0.8 %	27 %	100 %	36 %
Pig H **(7 Gy, 6 months)**	2.1 %	31 %	122 %	24 %
Pig O **(9 Gy, 6 months)**	3.6 %	24 %	119 %	23 %
Pig I **(14 Gy, 6 months)**	0.7 %	12 %	161 %	21 %
Pig F **(17 Gy, 6 months)**	1.5 %	25 %	166 %	35 %
Pig N **(17 Gy, 6 months)**	5.3 %	27 %	138 %	50 %

Table 17: Effects in the LV outfield region in percentage three and six months after carbon ion irradiation. Tendencially, no increased appearance of tissue responses compared to the respective sham control was measured. In addition, the effects in LV target areas were significantly more marked than in corresponding outfield regions of the same heart. Therefore, no evidence for the spreading of damage was obtained. Significance compared to corresponding target area within the same animal is shown: * = p-value ≤ 0.05, ** = p-value ≤ 0.01, *** = p-value ≤ 0.001, **** = p-value ≤ 0.0001. Significance was tested with one-way Kruskal Wallis statistic and Dunn´s post hoc test.

Treatment and Time after Irradiation	**Haemorrhage**	**Inflammation**	**Small vessels (2-5 µm) in myocardium**	**Scar tissue**
Pig G **(0 Gy, 3 months)**	1.2 %	5.4 %	100 %	2.5 %
Pig R **(0 Gy, 3 months)**	1.6 % -	4.1 % *	72 % *	0.8 %
Pig S **(0 Gy, 3 months)**	1.5 % ****	5.4 % ****	12 % ****	2.2 %
Pig E **(0 Gy, 6 months)**	5.5 %	17 %	100 %	3.1 %
Pig T **(0 Gy, 6 months)**	2.9 % ****	8.4 % ****	63 % ****	2.9 %

Table 18: Effects in the RV outfield region in percentage three months after carbon ion irradiation. Similar to the results in the LV outfield regions, the appearance of tissue responses was not different to the respective sham control. The effects in RV entrance channel regions did also not differ from the respective outfield regions. Significance compared to corresponding entrance channel region within the same animal is shown: * = p-value ≤ 0.05, ** = p-value ≤ 0.01, *** = p-value ≤ 0.001, **** = p-value ≤ 0.0001. Significance was tested with one-way Kruskal Wallis statistic and Dunn´s post hoc test.

Treatment and Time after Irradiation	**Haemorrhage**	**Inflammation**	**Small vessels (2-5 µm) in myocardium**	**Scar tissue**
Pig G **(0 Gy, 3 months)**	6.2 %	26 %	100 %	9.5 %
Pig R **(0 Gy, 3 months)**	2.9 % **	10.8 % -	82 % -	4.1 %
Pig S **(0 Gy, 3 months)**	2.4 % -	12.2 % -	67 % -	6.6 %

Table 19: Effects in the LAA outfield region in percentage six months after carbon ion irradiation. No changes in the appearance of tissue responses were obtained compared to the sham control. A pronounced appearance of tissue effects in LAA entrance channel regions was only detected occasionally compared to LAA outfield regions. Significance compared to corresponding entrance channel region within the same animal is shown: * = p-value ≤ 0.05, ** = p-value ≤ 0.01, *** = p-value ≤ 0.001, **** = p-value ≤ 0.0001. Significance was tested with one-way Kruskal Wallis statistic and Dunn´s post hoc test.

Treatment and Time after Irradiation	**Haemorrhage**		**Inflammation**		**Small vessels (2-5 µm) in myocardium**		**Scar tissue**
Pig E **(0 Gy, 6 months)**	2.2 %		53.2 %		100 %		32.4 %
Pig H **(0 Gy, 6 months)**	2.6 %	-	61.5 %	-	97 %	-	36.7 %
Pig O **(0 Gy, 6 months)**	3.5 %	-	16.8 %	-	113 %	-	32.7 %
Pig I **(0 Gy, 6 months)**	1.4 %	-	52.8 %	****	131 %	-	27.2 %
Pig F **(0 Gy, 6 months)**	7.3 %	-	50.6 %	-	101 %	****	23.2 %
Pig N **(0 Gy, 6 months)**	1.1 %	-	66.7 %	-	103 %	-	44.3 %

Table 20: Effects in the RAA outfield region in percentage six months after carbon ion irradiation. No difference in the manifestation of tissue responses compared to the sham control was found. In addition, these results are similar to the findings in RAA entrance channel regions. Significance compared to corresponding entrance channel region within the same animal is shown: * = p-value ≤ 0.05, ** = p-value ≤ 0.01, *** = p-value ≤ 0.001, **** = p-value ≤ 0.0001. Significance was tested with one-way Kruskal Wallis statistic and Dunn´s post hoc test.

Treatment and Time after Irradiation	Haemorrhage		Inflammation		Small vessels (2-5 µm) in myocardium		Scar tissue
Pig E **(0 Gy, 6 months)**	4.9 %		35.3 %		100 %		28.7 %
Pig H **(0 Gy, 6 months)**	2.1 %	-	43.1 %	-	71 %	-	23.6 %
Pig O **(0 Gy, 6 months)**	7.4 %	-	5.5 %	-	68 %	-	24.5 %
Pig I **(0 Gy, 6 months)**	0.6 %	-	18.9 %	-	83 %	-	17.2 %
Pig F **(0 Gy, 6 months)**	4.9 %	-	26.8 %	-	80 %	-	46.3 %
Pig N **(0 Gy, 6 months)**	2.4 %	-	21.7 %	-	77 %	-	21.8 %

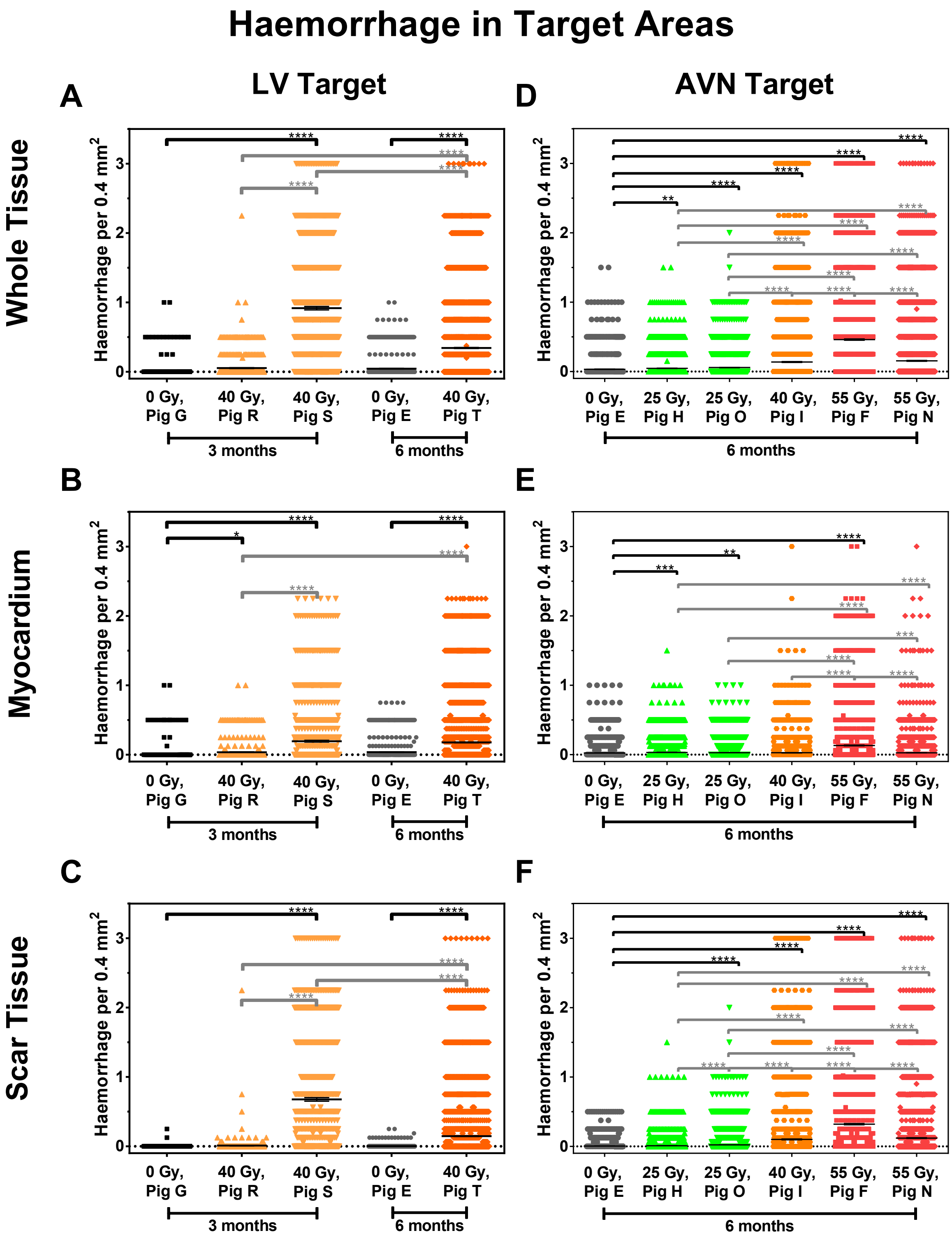

Figure 48: Haemorrhage occurred most pronounced in scar tissue of target areas of animals with strong fibrotic response. Although it was less marked at six months than before, its amount increased with dose. Target areas were analysed either in the whole area after LV (A) or AVN targeted irradiation (D) or discriminated accordingly between myocardium (B and E) and scar tissue (C and F). Scoring per visual field, mean and SEM are shown. * = p-value ≤ 0.05, ** = p-value ≤ 0.01, *** = p-value ≤ 0.001, **** = p-value ≤ 0.0001. Significance was tested with one-way Kruskal Wallis statistic and Dunn´s post hoc test.

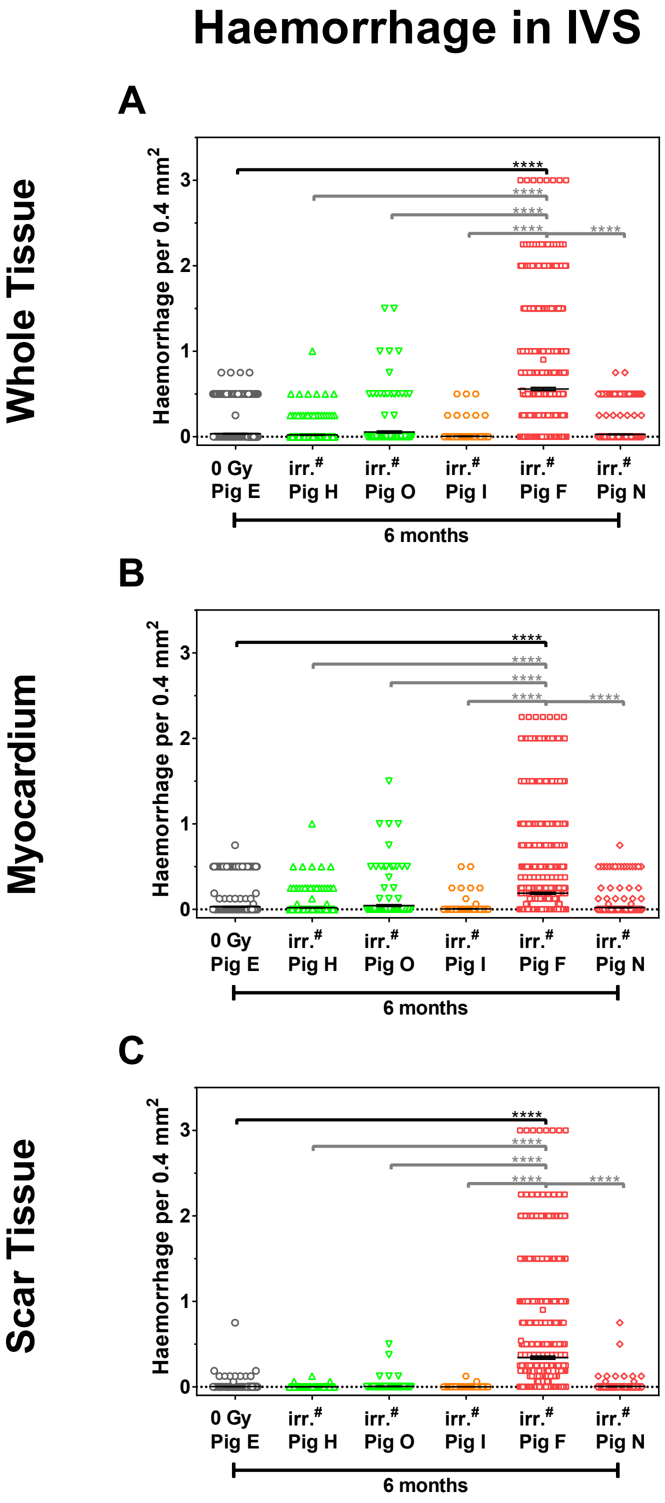

Figure 49: In IVS, a substantial amount of haemorrhage was only detected in IVS of the one animal with persistent AV block (Pig F). This effect was most pronounced in scar tissue. Samples from the IVS were analysed either in the whole area (A) or discriminated between myocardium (B) and scar tissue (C). . The doses to the IVS were not determined = irr.$^{\#}$. Scoring per visual field, mean and SEM are shown. * = p-value ≤ 0.05, ** = p-value ≤ 0.01, *** = p-value ≤ 0.001, **** = p-value ≤ 0.0001. Significance was tested with one-way Kruskal Wallis statistic and Dunn´s post hoc test.

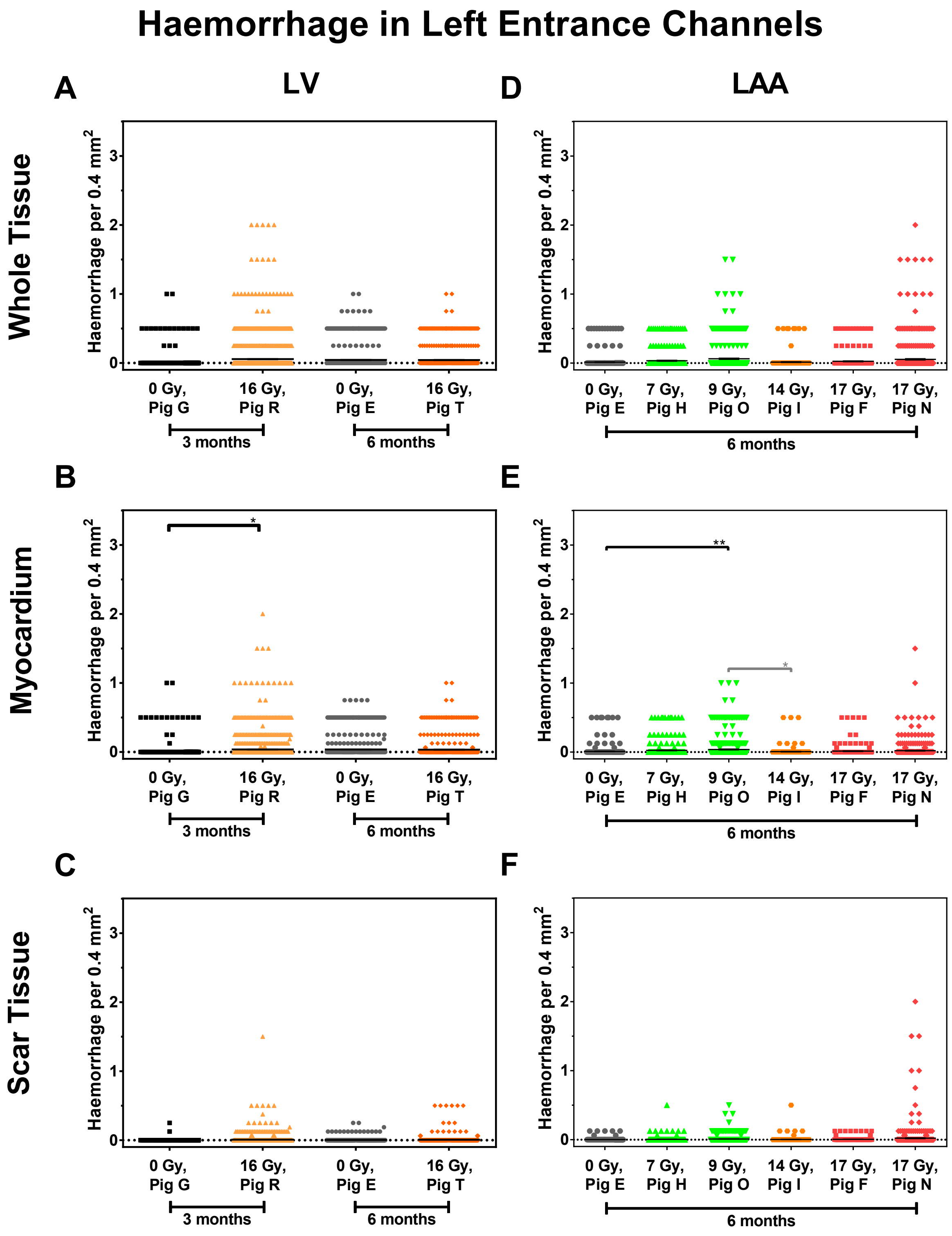

Figure 50: Haemorrhage was only infrequently observed in left entrance channel regions. These effects were evenly distributed among myocardium and scar tissue. Samples from the sinistral entrance channel regions were analysed either in the whole area after LV (A) or AVN targeted irradiation (D) or discriminated accordingly between myocardium (B and E) and scar tissue (C and F). Scoring per visual field, mean and SEM are shown. * = p-value ≤ 0.05, ** = p-value ≤ 0.01, *** = p-value ≤ 0.001, **** = p-value ≤ 0.0001. Significance was tested with one-way Kruskal Wallis statistic and Dunn´s post hoc test.

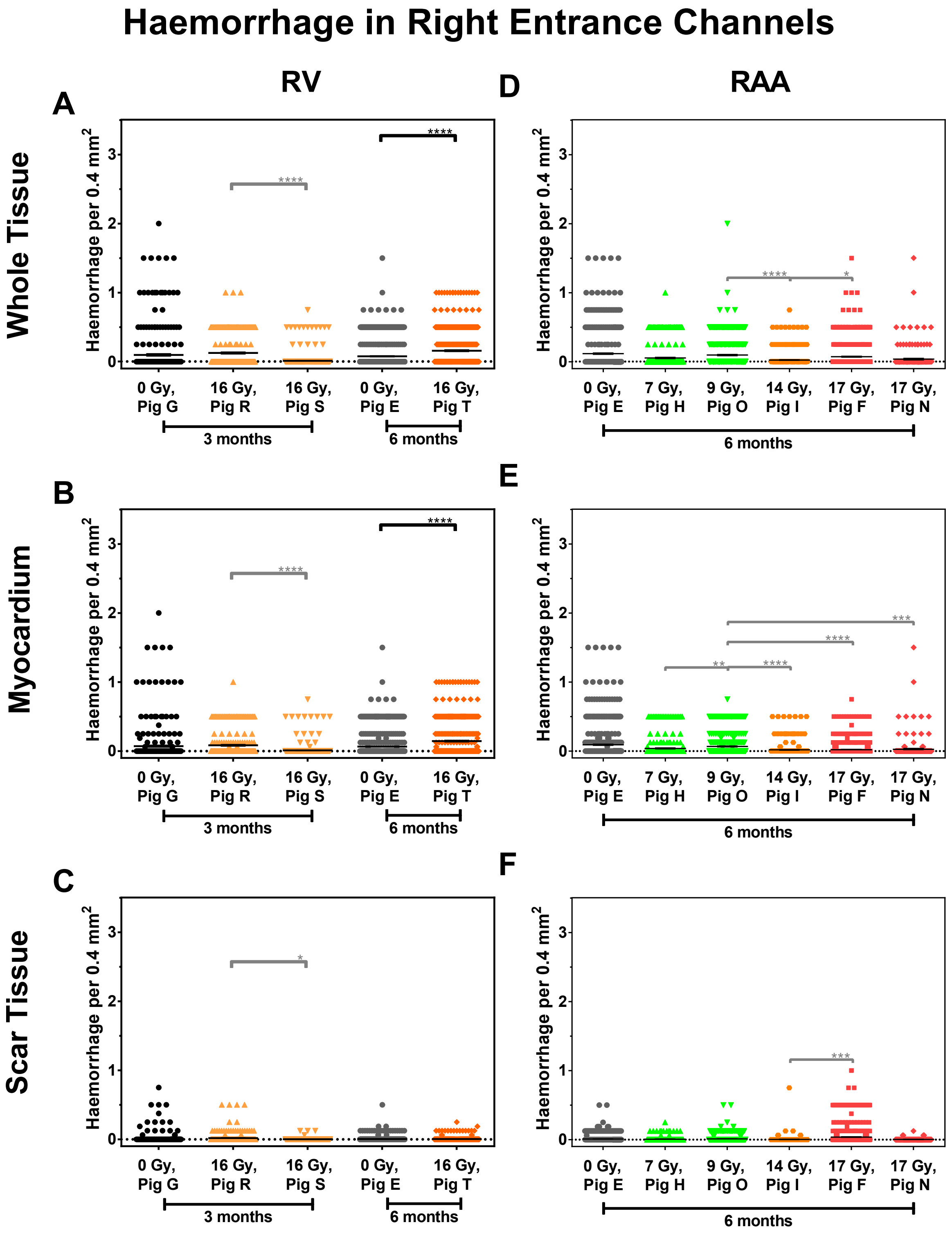

Figure 51: Larger, but still small, quantities of haemorrhage appeared only in the myocardium of right entrance channel regions. Samples from the dextral entrance channel regions were analysed either in the whole area after LV (A) or AVN targeted irradiation (D) or discriminated accordingly between myocardium (B and E) and scar tissue (C and F). Scoring per visual field, mean and SEM are shown. * = p-value ≤ 0.05, ** = p-value ≤ 0.01, *** = p-value ≤ 0.001, **** = p-value ≤ 0.0001. Significance was tested with one-way Kruskal Wallis statistic and Dunn´s post hoc test.

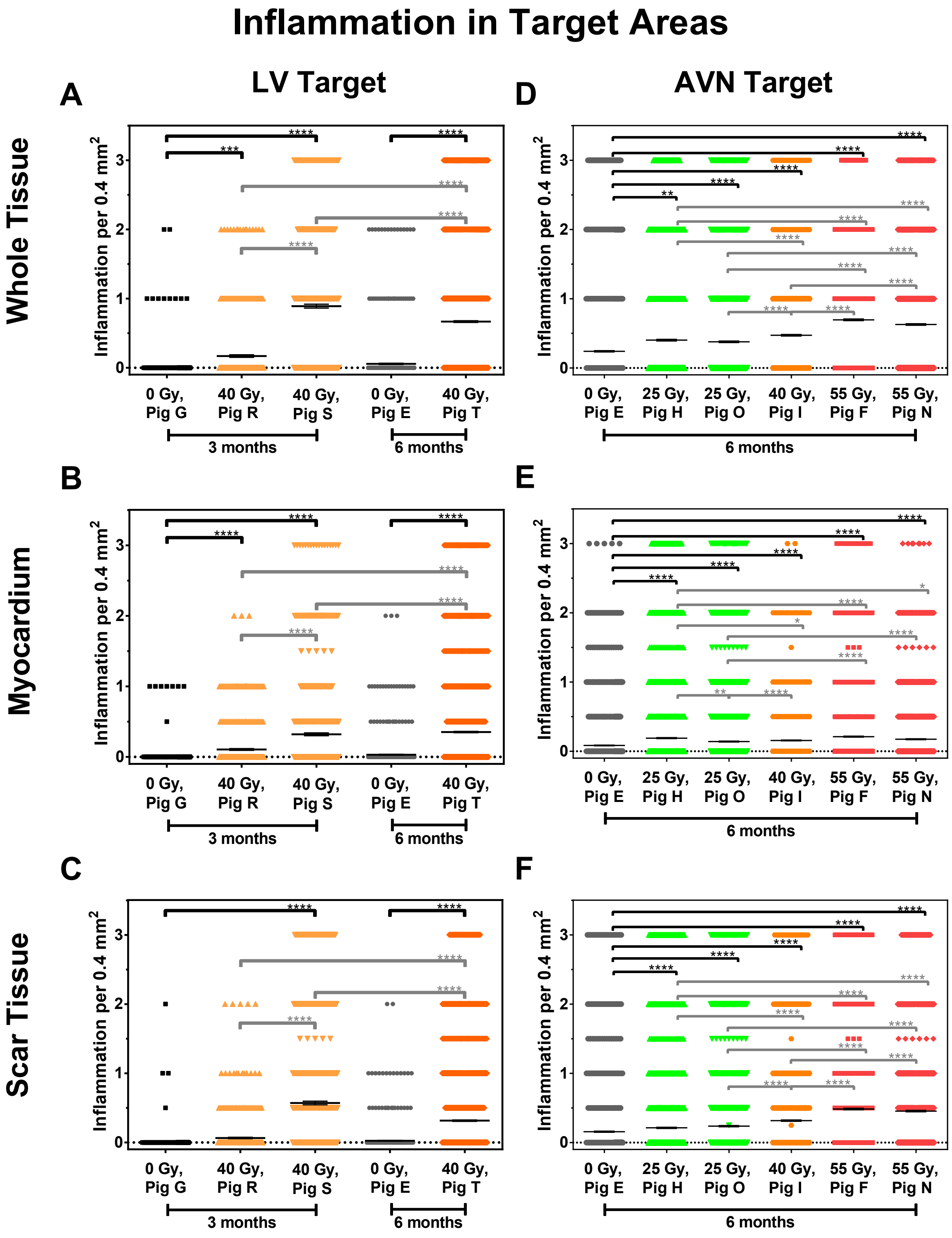

Figure 52: A substantial amount of inflammation was detected in animals with strong fibrotic response, particularly in scar tissue of target areas. The manifestation of this effect increased with dose. Target areas were analysed either in the whole area after LV (A) or AVN targeted irradiation (D) or discriminated accordingly between myocardium (B and E) and scar tissue (C and F). Scoring per visual field, mean and SEM are shown. * = p-value ≤ 0.05, ** = p-value ≤ 0.01, *** = p-value ≤ 0.001, **** = p-value ≤ 0.0001. Significance was tested with one-way Kruskal Wallis statistic and Dunn´s post hoc test.

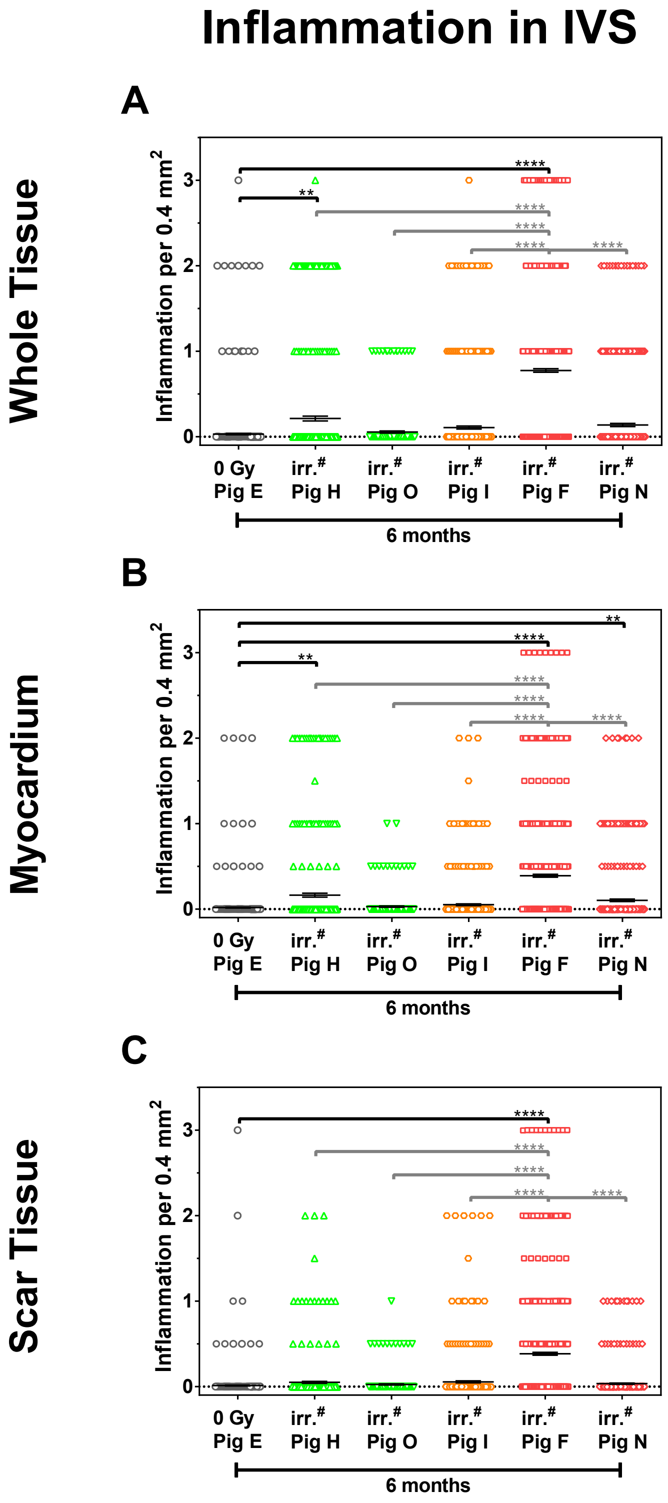

Figure 53: Increased infiltration of immune cells was detected in particular in myocardium of IVS. The most amount of inflammation was detected in the animal with persistent AV block (Pig F). Samples from the IVS were analysed either in the whole area (A) or discriminated between myocardium (B) and scar tissue (C). The doses to the IVS were not determined = irr.$^{\#}$. Scoring per visual field, mean and SEM are shown. * = p-value ≤ 0.05, ** = p-value ≤ 0.01, *** = p-value ≤ 0.001, **** = p-value ≤ 0.0001. Significance was tested with one-way Kruskal Wallis statistic and Dunn´s post hoc test.

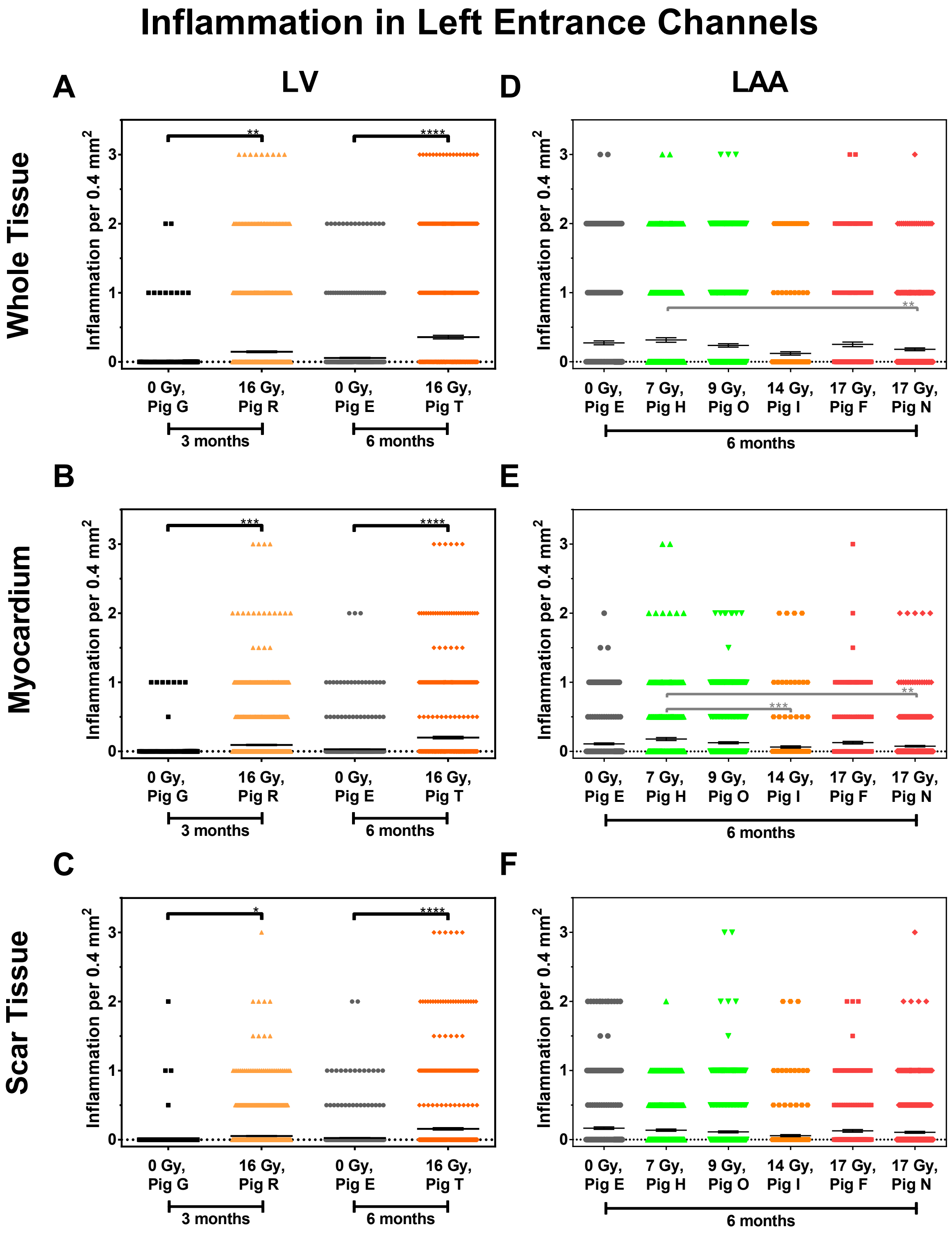

Figure 54: The comparison of left entrance channel regions showed increased levels of inflammation only in LV entrance channel regions. No difference between myocardium and scar tissue was detected. Samples from the sinistral entrance channel regions were analysed either in the whole area after LV (A) or AVN targeted irradiation (D) or discriminated accordingly between myocardium (B and E) and scar tissue (C and F). Scoring per visual field, mean and SEM are shown. * = p-value ≤ 0.05, ** = p-value ≤ 0.01, *** = p-value ≤ 0.001, **** = p-value ≤ 0.0001. Significance was tested with one-way Kruskal Wallis statistic and Dunn´s post hoc test.

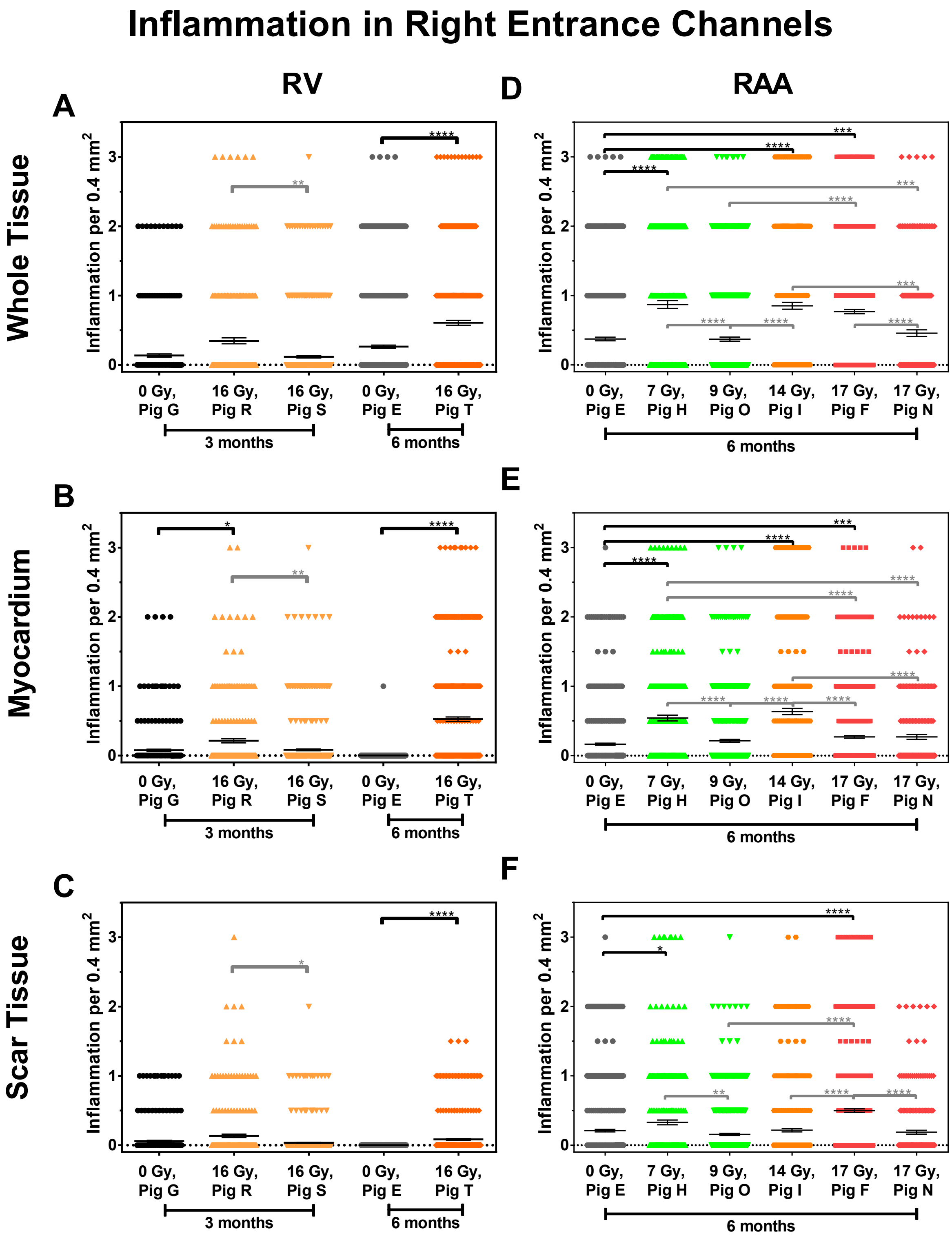

Figure 55: Inflammation was most pronounced in the myocardium of both right entrance channel regions. Samples from the dextral entrance channel regions were analysed either in the whole area after LV (A) or AVN targeted irradiation (D) or discriminated accordingly between myocardium (B and E) and scar tissue (C and F). Scoring per visual field, mean and SEM are shown. * = p-value ≤ 0.05, ** = p-value ≤ 0.01, *** = p-value ≤ 0.001, **** = p-value ≤ 0.0001. Significance was tested with one-way Kruskal Wallis statistic and Dunn´s post hoc test.

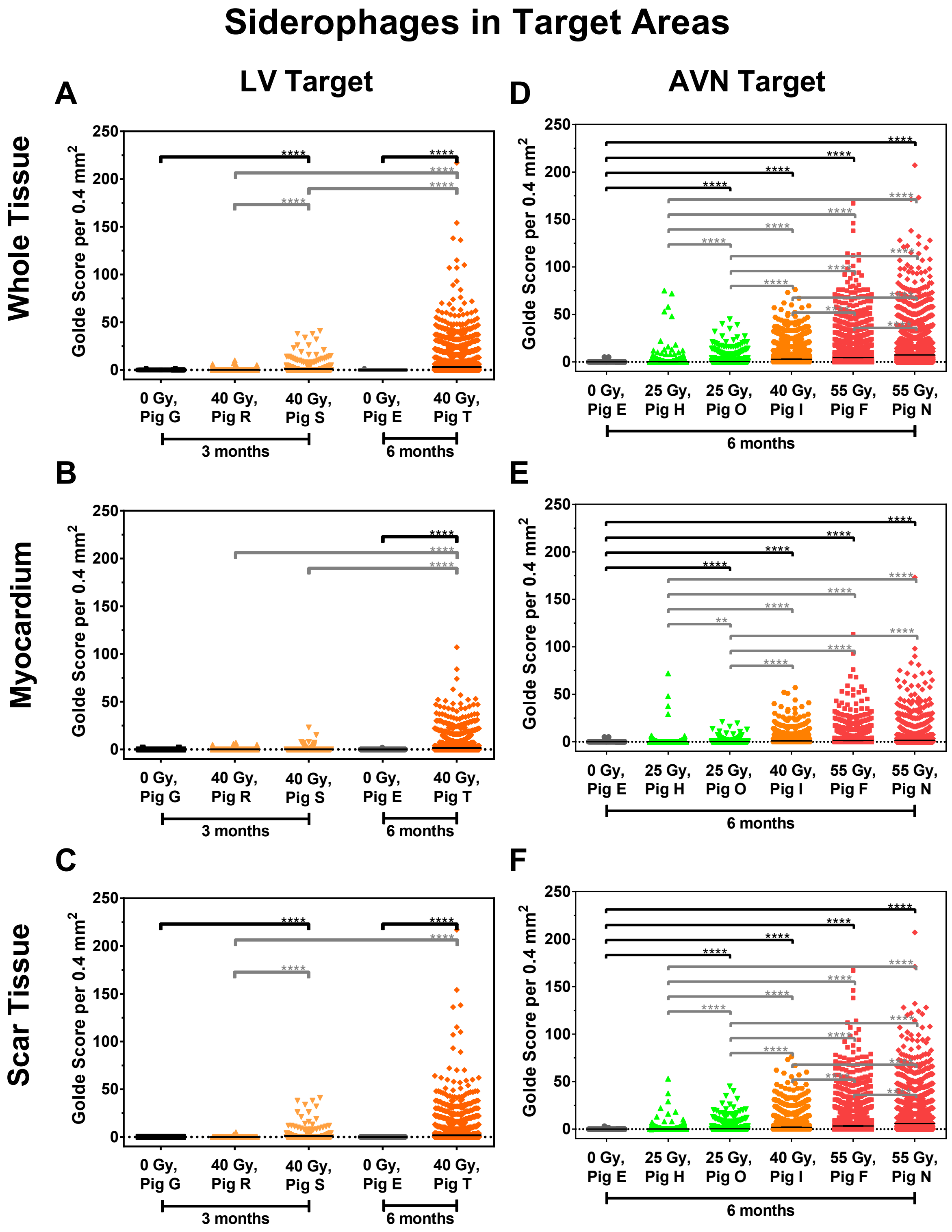

Figure 56: The formation of siderophages increased with time and dose. The appearance of siderophages in the myocardium was not detected before six months after irradiation. Target areas were analysed either in the whole area after LV (A) or AVN targeted irradiation (D) or discriminated accordingly between myocardium (B and E) and scar tissue (C and F). Scoring per visual field, mean and SEM are shown. * = p-value ≤ 0.05, ** = p-value ≤ 0.01, *** = p-value ≤ 0.001, **** = p-value ≤ 0.0001. Significance was tested with one-way Kruskal Wallis statistic and Dunn´s post hoc test.

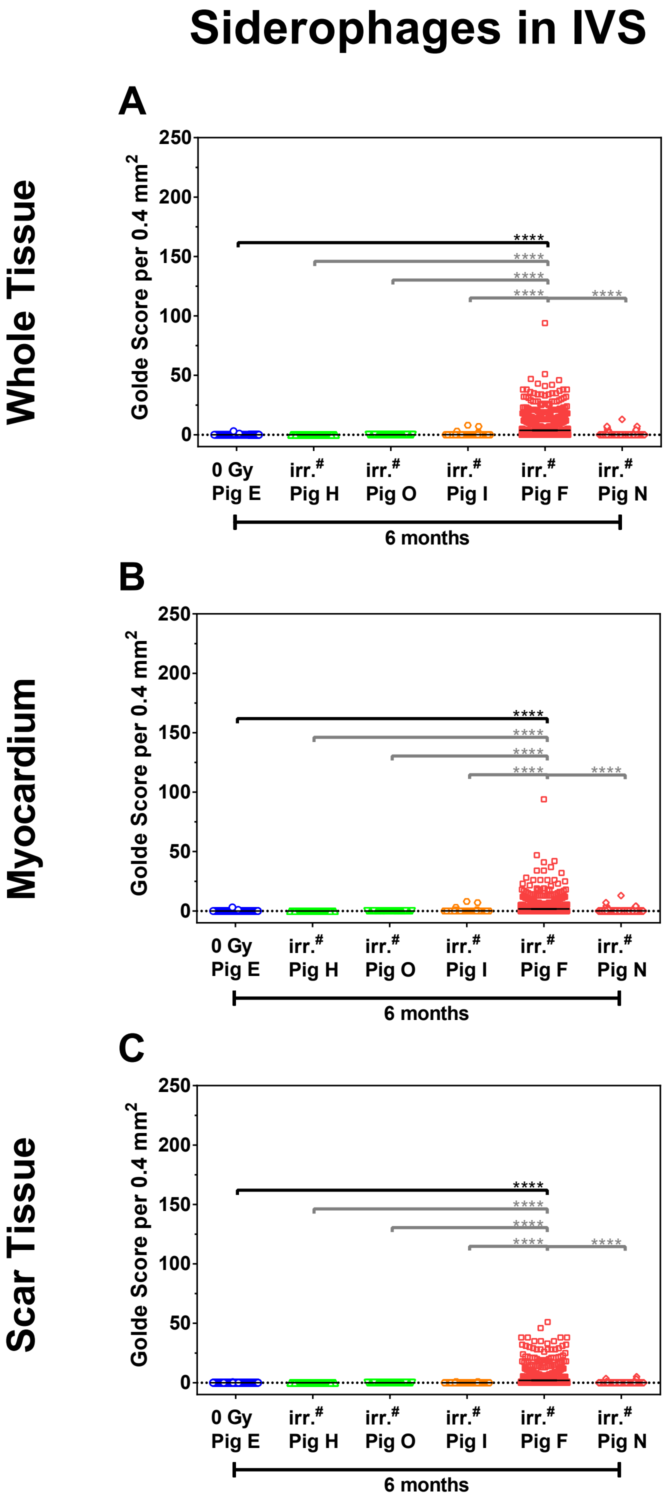

Figure 57: An augmented formation of siderophages was measured in the IVS of the animal with persistent AV block (Pig F). Siderophages manifested evenly distributed among myocardium and scar tissue. Samples from the IVS were analysed either in the whole area (A) or discriminated between myocardium (B) and scar tissue (C). The doses to the IVS were not determined = irr.$^{\#}$. Scoring per visual field, mean and SEM are shown. * = p-value ≤ 0.05, ** = p-value ≤ 0.01, *** = p-value ≤ 0.001, **** = p-value ≤ 0.0001. Significance was tested with one-way Kruskal Wallis statistic and Dunn´s post hoc test.

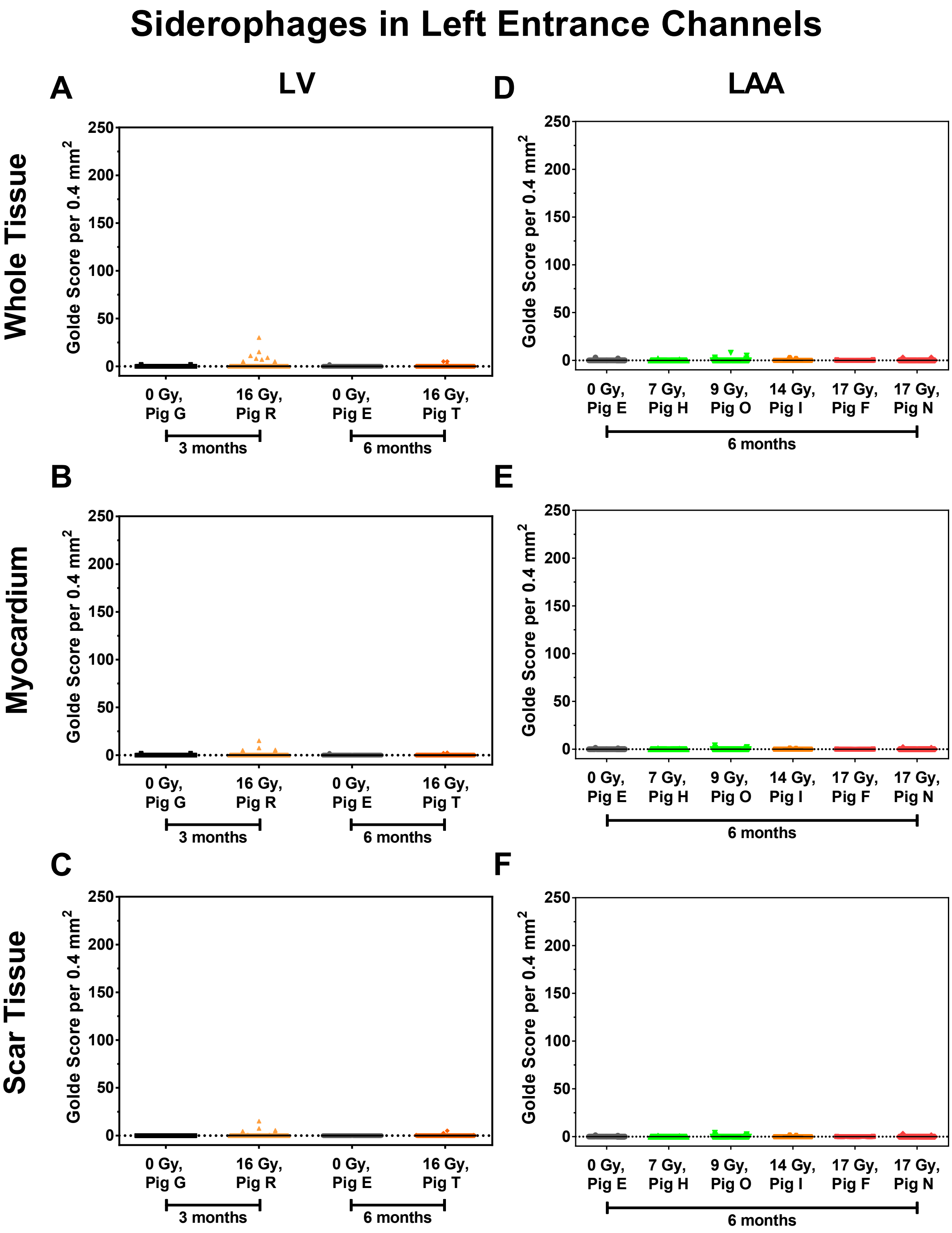

Figure 58: Siderophages could not be assessed in myocardium or scar tissue of left entrance channel regions. Samples from the sinistral entrance channel regions were analysed either in the whole area after LV (A) or AVN targeted irradiation (D) or discriminated accordingly between myocardium (B and E) and scar tissue (C and F). Scoring per visual field, mean and SEM are shown. * = p-value ≤ 0.05, ** = p-value ≤ 0.01, *** = p-value ≤ 0.001, **** = p-value ≤ 0.0001. Significance was tested with one-way Kruskal Wallis statistic and Dunn´s post hoc test.

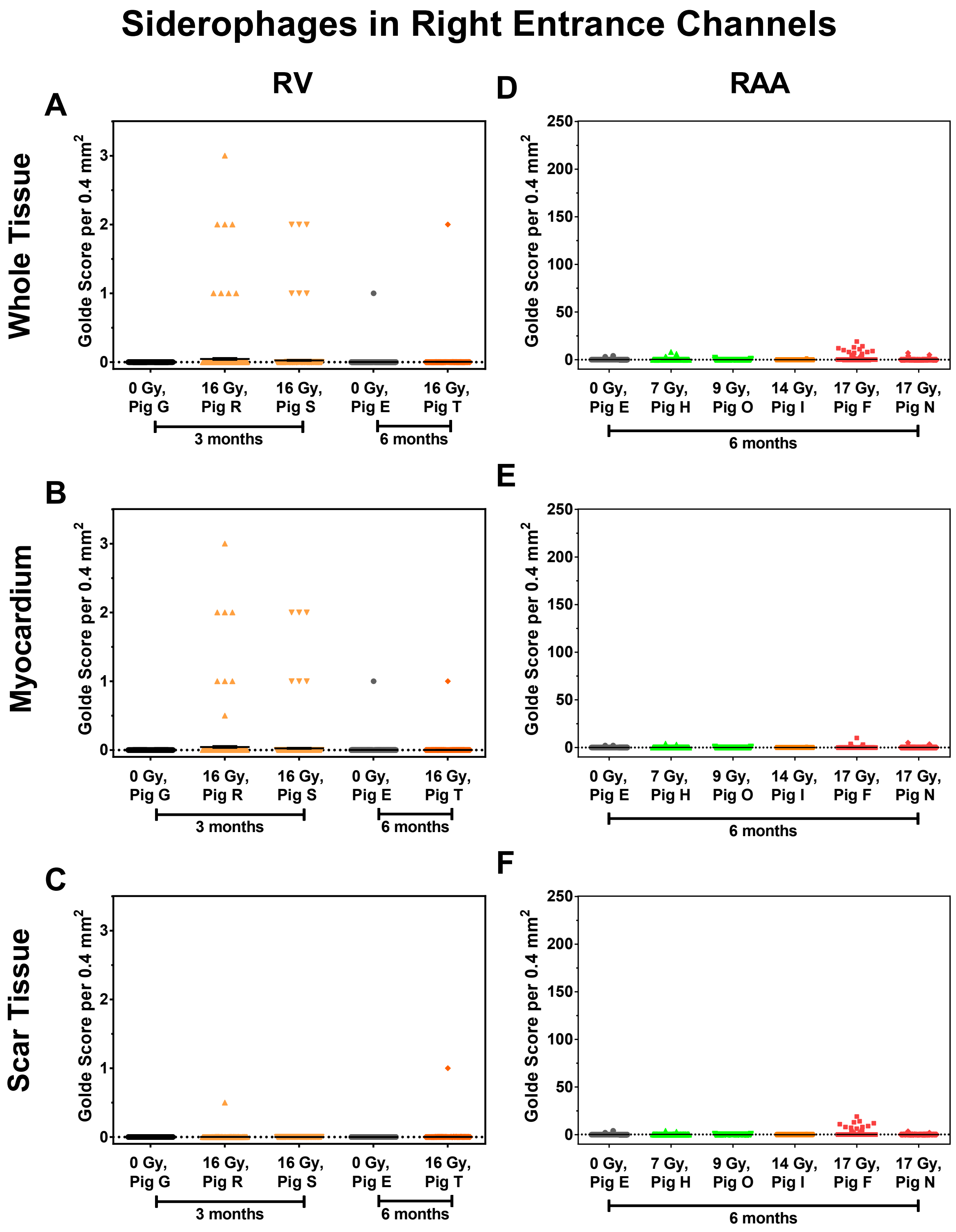

Figure 59: Comparably to left entrance channel areas, siderophages were also not detected in either tissue type of right entrance channel regions. Samples from the dextral entrance channel regions were analysed either in the whole area after LV (A) or AVN targeted irradiation (D) or discriminated accordingly between myocardium (B and E) and scar tissue (C and F). * = p-value ≤ 0.05, ** = p-value ≤ 0.01, *** = p-value ≤ 0.001, **** = p-value ≤ 0.0001. Significance was tested with one-way Kruskal Wallis statistic and Dunn´s post hoc test.

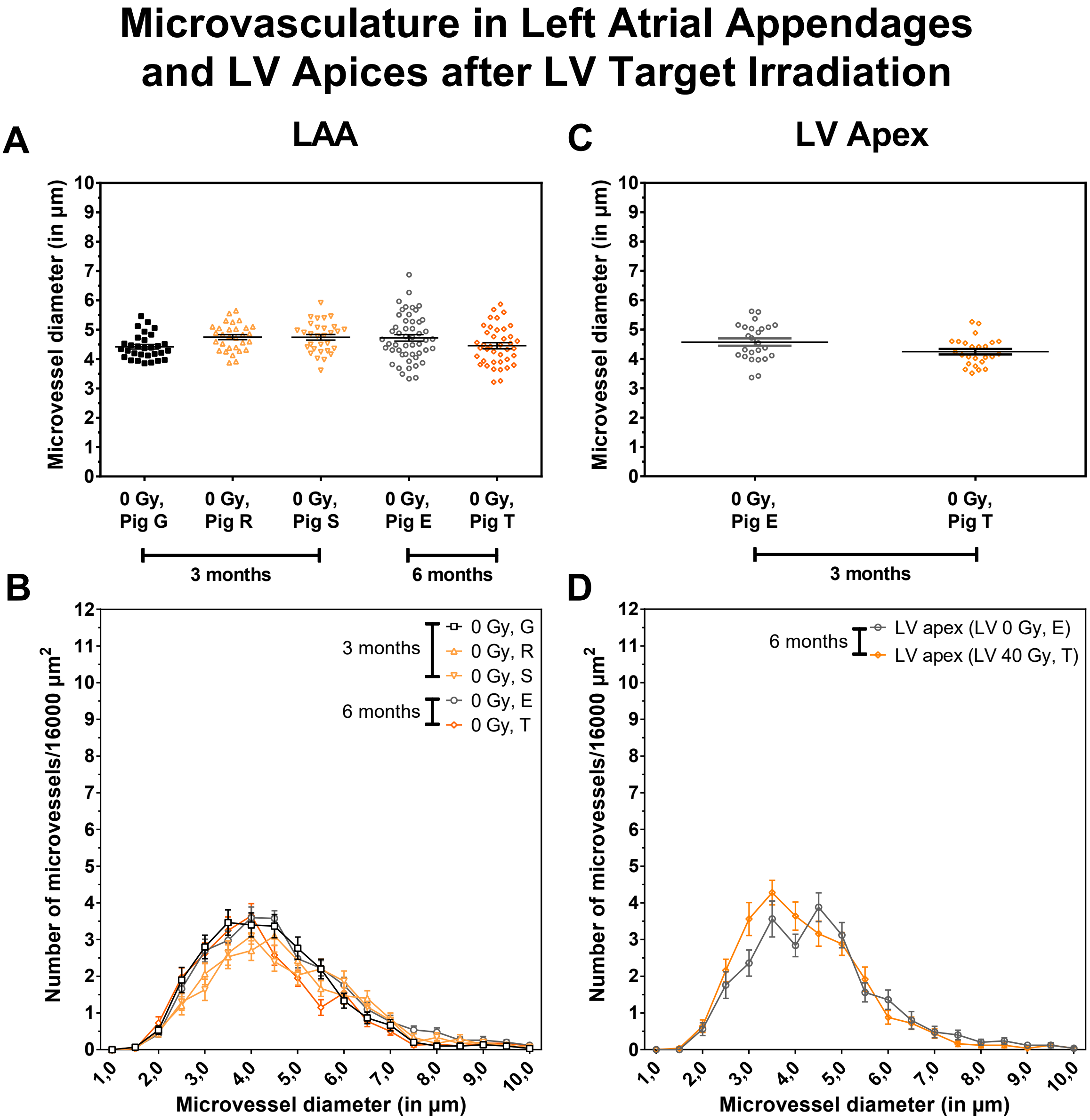
Microvasculature in Left Atrial Appendages and LV Apices after LV Target Irradiation

Figure 60: No change in the distribution of the microvascular diameter in outfield regions after LV target irradiation. The mean diameter of microvessels in the LAA (A) or LV (C) entrance channel region and the corresponding frequency distribution (B and D) were measured in the myocardium. Mean diameter, mean and SEM are shown. * = p-value ≤ 0.05, ** = p-value ≤ 0.01, *** = p-value ≤ 0.001, **** = p-value ≤ 0.0001. Significance was tested with one-way Kruskal Wallis statistic and Dunn´s post hoc test.

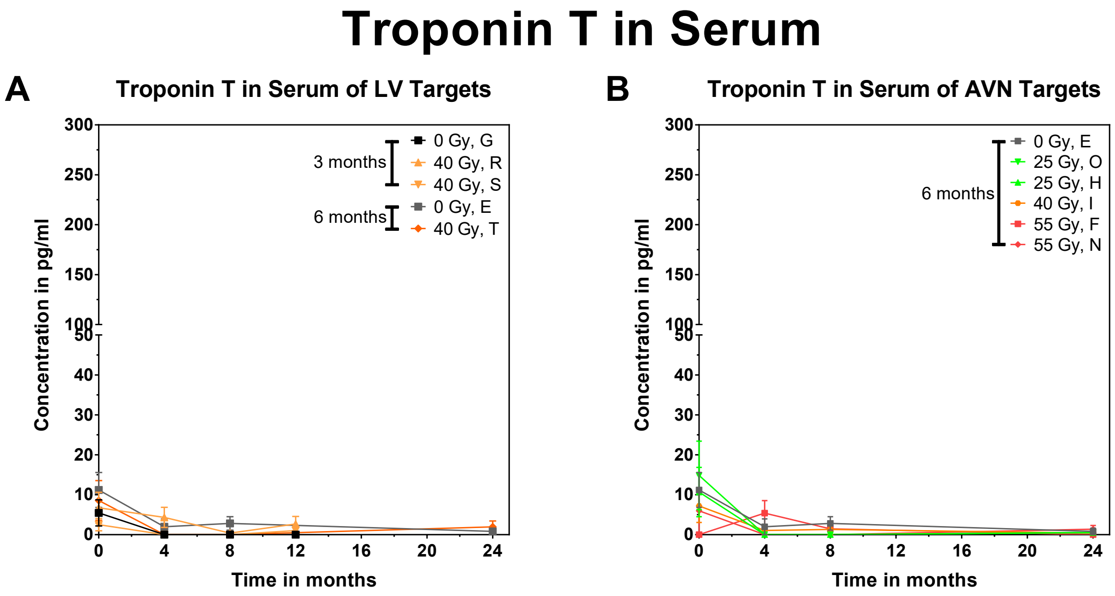

Figure 61: The irradiation of LV and AVN targets did not lead to a changed release of troponin T over time. Concentrations of troponin T were measured at different time points after LV (A) and AVN (B) target irradiation in serum. Concentration of technical replicates, mean and SEM are shown. * = p-value ≤ 0.05, ** = p-value ≤ 0.01, *** = p-value ≤ 0.001, **** = p-value ≤ 0.0001. Significance was tested with one-way Kruskal Wallis statistic and Dunn´s post hoc test.

HMGB-1 and vWF in Pericardial Fluid and Serum

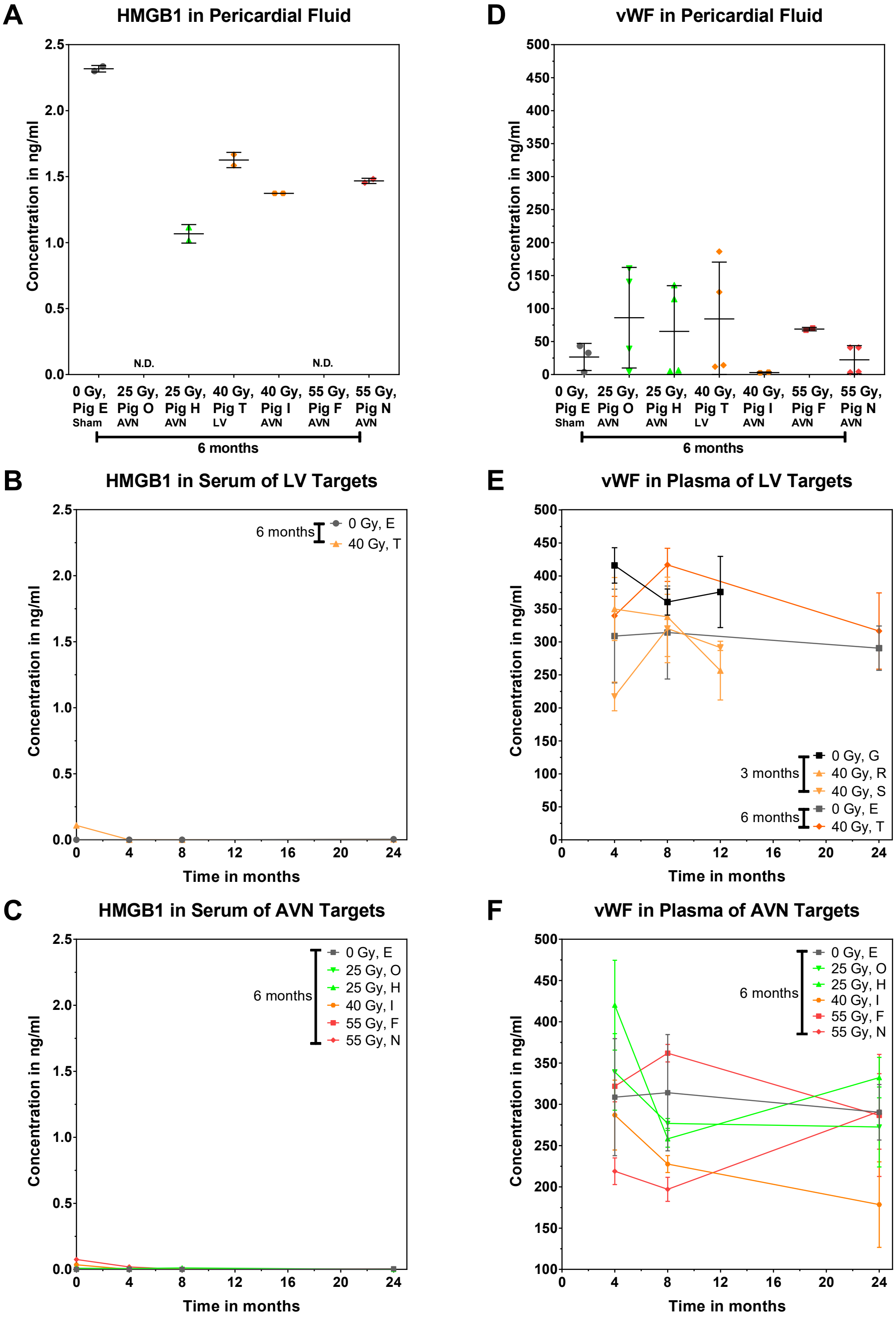

Figure 62: The release of HMGB1 and vWF was not increased after irradiation. HMGB1 and vWF concentrations were measured six months after LV target (A) and AVN target (D) irradiation in PF and at different time points after LV target (B and D) and AVN target (C and F) irradiation in serum. Concentration of technical replicates, mean and SEM are shown. N.D. = not determined. * = p-value ≤

0.05, ** = p-value ≤ 0.01, *** = p-value ≤ 0.001, **** = p-value ≤ 0.0001. Significance was tested with one-way Kruskal Wallis statistic and Dunn´s post hoc test.

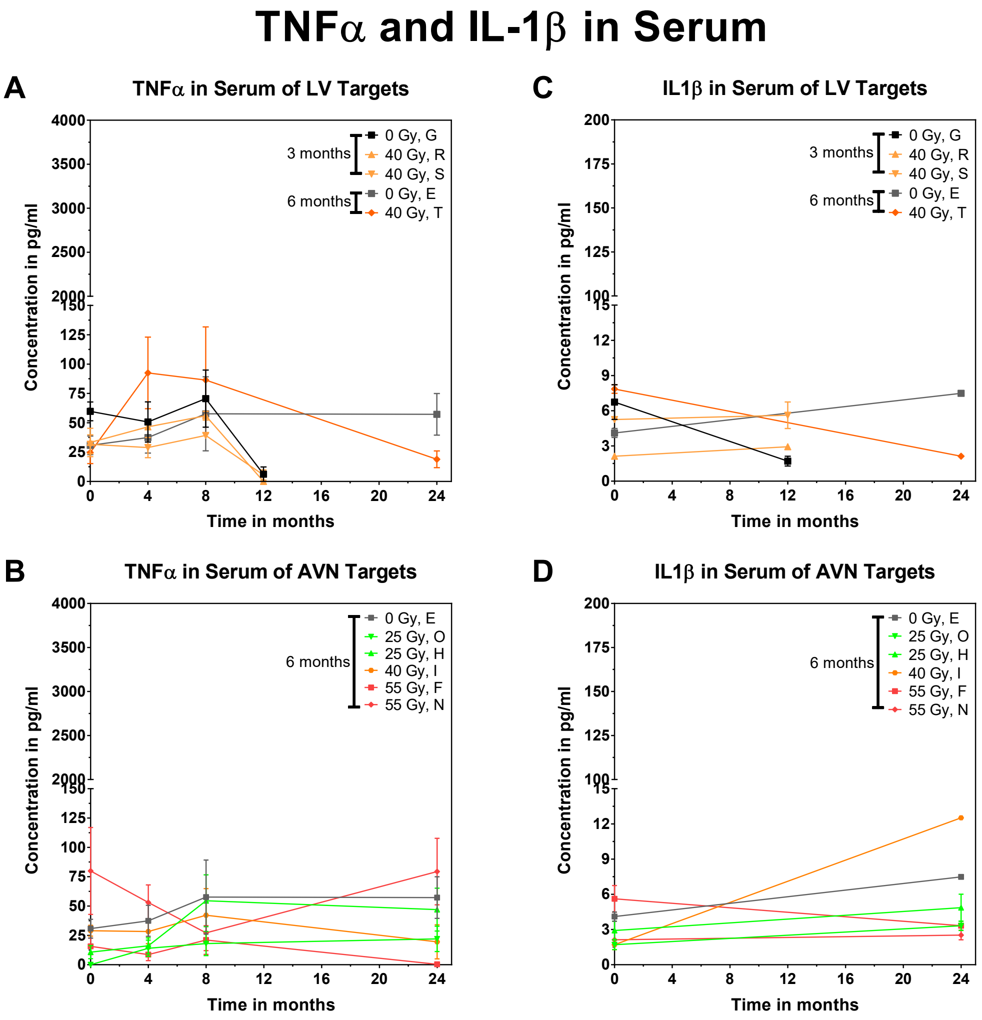

Figure 63: Although the release of TNFα and IL-1β fluctuated over time in the serum of irradiated animals, their concentrations were not considerably elevated. TNFα and IL-1β concentrations were measured at different time points after LV target (B and D) and AVN target (C and F) irradiation in serum. Concentration of technical replicates, mean and SEM are shown. N.D. = not determined. * = p-value ≤ 0.05, ** = p-value ≤ 0.01, *** = p-value ≤ 0.001, **** = p-value ≤ 0.0001. Significance was tested with one-way Kruskal Wallis statistic and Dunn´s post hoc test.

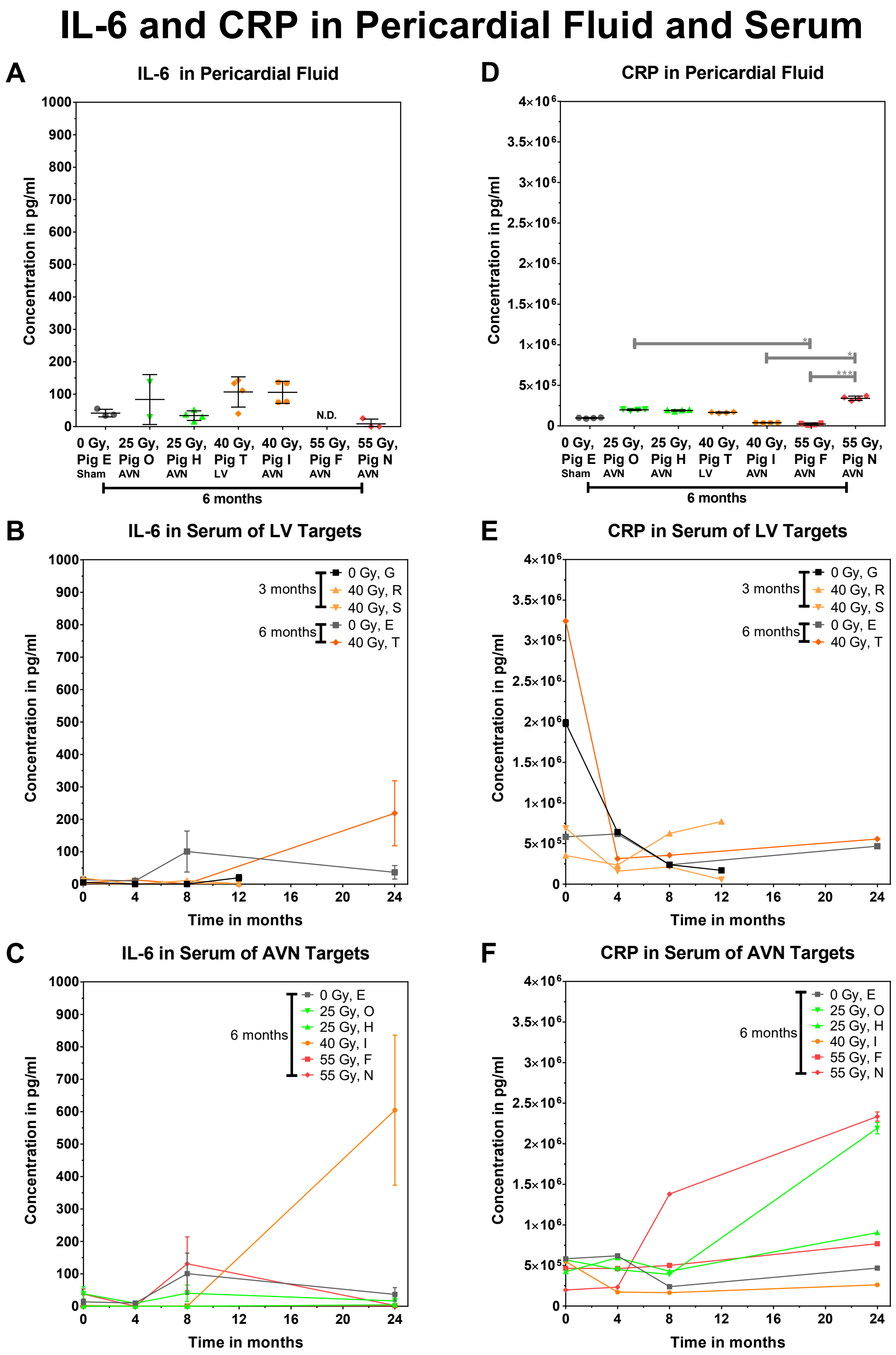

Figure 64: Measurement of IL-6 and CRP release in PF revealed a higher release of only CRP after AVN irradiation. Concentrations did not increase with dose. Compared to measurements before irradiation (0 months), both markers were not altered in serum samples. IL6 and CRP concentrations were measured six months after LV target (A) and AVN target (D) irradiation in PF and at different time points after LV target (B and D) and AVN target (C and F) irradiation in serum. Concentration of technical replicates,

mean and SEM are shown. The results for CRP release in PF are depicted again (Figure 42) to give a complete overview. N.D. = not determined. * = p-value ≤ 0.05, ** = p-value ≤ 0.01, *** = p-value ≤ 0.001, **** = p-value ≤ 0.0001. Significance was tested with one-way Kruskal Wallis statistic and Dunn´s post hoc test.

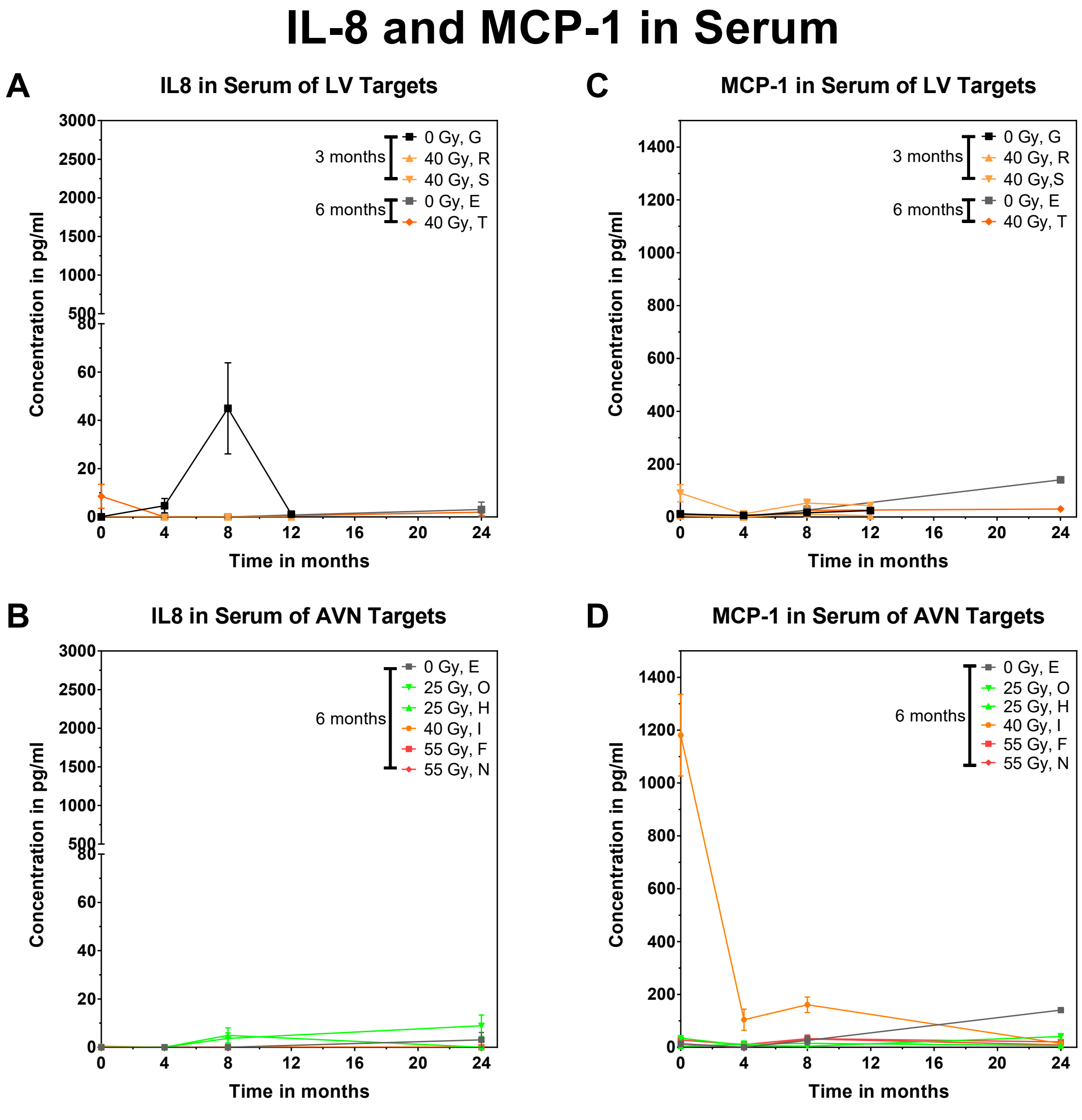

Figure 65: The release of IL-8 and MCP-1 did not change over time after irradiation in serum. IL-8 and MCP-1 concentrations were measured at different time points after LV target (B and D) and AVN target (C and F) irradiation in serum. Concentration of technical replicates, mean and SEM are shown. N.D. = not determined. * = p-value ≤ 0.05, ** = p-value ≤ 0.01, *** = p-value ≤ 0.001, **** = p-value ≤ 0.0001. Significance was tested with one-way Kruskal Wallis statistic and Dunn´s post hoc test.

IFNγ in Pericardial Fluid and Serum

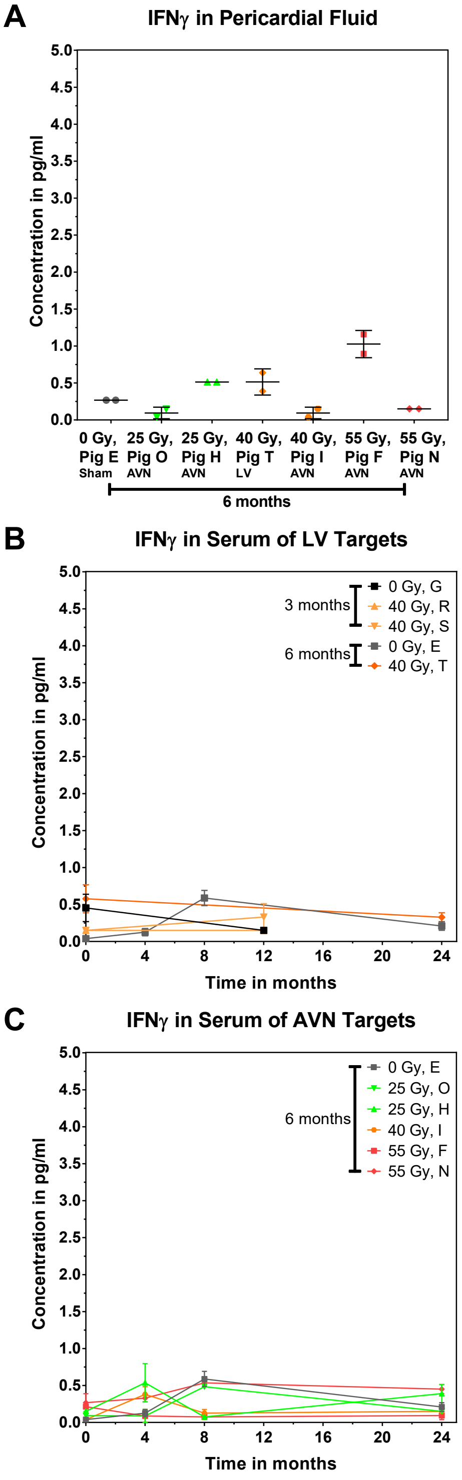

Figure 66: The release of IFNγ was not affected by cardiac irradiation. IFNγ concentrations were measured six months after LV target (A) irradiation in PF and at different time points after LV target (B) and AVN target (C) irradiation in serum. Concentration of technical replicates, mean and SEM are shown. N.D. = not determined. * = p-value ≤ 0.05, ** = p-value ≤ 0.01, *** = p-value ≤ 0.001, **** = p-value ≤ 0.0001. Significance was tested with one-way Kruskal Wallis statistic and Dunn´s post hoc test.

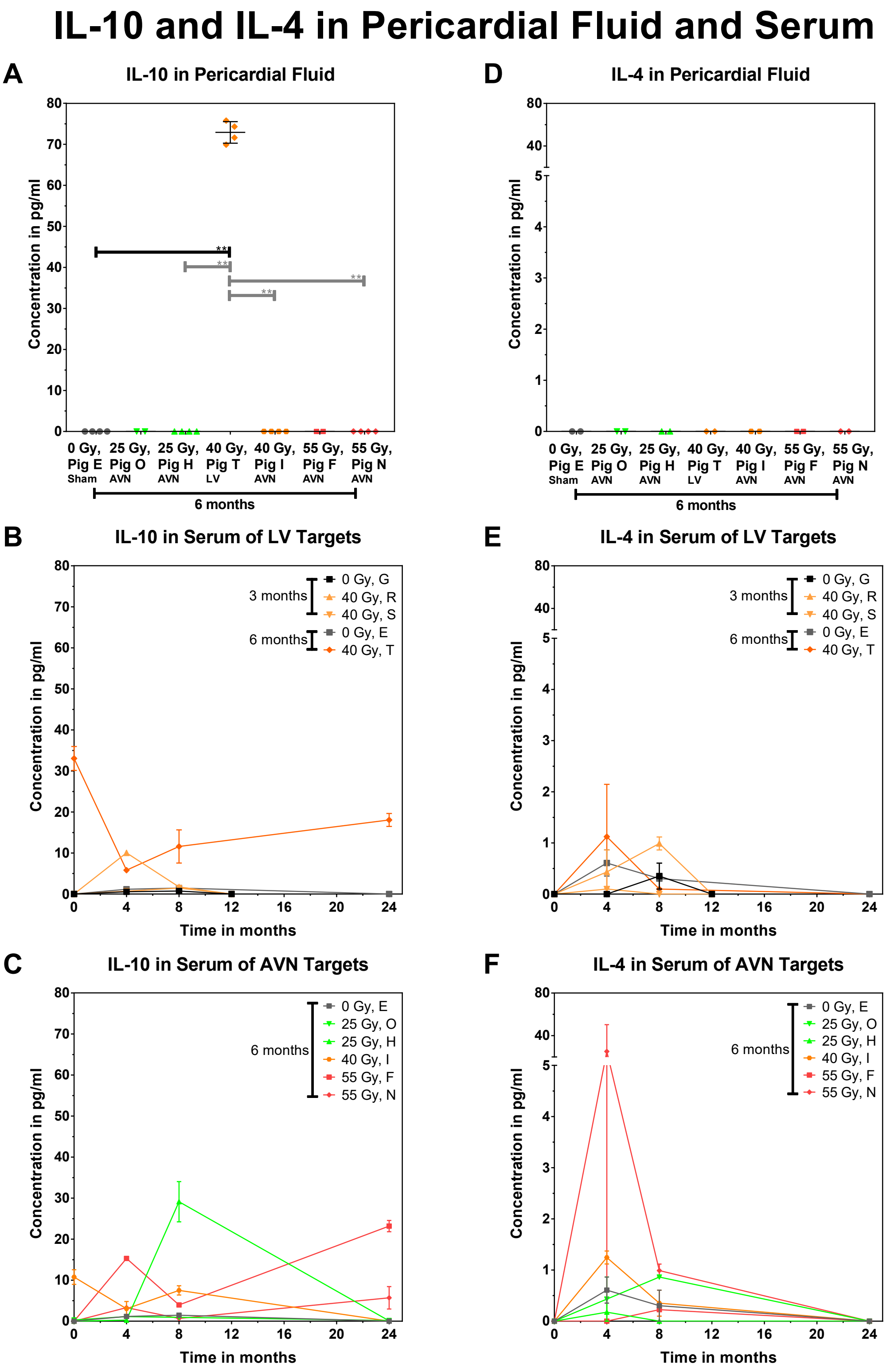

Figure 67: IL-10 release was only in PF elevated after LV irradiation. The release of IL-4 was not affected by irradiation. IL-10 and IL-4 concentrations were measured six months after LV target (A) and AVN target (D) irradiation in PF and at different time points after LV target (B and D) and AVN target (C and F) irradiation in serum. Concentration of technical replicates, mean and SEM are shown. The results for CRP release in PF are depicted again (Figure 43) to give a complete overview. N.D. = not determined. * = p-

value ≤ 0.05, ** = p-value ≤ 0.01, *** = p-value ≤ 0.001, **** = p-value ≤ 0.0001. Significance was tested with one-way Kruskal Wallis statistic and Dunn´s post hoc test.

Publications

Peer-Reviewed Articles

H.I. Lehmann, C. Graeff, P. Simoniello, A. Constantinescu, M. Takami, P. Lugenbiel, D. Richter, A. Eichhorn, M. Prall, R. Kaderka, F. Fiedler, S. Helmbrecht, C. Fournier, **N. Erbeldinger**, A.-K. Rahm, R. Rivinius, D. Thomas, H. Katus, S. Johnson, K. Parker, J. Debus, S. Asirvatham, C. Bert, M. Durante, D. Packer, “Feasibility Study on Cardiac Arrhythmia Ablation Using High-Energy Heavy Ion Beams”, Nature Scientific Reports, December 2016, doi: 10.1038/srep38895

N. Erbeldinger, F. Rapp, S. Ktitareva, A.-S. Bothe, T. Dettmering, M. Durante, T. Friedrich, B. Bertulat, S. Meyer, M. C. Cardoso, S. Hehlgans, F. Rödel, C. Fournier, “Measuring Leukocyte Adhesion to Endothelial Cells after Charged Particle Exposure with a dedicated Laminar Flow Chamber”, Frontiers in Immunology, June 2017, doi: 10.3389/fimmu.2017.00627

B. Baselet, O. Azimzadeh, **N. Erbeldinger**, M.V. Bakshi, T. Dettmering, A. Janssen, S. Ktitareva, D.J. Lowe, A. Michaux, R. Quintens, K. Raj, M. Durante, C. Fournier, M.A. Benotmane, S. Baatout, P. Sonveaux, S. Tapio, A. Aerts, “Differential Impact of Single-Dose Fe Ion and X-Ray Irradiation on Endothelial Cell Transcriptomic and Proteomic Responses”, Frontiers in Pharmacology, September 2017, doi: 10.3389/fphar.2017.00570.

J. Philipp, O. Azimzadeh, V. Subramanian, J. Merl-Pham, D. Lowe, D. Hladik, **N. Erbeldinger**, S. Ktitareva, C. Fournier, M. J. Atkinson, K. Raj, S. Tapio, “Radiation-Induced Endothelial Inflammation Is Transferred via the Secretome to Recipient Cells in a STAT-Mediated Process”, Journal of Proteome Research, October 2017, doi: 10.1021/acs.jproteome.7b00536

N. Erbeldinger, P. Simoniello, F. Rapp, H. I. Lehmann, P. Lugenbiel, A. Constantinescu, A. Eichhorn, M. Prall, R. Kaderka, D. Thomas, D. L. Packer, M. Durante, C. Graeff and C. Fournier, “Vascular and Fibrotic Changes as Underlying Mechanisms for Cardiac Ablation after High Dosed Carbon Ion Irradiation”, manuscript in preparation

N. Erbeldinger, F. Merz, T. Dettmering, A.-S. Bothe, J. Klinger, S. Ktitareva, M. Durante, C. Fournier, “Inflammation-related cell adhesion of lymphocytes to endothelial cells is inhibited under shear stress after irradiation”, manuscript in preparation

GSI Scientific Reports

N. Erbeldinger, P. Simoniello, F. Rapp, H. I. Lehmann, P. Lugenbiel, A. Eichhorn, D. Thomas, D. L. Packer, M. Durante, C. Graeff and C. Fournier, “Changes in Cellular Organisation Leading to the Interruption of Conductivity in a Porcine Model after the Exposure to High Doses of Carbon Ions”, GSI Scientific Report, 2016

N. Erbeldinger, F. Merz, P. Simoniello, H. I. Lehmann, P. Lugenbiel, A. Eichhorn, D. Thomas, D. L. Packer, M. Durante, C. Graeff and C. Fournier, “Vascular and Fibrotic Changes in Irradiated Myocard after Cardiac Ablation with Carbon Ions in a Pig Model”, GSI Scientific Report, 2015

N. Erbeldinger, M. Liebig, T. Dettmering, D. Lowe, Bjorn Baselet, R. Benotmane, S. Tapio4, K. Raj, M. Durante and C. Fournier, “Cytokine Release and Adhesion of Immune Cells to Cardiac Endothelial Cells”, GSI Scientific Report, 2014

C. Graeff, H. I. Lehmann, A. Constantinescu, P. Simoniello, P. Lugenbiel, M. Prall, D. Richter, M. Takami, A. Eichhorn, **N. Erbeldinger**, C. Fournier, R. Kaderka, S. Helmbrecht, F. Fiedler, J. Debus, D. Thomas, C. Bert, M. Durante and D. L. Packer, “Catheter-free Arrhythmia Ablation Using Scanned Carbon Ion Beams in a Porcine Model”, GSI Scientific Report, 2014

Conference Contributions

N. Erbeldinger, F. Merz, P. Simoniello, H. I. Lehmann, P. Lugenbiel, D. Packer, C. Graeff, M. Durante, C. Fournier, “Microvascular effects in a porcine model after carbon ion irradiation”, ERR 2016, Poster Presentation

N. Erbeldinger, P. Simoniello, H. I. Lehmann, P. Lugenbiel, M. Takami, A. Constantinescu, A. Eichhorn, D. Richter, M. Prall, D. Thomas, D. Packer, M. Durante, C. Graeff, C. Fournier, “Biological Effects of Cardiac Ablation with Carbon Ion Irradiation”, GBS 2015, Poster Presentation

N. Erbeldinger, P. Simoniello, H. I. Lehmann, P. Lugenbiel, M. Takami, D. Richter, A. Eichhorn, M. Prall, A. Constantinescu, A. Thomas, M. Durante, D. Packer, C. Graeff, C. Fournier, “Cardiac Ablation in a Pig Model with Carbon Ion Irradiation”, EACR 2015, Poster Presentation

N. Erbeldinger, M. Liebig, T. Dettmering, D. Lowe, K. Raj, M. Durante, C. Fournier, “Radiation induced adhesiveness of endothelial cells and related cytokine release investigated in human heart cells as markers of cardiovascular risk”, GBS 2014, Poster Presentation

Curriculum Vitae

Personal Data

Name:	Nadine Erbeldinger
Date of birth:	01.04.1989
Place of birth:	Lindenfels

Education and Work Experience

Since 04/2014	TU Darmstadt, GSI Helmholtz centre for heavy ion research Ph.D. candidate and scholar of the GrK 1657
01/2014 – 03/ 2014	GSI Helmholtz centre for heavy ion research Student Research Assistant
10/2011 – 04/ 2014	TU Darmstadt Master of Science in Technical Biology Titel of thesis: „Adhäsionsverhalten und Zytokinfreisetzung vaskulärer Zellen nach Einwirkung ionisierender Strahlung“
10/2008 – 10/ 2011	TU Darmstadt Bachelor of Science in Biology Titel of thesis: „ Untersuchungen zur Auswirkung ionisierender Strahlung auf die Struktur, das zelluläre Überleben und die Funktionalität von Retinaexplantaten des Huhns“
08/ 1999 – 07/2008	Liebfrauenschule Bensheim Abitur

Positions held

04/2014 – 03/ 2017	Student representative of the Graduate College 1657
07/2013 – 05/ 2015	Gender equality team at the Department of Biology, TU Darmstadt
10/2011 – 04/ 2014	Active member of the student body of Biology